A coupled left ventricle and systemic arteries model

by

Weiwei Chen

A thesis submitted to the

College of Science and Engineering

at the University of Glasgow

for the degree of

Doctor of Philosophy

September 2015

Abstract Mathematical modelling and computational simulation are effective tools in studying the function of the cardiovascular system and diagnosing the progress of diseases in this system, especially when clinical experiments or measurements are limited or not capable to proceed. A variety of models have been developed related to different segments in the cardiovascular system, such as the heart, the valves, the systemic arteries and the pulmonary arteries, etc. Among these studies, modelling the left ventricle (LV) and systemic arteries (SA) have drawn a great deal of attention in the last several decade due to the high pressure and high morbidity of the systemic circulation. The recent models range from lumped-parameter models, one-dimensional models to three-dimensional models,which expand our understanding of the function of the left ventricle and systemic arteries respectively, but few of them considered the interaction between two parts. Thus, the propose of this thesis is to develop a dynamic cardiac-vascular model to study the pressure and flow wave interactions in the systemic circulation.

Here we employs two advanced models, a three-dimensional finite-strain structure-based LV, and a one-dimensional dynamic physiologically-based model for the systemic arteries, to complete a coupled LV-SA model. The LV model is based on Gao et al. [35]'s work. In this model, the fluid-structure interaction (FSI) is described by an Immersed Boundary (IB) approach, in which an incompressible solid is immersed in a viscous incompressible fluid, and solved by a Lagrangian Finite Element (FE) method [40]. The systemic circulation model is employed from Olufsen et al. [90]'s work, which consists of two groups of arteries, the large arteries and the small arteries or vascular beds. The large-arteries model uses a LaxWendroff scheme to compute the cross-sectional area-averaged flow and pressure based on physiological parameters of the arterial tree. The vascular beds are modelled as asymmetric structured tree, to provide outflow boundary conditions at the end of each terminal vessel in the network of large arteries. The coupling is achieved by matching the pressure and flow rate at the aortic root, i.e. the circulation model feeds back the pressure as a boundary condition to the LV model, and the flow rate from the LV is used as the inflow for the circulation model. The function of the aortic valve (AV) is modelled as follows: the AV opens when the pressure in the LV just exceeds the pressure in the proximal aorta adjacent to the valve; the AV closes when the flow rate is negative (referring to backflow) at the boundary plane in the LV proximal to the AV. The governing equations of the system is solved by a combined immersed boundary finite element (IB/FE) method, and the LaxWendroff scheme of Olufsen et al. [90].

To investigate the cardio-vascular interactions under different conditions in the LV-SA system, this thesis first simulate a standard case defined by using parameters based on measurements of healthy

LV and healthy systemic arteries from two healthy subjects, and then simulating four diseased-related cases based on different pathological conditions in the LV-SA model, i.e. stiffening of the large arteries, functional rarefaction, increasing heart beat rate (by shortening the systemic diastolic phase) and varied end-of-diastolic pressure. The results of pathological cases are compared with the standard case to provide a more insightful change of the pressure/flow interaction, and the change of LV contractility.

To better understand the cardiac-valvular-vascular interactions, a lumped-parameter AV model is coupled in the LV-SA model to further develop it into a more detailed LV-AV-SA model. Compared to the LV-SA model (no AV), when a normal AV condition is used in the coupled LV-AV-SA model, the active tension of the LV and the peak LV pressure at early systole slightly increases, but the peak flow rate and the cardiac output barely changed. While, when a mild stenosis AV condition is applied in the LV-AV-SA model, the LV function changes dramatically, especially a dramatically increase of the peak LV pressure and the peak active tension of the LV. This indicates that the valve condition is also important in studying cardiac-vascular interactions, especially for diseased valve conditions that the effects are huge and cannot be ignored.

In order to study how the valvular region affects the cross-valve pressure difference, we reconstruct the valvular region in the LV based on the mid-systolic CMR images, which shows a 93% increase of the cross-sectional area in the valvular region than early systole. The cross-valve pressure drop decreases dramatically with a expanded valvular region compared with the narrower valvular region in previous LV-SA model. This indicates that the a local stenosis in the valvular region may have significant effects on the heart function, and a better description of modelling the expanding procedure of the valvular region is needed to predict more physiological results.

This thesis is a step forward for studying the cardiac-valvular-vascular interactions in the systemic circulation, and can provide dynamic pressure and flow waveforms in the LV and long the systemic arteries. Moreover, this model not only verifies the effects of pethological conditions but also quantifies change of pressure, flow rate and ventricular inotropy in the LV-SA system, which is important progress and has barely been studied before. Further approach of this work is to develop a patient-specific model in the future to diagnose the progress of disease, as well as providing practical treatment strategy.

Acknowledgments Foremost, I would like to express my special appreciation and thanks to my supervisor Prof. Nicholas Hill for his guidance and encouragement during my four years' study in University of Glasgow. Since English is not my first language, at the beginning of my study he helped me a lot with improving my speaking and writing skills, and I am very grateful for his kindness and patient all the time. I am also sincerely grateful to my second supervisor Prof. Xiaoyu Luo for her thoughtful care of not only my research, but also my living in Glasgow. I am very enjoying the group meetings hold by them every week, in which people could share ideas, discuss problem, and gain useful suggestions from other people. The group meeting makes me feel more like we are a big family and it gives me a lot of comfort when I am missing home. Four years time gives me an inner view of the advanced British researchers' spirit, especially from my supervisors. Their hardworking, conscientiousness, especially the love for their works impress me and encourage me all the time. I am appreciate for the many fruitful conversations, the conferences they support me to attend, and the time they have devoted to reviewing my thesis. It is my great honor to be one of their postgraduate students. Thanks to Prof. Yufeng Nie for his guidance during university, and thanks to my teachers, Xiaoli Zhao, and Decang Guo in high school. I also want to give a special thanks to Janette Mcquade for her tutoring in English Cafe in the last two years, which helps me a lot with my spoken English and gives me a deeper and wider view of Scotland.

Thanks to all the colleagues and friends for their company during the last four years. A special thanks to Dr. Beibei Li for helping me settle down when I first arrived in Glasgow. Thanks for one of my best office friends Nan Qi for her wonderful company, especially those get-together parties during the Chinese traditional festivals. Thanks also to Dr. Hao Gao for his patient answering my questions of C++ and VISIT. Thanks to my office friend Lei Wang for helping me solve Euclid problems. During the last year, thanks for the many wonderful conversations with Xin Zhuan, I have learnt a lot from his creative thoughts and enterprising mind, which makes me think more of continues self-improving in the future. I am also very grateful to Yuji Chen for taking me to experience the beauty of Scotland, especially those mountain walkings in winter, giving me a stronger mind to face and conquer difficulties in life.

I am also grateful to the Chinese Scholarship Council for the four years funding for living, and thanks for the tuition fee waiver from University of Glasgow. I also acknowledge the excellent research atmosphere and advanced facilities provided by the University of Glasgow during the last four years. Thanks also to the people I know or not know in Glasgow, their kindness and their love for Glasgow makes me love more of this city day by day.

Last but not the least, thanks to my dearest mother Yuyun Zhu for her encouragement and strong supports for my study, and the thoughtful care trough the hundreds of phone calls during the last four years. Thanks also to my father Weiliang Chen for making me independent and being strong.

List of Figures

List of Tables

Contents

Chapter 1

Introduction

1.1 Background

1.1.1 The cardiovascular system

The cardiovascular system is composed of the heart and blood vessels, including arteries, veins and capillaries, and they consist of the two circulatory systems, i.e. the pulmonary circulation and the systemic circulation. With each heartbeat, blood carries all of the oxygen, nutrients, hormones, etc throughout the body and takes the toxins and carbon dioxide away from the cells [15, 108]. Every day, approximately 10 pints (5 litres) of blood travels about 60,000 miles (96,560 kilometers) through the blood vessels, linking the cells of our organs and body parts [15], starting from before birth and lasting for a lifetime without break. Since the cardiovascular system is so important in maintaining human life, it is worthwhile to get a better understanding of it and the interactions between each component in the system.

The heart

The heart is the key organ in the cardiovascular system. It works as a hollow, muscular pump, propelling blood throughout the whole body constantly without ever pausing to rest. It has four hollow chambers enclosed by cardiac muscles.

The upper two chambers are the atria, receiving the blood entering the heart, and are separated by a common wall, the inter-atrial septum. The bottom two chambers are ventricles, pumping blood out of the heart, and separated by the interventricular septum wall (Fig. 1.1). The atrial muscles are thin and develop only relatively low pressures when the atria contract. The right atrial wall

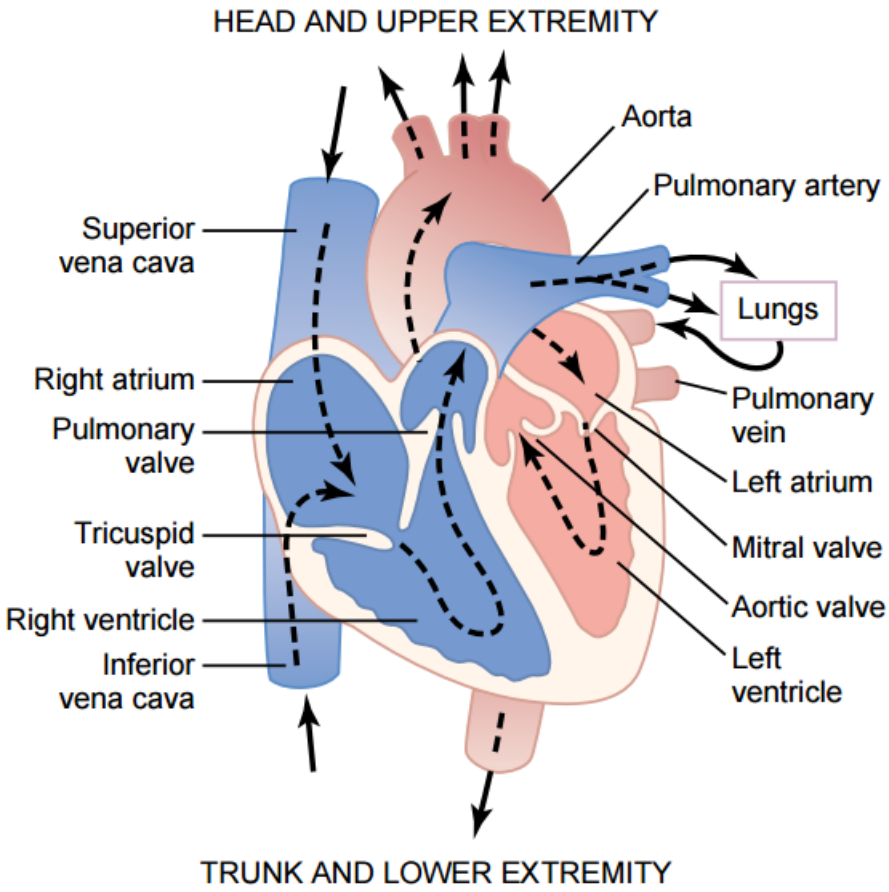

Figure 1.1: A sketch of the human heart. From [45].

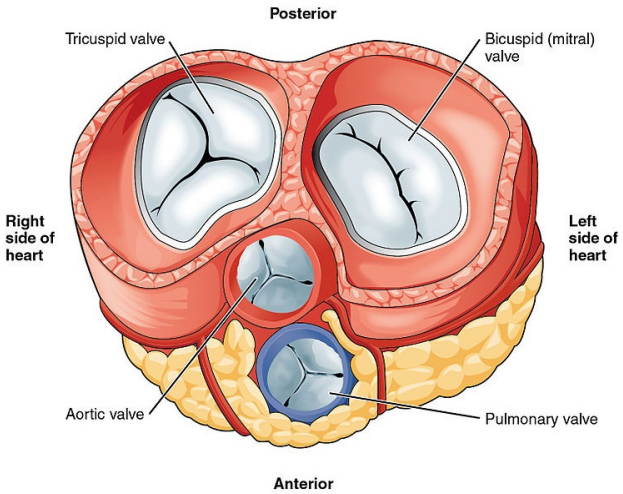

Figure 1.2: A transverse section through the heart illustrates the four heart valves. From [10].

is thinner than the left, and the right atrial pressure is consequently lower than the left [68]. The atrial chambers do not contribute much to the resting cardiac function, since the atrial filling is

generally considered as a passive process. The ventricular wall is thicker than the atrial walls. Moreover, the wall thickness of the left ventricular is around two times larger than the thickness of the right ventricle in order to develop a much higher pressure [68]. The thick interventricular septum wall laying between the right and left chambers is associated with the pumping action of the left ventricle.

The ventricle and atria are separated by atrioventricular valves. The tricuspid valve separates the right atrium from the right ventricle, and the mitral valve separates the left atrium and the left ventricle. Two other heart valves lie between the ventricles and the large arteries, which carry blood leaving the heart. These valves are the pulmonary valve, which separates the right ventricle from the pulmonary artery, and the aortic valve, which separates the left ventricle from the aorta. These four valves are aligned approximately in the same plane (Fig. 1.2).

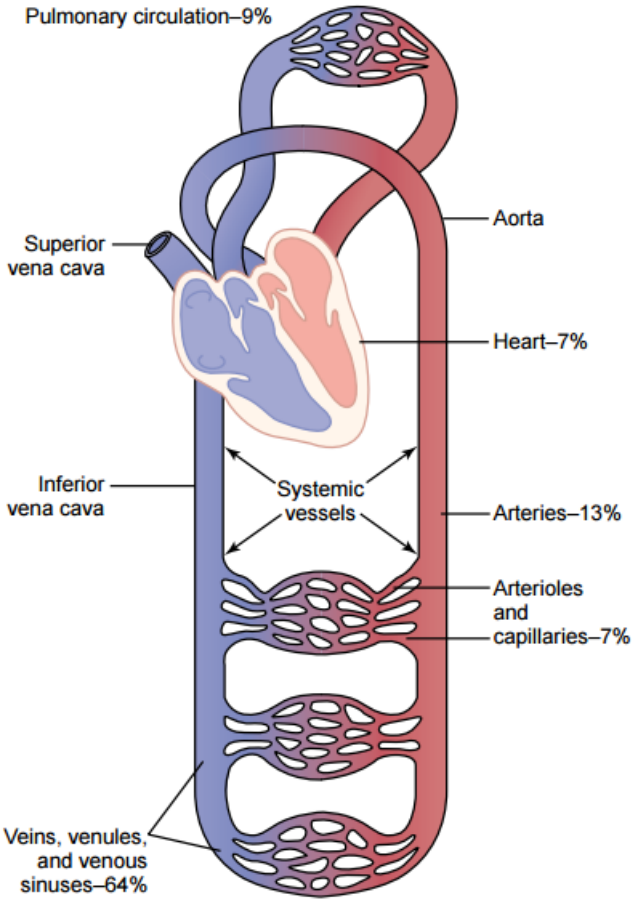

Figure 1.3: Distribution of circulation of blood in the arterial system with percentage of total blood in different parts of the circulation system. From [45].

During each heartbeat, the left atrium gathers oxygenated blood from the lungs to the left ventricle,

which pumps it throughout the body, while the right atrium receives deoxygenated blood from the body and delivers to the right ventricle to pump it through the lungs (Fig. 1.3). These double pumps repeat during each heart beat at the beginning of the systemic and pulmonary circulations.

The blood vessels

There are three types of blood vessels, i.e. arteries, veins and capillaries (Fig. 1.4). The arteries carry highly oxygenated blood away from the heart, while veins bring deoxygenated blood back to the heart [7, 94]. The capillaries connect the arterioles at one end and venules at the other, carrying blood very close to the cells of the tissues of the body in order to exchange gases, nutrients, and waste products. The wall of an artery consists of three layers (Fig. 1.4), i.e. the innermost layer (the tunica intima or tunica interna), the middle layer (the tunica media) and the outermost layer (the tunica adventitia). The middle layer is primarily smooth muscle and is usually the thickest layer. Since the arteries have a higher blood pressure than other parts of the circulatory system (Fig. 1.5), the arterial wall is thicker than the other vessels (Fig. 1.4) [7]. The blood pressure in veins are much lower than arteries with lower flow rate (Fig. 1.5), so there are valves on the inner layer to prevent reversed flow [94]. The capillaries have the thinest wall among three types of vessels being only one cell layer thick (measuring around 5 to 10 μm), in order to allow the exchange of water, oxygen, carbon dioxide, and many other nutrients and waste substance between the blood and the tissues surrounding them [62]. Remarkably, residual stress and pre-stretch in the arteries ensures no change in length as the pressure pulse passes through [48].

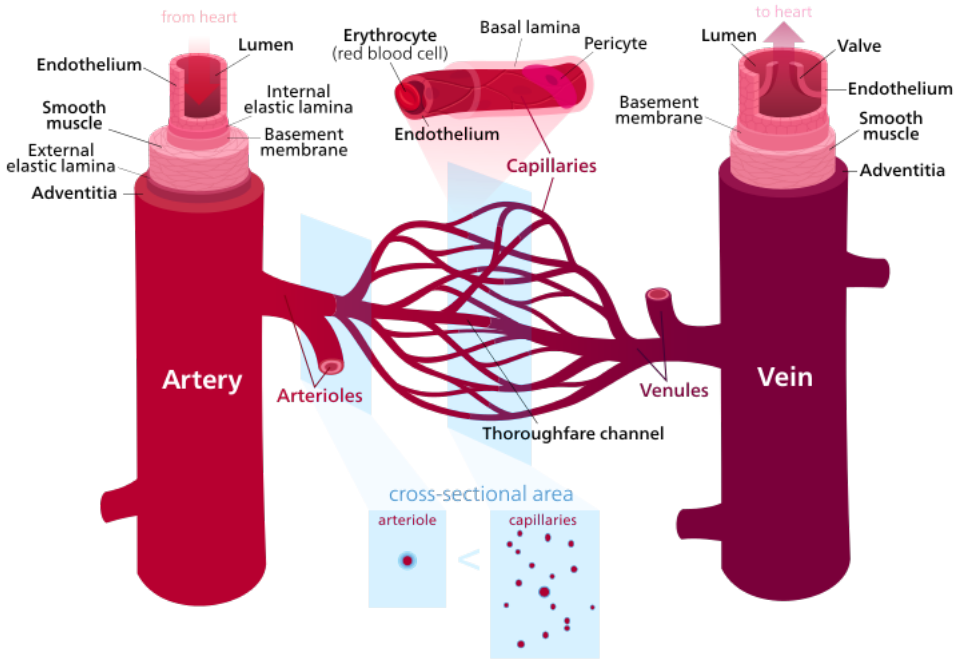

Figure 1.4: Diagram of arteries, veins, and capillaries, from *https://en.wikipedia.org/wiki/File:Blood_vessels_-_en.svg* by Kelvinsong (2013).

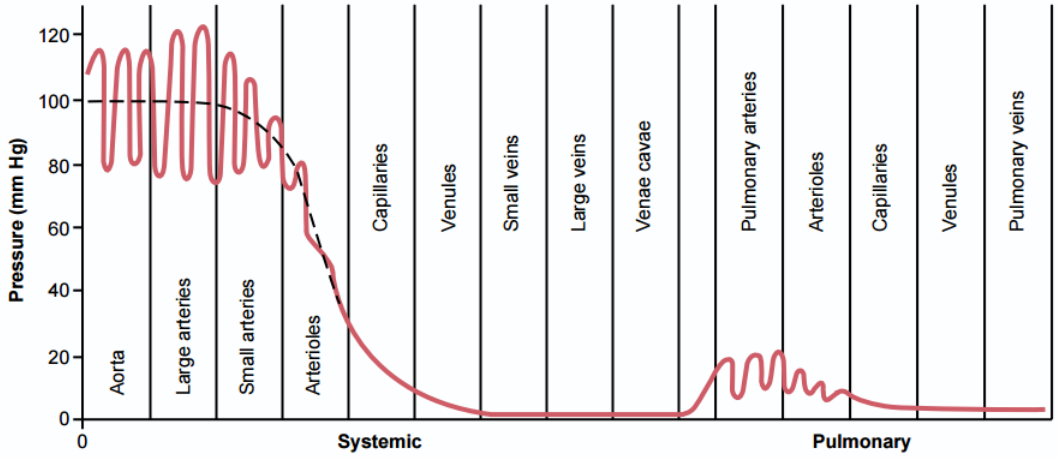

Figure 1.5: Mean pressure drop across different levels of circulatory arterial system [45].

1.2 Mathematical modelling of the cardiovascular system

Mathematical modelling and computational simulation are useful in studying the cardiovascular system and diagnosing the progress of diseases in order to give suitable treatment strategy. A number of in vivo, in vitro experiments, and advanced imaging technologies, such as magnetic resonance imaging (MRI) and computed tomography (CT) scan, provide high fidelity haemody-

namic information for mathematical modelling [11]. There are a variety of models ranging from lumped parameter (or zero-dimensional, 0D) models [1, 4, 12, 14, 75, 87, 104, 113, 116, 129], one-dimensional (1D) models [9, 50, 74, 79, 90, 102, 103, 111, 113] to three-dimensional (3D) models [17, 20, 26, 29, 35, 37, 41, 56, 58, 77, 81, 96, 100, 112, 117, 118, 124, 131] used for simulating the fluid mechanics in different segments of the cardiovascular system. Such studies expand our understanding of the function of the heart and other segments in the cardiovascular system. Here, we have a brief review of three important components of the systemic circulation: the left ventricle, the aortic valve, and the systemic arteries, so that we can have a better understanding of current work and to develop a more detailed cardiac-valvular-arterial model to study the interactions between each component.

1.2.1 Modelling of the left ventricle

The lumped parameter (0D) models related to the LV characterize basic relationships between the circulatory variables and heart properties [4, 12, 75, 104, 116]. Among these, the early models developed by Maughan et al. [75],Beyar et al. [12] and Santamore and Burkhoff [104] are constructed with time variable removed, then based on these studies Sun et al. [116] and Arts et al. [4] further developed four-chamber heart interaction models enable to simulate the cardiac haemodynamics of the heart with normal and diseased conditions. These lumped-parameter models are efficient in computational simulation, but they do not account for many ventricular properties and can not provide the propagation of the pressure or flow waves inside the left ventricle.

In order to study the fluid dynamics of the left ventricle, a number of high dimensional computational models of the left ventricle have been developed [20, 35, 41, 58, 77, 81, 100, 124, 131]. The basic approach in these models is to construct the three-dimensional geometry and the passive and active elastic response of the ventricular myocardium. The detailed three-dimensional fiber orientations and sheet structure of the ventricular wall are constructed in Bovendeerd et al. [13], Costa et al. [20], Nash and Hunter [81], Wang et al. [123]. The elasticity with constitutive modelling of the myocardium differs in different studies. Early studies are based on isotropic elasticity [23], which only include the isotropic exponential form in the strain-energy function. Further studies are based on transversely isotropic elasticity, among these, Humphrey and Yin [51] accounts for the fibre structure,Humphrey et al. [52] characterize the passive viscoelastic response of the myocardium, and some other models are based on the components of the Green–Lagrange strain tensor [13, 19, 43], but a subsequent study shows that the myocardium is not a uniformly branching

continuum but a laminar hierarchy [65]. More recently, orthotropic constitutive models are developed to describe the laminar characteristic of the ventricular myocardium [20, 47, 53, 105]. The active tension generation of the myocardium is modelled by various groups [13, 44, 81, 84, 120]. These active models relate the transmural variations of fibre orientation and the passive response in the left ventricle.

In order to study the intracardiac fluid dynamics of the left ventricle, detailed fluid-structure interaction (FSI) models are developed by several groups [35, 41, 76, 77, 86, 100, 124, 125]. Some groups use the arbitrary Lagrangian–Eulerian (ALE) method [76, 86, 124, 125], of which Watanabe et al. [124] model the propagation of excitation and contraction mechanics of the cardiac muscles; Nordsletten et al. [86] use a nonconforming ALE framework for modelling the passive diastolic and active systolic phases of the heart; McCormick et al. [76] use the fictitious domain (FD) method to investigating the full range of cardiac motion under LVAD support. These ALE models can provide detailed fluid dynamics and fluid-solid interactions in the LV, but the dynamic mesh generation caused by large structural deformations yield significant computational difficulties. An alternative approach to FSI models is based on the immersed boundary (IB) method, first introduced by Peskin [99]. In the IB approach, the solid structure is immersed in a fluid region, and the deformation and stress of the solid structure is described in Lagrangian coordinates, while the momentum of the fluid is described in the Eulerian form, using the Dirac delta function to mediate the integral transform. The main feature of IB method is that the Lagrangian grid overlays the Eulerian mesh, thus it does not require a dynamic generated discretization of the solid and fluid. Thereby, it is more efficient than ALE methods for modelling large structural deformation systems. The IB method has been applied in modelling the fluid dynamics of the LV [35, 77, 97], the aortic valve [42], and the mitral valve [33, 36, 71]. Although all these three-dimensional models have achieved various degrees of success, most applying fixed boundary conditions, and with the absence of detailed downstream models, cannot provide a more realistic cardiac-arterial interactions in the whole circulation.

1.2.2 Modelling the aortic valve

To study the complexity of the valve motion dynamics, a number of numerical studies have been carried out. The lumped-parameter models of the aortic valve are usually based on two altemative assumptions. One group of models treats the vortex in the sinus as the driving force for valve motion [8, 30], the other group takes the pressure difference across the valve as the main driver

for the valve motion [67, 80, 98]. Among them, early studies [25, 46, 95, 122] models the heart valves as a diode with a resistance. Werner et al. [128] considered the volume of reversed flow in the valve during closure related with the leaflet opening angle. Korakianitis and Shi [59], Shi et al. [109] and Mynard et al. [80] considered the local flow resistance and the blood inertial effect of the valve dynamics. Furthermore, Mynard et al. [80] related the resistance and the inertial terms with the valve state, which can provide more realistic pressure difference and can be used to study normal or pathological valve conditions. These lumped-parameter models provide the basic opening and closing motions of the valve and are easy to be used as part of the global mechanics of the cardiovascular system. However, these models cannot provide detailed fluid field in the valve region.

To predict more detailed fluid dynamics in the valve, three-dimensional models have been developed with the benefits from advanced imaging technology [16, 21, 22, 39, 73, 98]. These models provide detailed three-dimensional fluid dynamics across the valve, and account for complex flow patterns and realistic valve sinus.

1.2.3 Modelling the arterial system

Another important part of the cardiovascular system is the systemic arteries. Simple lumped-parameter models has been developed to describe the heamodynamics of the arterial system [1, 4, 14, 87, 113, 129]. Among these models, the most widely used models are windkessel models, including two-element (or RC) windkessel models [70], three-element (or RCR) windkessel models [14, 113, 129], and four-element windkessel models[27, 114]. The key idea of windkessel model is treating the blood pressure similar to voltage and blood flow similar to current as in an electric circuit, and using resistance (R) and compliance (C) to adjust the pressure and flow relations [129]. The RC model taking account of the total compliance (C_T) and the peripheral resistance (R_p) is shown in Fig. 1.6 (a). The governing equation for the RC model is

$$q(t) = \frac{p(t) - P^{\infty}}{R_p} + C_T \frac{dp(t)}{dt}. \tag{1.1}$$

The RCR model is the most commonly used windkessel model. It incudes an additional resistance connecting in series with the RC model (Fig. 1.6 (b)), making the RCR model taking account both resistive and compliant effects of the proximal vessels, and this resistance is a frequency-dependent impedance (R_c) [114]

$$R_c(\omega) = \frac{p(\omega)}{q(\omega)}. \tag{1.2}$$

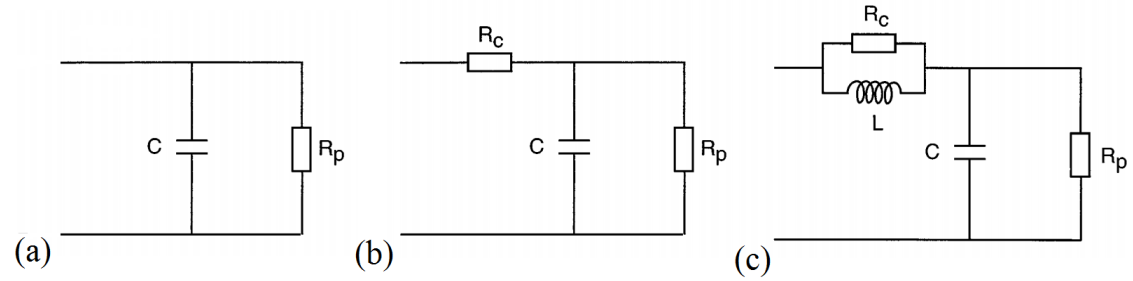

Figure 1.6: Schematics of 2-element (a), 3-element (b) and 4-element (c) windkessel models presented in electrical form. R_c and R_p are the characteristic and peripheral resistance, respectively; C is the total arterial compliance; L is the inertance.

The governing equation for the RCR model is

$$p(t) - P^{\infty} + R_p C_T \frac{dp}{dt} = (R_p + R_c)q + R_c R_p C_T \frac{dq}{dt}. \tag{1.3}$$

In the four-element windkessel model, the total arterial inertance L is included in parallel with the characteristic impedance in the system (Fig. 1.6 (c)) to provide more accurate total arterial compliance [114]. The inertance is defined as

$$L = \frac{\rho l}{A_0}, \tag{1.4}$$

where ρ is the blood density, l is the length of the vessel segment, and A_0 is the reference cross-sectional area. These windkessel models can provide basic blood pressure/flow interactions and basic heart and vascular properties, but with only a small number of parameters, it can not provide the effects of wave propagation in the arterial system. The point is that the parameters are ”tuned” to obtain a ”realistic” pressure and flow. They do not all represent physiologically measurable parameters, and cannot represent diseased vessels.

To investigate the wave propagation in the arterial system, a series of one-dimensional (1D) models are developed [9, 50, 74, 79, 90, 102, 103, 111, 113]. Basically, these are cross-sectional-area-averaged arterial models, in which some basic parameters, such as the length, radius, etc., are generated from clinical measurements. These models are based on one-dimensional flow equations and the large arteries are modelled as a binary tree, with lumped vascular models or structured-tree models to provide the outflow boundary condition of the large arteries. Since 1D models are efficient in computational simulation, it is possible to take in account of as many as arteries to do simulations. Currently, 1D models can include as many as 259 arteries in the cardiovascular system [79], and this also depends on the ability of measurements from clinical techniques. These

models provide detailed information of volumetric flux (flow) and pressure along the arterial system, and they can be used to study pathological conditions by changing the local parameter values. However, these models do not include detailed local flow information, such as the velocity profile on the cross-sectional area.

More detailed three-dimensional (3D) models have been developed to study the local fluid dynamics of certain segments of the large arteries [37, 96, 112]. These 3D models can provide values of localized haemodynamic quantities, such as wall shear stress, and particle residence time, but these models are limited to small segments of the arterial system due to the high computational cost and the limitation of measurements [26, 118].

Some multiscale approaches coupling 3D and 1D arterial models have also been developed [28, 69, 119], what can provide more insights into both local and global characteristics of blood flow, pressure profiles and arterial wall biomechanics. However, a detailed 3D heart is not usually included, instead volumetric flow rates are prescribed at the inlet [26, 90, 119], or simplified lumped heart models are used [4, 56]. Consequently, the cardio-vascular interaction is not fully explored.

1.3 Motivation and objectives of this thesis

Since cardiovascular disease (CVD) is the leading global cause of death, accounting for nearly half of the 36 million deaths due to noncommunicable diseases [63], understanding how the disease develops and the relationships between each part of the cardiovascular system are very important for reducing mortality and morbidity, which is the basic motivation behind this work. Computational simulation is effective in studying the cardiovascular system, since current clinical technology cannot provide measurements of all physiological segments simultaneously in the cardiovascular system in order to study the interactions.

Current mathematical models ranging from lumped-parameter models to three-dimensional dynamic models have improved our understanding of different segments of the cardiovascular system, such as the heart, heart valves, systemic arteries, pulmonary arteries, etc. However, due to the complexity of the cardiovascular system, very little work has been devoted to study the circulatory interactions between segments in the cardiovascular system. Thus, our goal in this thesis is to develop a complete systemic circulation model including a dynamic left ventricle and a large brunches of systemic arteries in order to make progress of current works to study the interactions.

First, we start our work by taking account of relevant models to build up a dynamic LV-arterial model by adapting two advanced models of the LV and systemic arteries. In this work, we choose the model described in Gao et al. [32, 35], since this is a full fluid-structure interaction (FSI) model and includes both passive and active contraction, which is important when making comparisons with physiological properties. For the systemic arterial circulation, we use the 1-D structured tree model introduced by [89], since it considers both large arteries and vascular beds, and is based on physiologically measurable parameters. The 1-D models using cross-sectionally averaged flow are based on parameters of the arterial tree, such as length, radius, compliance, which could be measured and then varied to simulate disease. Olufsen et al. [91] also showed how to calculate pressure drop and flow in the small arteries to the vascular beds. Recently, Qureshi and Hill [102] have extended the structured tree model of Olufsen et al. [90] to analyse pressure and flow in the pulmonary arterial and venous circulation, which would be a good support for developing a right ventricle and pulmonary circulation model in order to study the interactions in the cardiovascular system which includes the whole heart, the systemic and the pulmonary circulations in the future study.

After this proof-of-concept study, we improve the coupled LV-arterial model by adding a lumped parameter AV model [80] to get a new LV-AV-arterial model, which can provide more realistic results of the pressure drop across the AV plane and can be used to study aortic valve stenosis problem, which makes the ventricular-arterial model more complete for studying the fluid interactions in this system. The work detailed in this thesis represents a necessary step towards our goal.

1.4 Thesis layout

This chapter (Chapter 1) includes basic physiological description of the human cardiovascular system, along with a brief review of mathematical modelling of the left ventricle, the systemic circulation and aortic valve.

Chapter 2 includes a more detailed description of the mathematical methods for developing the left ventricle, systemic arteries and the aortic valve models we are using in this work.

Chapter 3 describes the procedure of coupling the three-dimensional left ventricle and the one-dimensional systemic arterial model.

Chapter 4 studies the results of the coupled LV-arterial model and comparisons with measured data.

Chapter 5 gives applications of disease conditions and shows results of four disease-related cases.

Chapter 6 describes the methodology of adding a lumped parameter AV model into the previous coupled model to get a new LV-AV-arterial model.

Chapter 7 studies the results from the coupled LV-AV-arterial model and shows comparisons and improvements with previous LV-arterial model.

Chapter 8 summaries the achievements of this thesis and shows the limitations of this work by giving suggestions for future study.

Chapter 2

Mathematical modelling

In this chapter, the mathematical methods for the description of the left ventricle (LV), and systemic arteries (SA) models are formulated. First, the basic theory employed in the three-dimensional (3D) dynamic left ventricle model is discussed, along with a general description of the immersed-boundary (IB) method used in this model. Second, the mathematical methods for the one-dimensional (1D) systemic arteries model are described, including modelling of the large arteries and vascular beds, which are modelled as structured-trees. Thirdly, the boundary conditions and the numerical methods for solving both fluid-structure interaction systems are briefly described in this chapter. The boundary conditions for the coupled domains between the two models, i.e. the inlet boundary condition in the arterial system and the outlet boundary condition in the LV model when the two models are coupled, are described in detail in the following chapter.

2.1 The 3D left ventricle model

The three-dimensional LV model is an imaging-derived model using a hybrid finite difference/finite element version of the immersed-boundary method [40] to simulate the dynamics of the LV.

2.1.1 The Immersed-boundary finite-element method

The immersed boundary (IB) method is intended to solve fluid-structure interaction (FSI) problems, in which an incompressible solid is immersed in a viscous incompressible fluid [99]. In the IB approach, the elasticity of the immersed elastic structure is described by a Lagrangian formula-

tion, and the viscous incompressible fluid is described by Eulerian incompressible Navier-Stokes equations. The IB equations are based on a fixed Cartesian mesh for the Eulerian variables, and a moving curvilinear mesh for the Lagrangian variables. These two types of variables are linked by the interaction equations of the Dirac delta function. The key idea is to make the equations of the elastic structure as much as possible like the equations of the fluid dynamics, so that the fluid-structure interaction can be dealt with easy.

The equations of motion

The equations of motion in the IB form is given below, and the more detailed derivation can be found in Peskin [99].

Let $\Omega \subset \mathbb{R}^3$ denote the physical domain occupied by the fluid-structure system, in which $\mathbf{x} = (x_1, x_2, x_3) \in \Omega$ are fixed Eulerian coordinates. Let $U \subset \mathbb{R}^3$ denote the reference configuration of the immersed solid, in which $\mathbf{X} = (X_1, X_2, X_3) \in U$ are fixed Lagrangian coordinates. If $\chi(\mathbf{X}, t)$ describes the physical position of material point $\mathbf{X}$ at time t, then the physical region occupied by the immersed solid at time t is $\chi(U, t) = \Omega(t) \in \Omega_s$, and the region occupied by the fluid at time t is $\Omega_f(t) = \Omega \setminus \Omega_s$. The IB/FE formulation of the equations is [39]

$$\rho \left(\frac{\partial \mathbf{u}}{\partial t}(\mathbf{x}, t) + \mathbf{u}(\mathbf{x}, t) \cdot \nabla \mathbf{u}(\mathbf{x}, t) \right) = \nabla \cdot \sigma(\mathbf{x}, t) = -\nabla p(\mathbf{x}, t) + \mu \nabla^2 \mathbf{u}(\mathbf{x}, t) + \mathbf{f}^s(\mathbf{x}, t), \tag{2.1}$$

$$\nabla \cdot \mathbf{u}(\mathbf{x}, t) = 0, \tag{2.2}$$

$$\mathbf{f}^s(\mathbf{x}, t) = \int_U \nabla_{\mathbf{X}} \cdot \mathbb{P}^s(\mathbf{X}, t)\, \delta(\mathbf{x} - \chi(\mathbf{X}, t))\, d\mathbf{X} - \int_{\partial U} \mathbb{P}^s(\mathbf{X}, t)\, \mathbf{N}(\mathbf{X})\, \delta(\mathbf{x} - \chi(\mathbf{X}, t))\, dA, \tag{2.3}$$

$$\frac{\partial \chi}{\partial t}(\mathbf{X}, t) = \int_\Omega \mathbf{u}(\mathbf{x}, t)\, \delta(\mathbf{x} - \chi(\mathbf{X}, t))\, d\mathbf{x}, \tag{2.4}$$

where ρ is the fluid density, μ is the viscosity, $\mathbf{u}(\mathbf{x}, t)$ is the fluid velocity, $p(\mathbf{x}, t)$ is the pressure, $\mathbf{f}^s(\mathbf{x}, t)$ is the Eulerian force density derived from the first Piola–Kirchhoff stress $\mathbb{P}^s(\mathbf{X}, t)$ as in (2.3), which is determined from the passive hyperelastic properties of the myocardium and the active tension generated by the myocytes in systole. $\mathbf{N}(\mathbf{X})$ is the exterior unit normal to U, and $\delta(\mathbf{x}) = \delta(x_1)\delta(x_2)\delta(x_3)$ is the three-dimensional Dirac

delta function in the following form:

$$\int_V \delta(\mathbf{x}-\mathbf{X})\,d\mathbf{x} = \begin{cases} 1, & \text{if} \quad \mathbf{X} \in V, \\ 0, & \text{otherwise}, \end{cases} \tag{2.5}$$

where $V \subset U$ is an arbitrary region of physical space.

The first two equations, (2.1) and (2.2), are the Navier–Stokes equations of a viscous incompressible fluid written in the Eulerian form. Equations (2.3) and (2.4) denote the interaction between the Eulerian and Lagrangian variables. In (2.3), the Eulerian elastic force density $\mathbf{f}^{\mathrm{s}}(\mathbf{x},t) = \nabla \cdot \sigma(\mathbf{x},t)$ is determined by two integral transforms with delta functions, which are $\nabla_{\mathbf{X}} \cdot \mathbb{P}^s$, the Lagrangian internal force density, and $-\mathbb{P}^{\mathrm{s}}\mathbf{N}$, the Lagrangian transmission force density. In the IB method, the Cauchy stress is separated into two parts: one is naturally written in Eulerian framework, and the other is easily described in Lagrangian form. The Cauchy stress tensor in the coupled fluid-structure system is

$$\sigma(\mathbf{x},t) = \begin{cases} \sigma^{\mathrm{f}}(\mathbf{x},t) + \sigma^{\mathrm{s}}(\mathbf{x},t) & \text{for} \quad \mathbf{x} \in \chi(U,t), \\ \sigma^{\mathrm{f}}(\mathbf{x},t) & \text{otherwise}, \end{cases}$$

where $\sigma^{\mathrm{f}}(\mathbf{x},t)$ is the Cauchy stress of a viscous incompressible fluid, and $\sigma^{\mathrm{s}}(\mathbf{x},t)$ is the Cauchy stress that describes the elasticity of the immersed structure.

The fluid mechanics of Newtonian blood fluid

Let $\Omega_f(t) = \Omega \setminus \Omega_s$ denote the fluid domain in the current configuration, in which $\mathbf{x} = (x_1, x_2, x_3) \subset \Omega_f$ are the fluid nodes in the Eulerian coordinates. Then, the velocity of fluid $\mathbf{u}$ is defined as

$$\mathbf{u} = \frac{\partial \mathbf{x}}{\partial t}. \tag{2.6}$$

The fluid stress from the general Navier–Stokes equation is

$$\boldsymbol{\sigma}^{\mathrm{f}} = -p\mathbb{I} + \tau \tag{2.7}$$

where $p = p(\mathbf{x},t)$ is the pressure in current configuration, $\mathbb{I}$ is the second-order unit tensor, and τ is the shear stress.

For the Newtonian laminar flow, the shear stress is calculated from

$$\tau = \mu(\nabla\mathbf{u} + (\nabla\mathbf{u})^T) \tag{2.8}$$

where μ is the fluid viscosity, $\nabla\mathbf{u}$ is the velocity gradient.

Solid mechanics of the LV wall

In the LV model, the passive and the active stresses contribute to the total stress for the myocardium,

$$\sigma^{\mathrm{s}} = \sigma^{\mathrm{p}} + \sigma^{\mathrm{a}} \tag{2.9}$$

where σ^{p} is the passive elastic response and σ^{a} is the active stress.

Description of deformation

Let $\mathbb{F} = \partial\chi/\partial\mathbf{X}$ be the deformation gradient associated with the structural deformation, and $J = \det\mathbb{F}$ is the local volume ratio. Then, the right Cauchy-Green deformation is defined as

$$\mathbb{C} = \mathbb{F}^T\mathbb{F}. \tag{2.10}$$

The passive hyperelastic stress response

If the existence of free-energy function $W(\mathbf{C})$ are postulated here, the first Piola-Kirchhoff stress $\mathbb{P}(\mathbf{X})$ is obtained for the incompressible LV wall as

$$\mathbb{P}(\mathbf{X}) = -p\mathbb{F}^{-1} + \frac{\partial W(\mathbb{C})}{\partial\mathbb{C}}, \tag{2.11}$$

where p is the hydrostatic pressure.

If the resultant Cauchy stress on the solid infinitesimal in the current configuration is $\boldsymbol{\sigma}^{\mathrm{p}}(\mathbf{x})$, the relation between Cauchy and the first Piola-Kirchhoff stresses is written as

$$\int_{\partial V} \mathbb{P}^{\mathrm{p}}(\mathbf{X},t)\mathbf{N}\,dA = \int_{\partial\chi(V,t)} \sigma^{\mathrm{p}}(\mathbf{x},t)\mathbf{n}\,da, \tag{2.12}$$

for any smooth region $V \subset U$, where $\mathbf{N}$ is the outward normal along ∂V in the Lagrangian coordinates, and $\mathbf{n}$ is the outer normal along $\partial\chi$. By using the Nanson's formula relating the current and the reference element of the surface area, the passive part of total Cauchy stress $\boldsymbol{\sigma}^{\mathrm{p}}$ is given by

$$\sigma^{\mathrm{p}} = J^{-1}\mathbb{P}^{s}\mathbb{F}^{T}, \tag{2.13}$$

where $J = \det(\mathbb{F})$ is the structural deformation.

The passive elastic property of the myocardium is described by a hyperelastic Holzapfel–Gasser–Ogden (HGO) stain energy function W [47], first given by Holzapfel and Ogden,

in terms of invariants of the right Cauchy-Green deformation tensor $\mathbb{C} = \mathbb{F}^T\mathbb{F}$,

$$W = \frac{a}{2b}e^{b(I_1-3)} + \sum_{i=\mathrm{f,s}} \frac{a_i}{2b_i}\left(e^{b_i(I_{4i}^*-1)^2} - 1\right) + \frac{a_{\mathrm{fs}}}{2b_{\mathrm{fs}}}\left(e^{b_{\mathrm{fs}}(I_{8\mathrm{fs}})^2} - 1\right), \tag{2.14}$$

where a, b, a_i and b_i ($i = \mathrm{f}, \mathrm{s}$ and fs) are material parameters and $I_1 = \mathrm{tr}(\mathbb{C})$, $I_{4\mathrm{f}} = \mathbf{f}_0^T\mathbb{C}\mathbf{f}_0 = \mathbf{f}\cdot\mathbf{f}$, $I_{4\mathrm{s}} = \mathbf{s}_0^T\mathbb{C}\mathbf{s}_0 = \mathbf{s}\cdot\mathbf{s}$, $I_{8\mathrm{fs}} = \mathbf{f}_0^T\mathbb{C}\mathbf{s}_0 = \mathbf{f}\cdot\mathbf{s}$, and $I_{4i}^* = \max(I_{4i}, 1)$. Here $\mathbf{f}_0$ and $\mathbf{s}_0$ are the initial fibre and sheet directions.

In this study, the passive and active material parameters in the LV region are determined by fitting both the end-diastolic and end-systolic LV cavity volumes, and the myocardial strains to the MR imaging measurements.

The myocardial fibre generation is based on the work of Potse et al. [101]; the fibre angles rotates from -60° to 60° from the endocardium to the epicardium, and the sheet angle rotates from -45° to 45°, thereby corresponding to a normal healthy LV[66] as shown is Fig. 2.1.

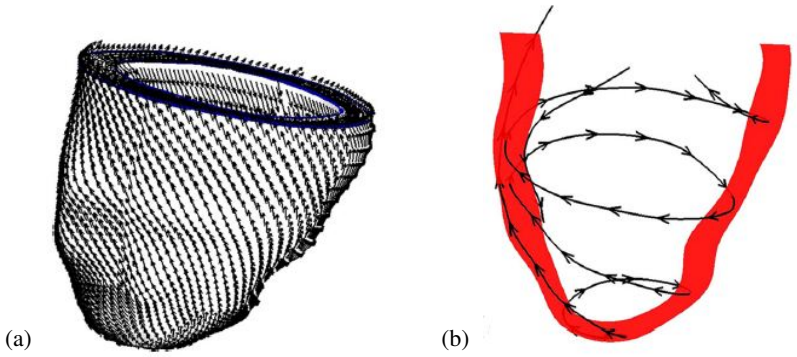

Figure 2.1: The rule-based fiber architecture of the LV (a) and the fiber tracing (b)Gao et al. [34].

The active stress response

The active stress of myocardium comes from the active contractions of the myocardium fibers,

$$\sigma^a = T\mathbf{f}\otimes\mathbf{f}, \tag{2.15}$$

where T is the active contractile tension force determined by the active contraction model of Niederer et al. [83], which describes the active tension as a function of the intracellular calcium concentration $[\mathrm{Ca}]_i$, the fibre stretch λ_{f}, and the changing rate of fibre stretch.

The dynamics of the concentration of tropnin-bound calcium $[\mathrm{Ca}]_{\mathrm{trpn}}$ is given by

$$\frac{d[\mathrm{Ca}]_{\mathrm{trpn}}}{dt} = k_{\mathrm{on}}[Ca]_i([\mathrm{Ca}]_{\mathrm{trpn,max}} - [\mathrm{Ca}]_{\mathrm{trpn}}) - k_{\mathrm{off}}[\mathrm{Ca}]_{\mathrm{trpn}}, \tag{2.16}$$

$$k_{\mathrm{off}} = k_{\mathrm{off,ref}}\left(1 - \frac{T}{\gamma T_{\mathrm{ref}}}\right), \tag{2.17}$$

where k_{on} and k_{off} are the binding and unbinding rates, $k_{\mathrm{off,ref}}$ is the unbinding rate in absence of the active tension, T is the active tension and T_{ref} is the maximum active tension at the resting sarcomere length. The value of parameter is given by Niederer et al. [83], $k_{\mathrm{on}} = 100\,\mu\mathrm{M}^{-1}\mathrm{s}^{-1}$, $k_{\mathrm{off,ref}} = 200\,\mathrm{s}^{-1}$, $[\mathrm{Ca}]_{\mathrm{trpn,max}} = 70\,\mu\mathrm{M}$, In this model, we define

$$T_{\mathrm{ref}} = T_{\mathrm{scale}} \times 56.2\,\mathrm{kPa}, \tag{2.18}$$

where T_{scale} is a dimensionless scale factor determined by matching the end-systolic volume of the LV to the in vivo LV volume.

2.1.2 LV geometry

The geometry of the LV model is reconstructed from the cardiac magnetic resonance (CMR) images performed on a healthy volunteer (male, age 28) Gao et al. [32]. The basic CMR imaging protocol is as follows: slice thickness= 10 mm, in-plane pixel size= $1.3 \times 1.3\,\mathrm{mm}^2$, and frame rate= 25 per cardiac cycle. Three directions of the steady-state free precession cine images are used for functional assessment, i.e. the short-axis, horizontal long-axis, and vertical long-axis planes. Seven slices of short-axis images from base to apex at early diastole (the lowest pressure in the LV) are used for the LV reconstruction (Fig. 2.2(a)). Long-axis slices are used for reconstructing the inflow (left atrium) and the outflow (aorta) tracts. The rebuilt LV is shown in Fig. 2.2(b).

In order to simulate the ventricular flow, the inflow and outflow tracts are also reconstructed as shown in Fig. 2.3 using long-axis MR images. The valvular region between the valvular rings and the LV base is derived from MR images; the regions above the two valvular rings are artificial extensions with fixed elliptical openings at the top of the computational box (Fig. 2.3). The region below the LV base is allowed to actively contract.

In this study, because only the LV region can actively contract, we fix the longitudinal and circumferential displacements of the LV base, but allow the radial expansion. The remainding LV region is free to move, including the apex. We assume the valvular region

(a) (b)

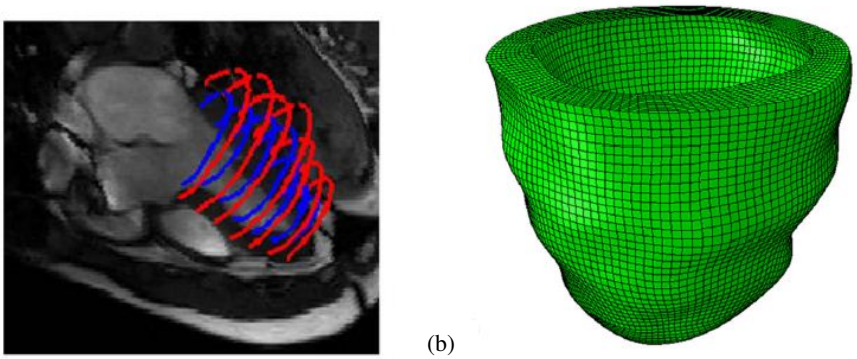

Figure 2.2: The LV geometry reconstruction: (a) the endocardial and deformed boundary segments of the LV; (b) the rebuilt LV mesh with 135,430 tetrahedral elements Gao et al. [32].

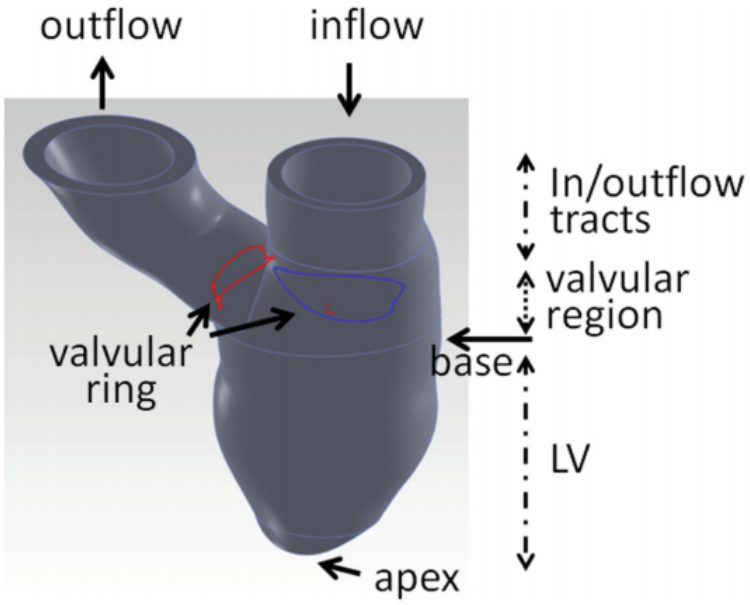

Figure 2.3: Reconstructed LV model with inflow and outflow tracts Gao et al. [35].

can only bear passive loads, and is much softer than the LV region. Since this model does not include the aortic and mitral valves, specific boundary conditions applied on the outlet plane of the two tracts are used to mimic the function of the valves as follows.

2.1.3 Boundary condition

In this study, the LV model is immersed in a 17 cm $\times$ 16 cm $\times$ 16.5 cm fluid box, with inflow and outflow tracts attached to the top plane of the fluid box (Fig. 2.4). The geome-

tries of the two tracts above the valvular rings in Fig. 2.3 are not derived from the MR images; they are the artificial extensions for applying flow boundary conditions.

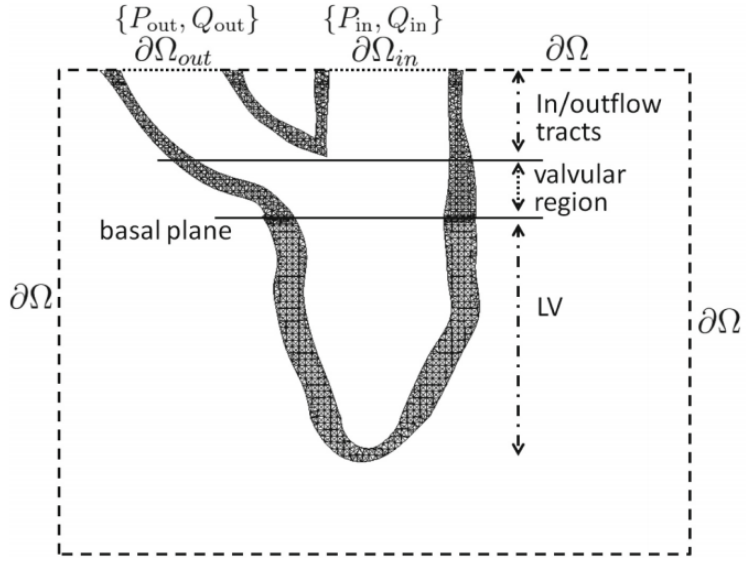

Figure 2.4: Schematic illustration of boundary conditions of the IB/FE LV model. $\partial_{\text{in}}/\partial_{\text{out}}$ denote the inflow/outflow boundary, and $P_{\text{in}}/P_{\text{out}}$, $Q_{\text{in}}/Q_{\text{out}}$ are the pressure and volumetric flow rate at the inlet/outlet boundary $\partial\Omega_{\text{in}}/\partial\Omega_{\text{out}}$, respectively.

During diastole, a maximum displacement of 6 mm is allowed for the valvular region (Fig. 2.4); beyond that, a tethering force is applied to avoid further deformations. During systole, the valvular region is gradually pulled back to the original position. The interface between the valvular region and the LV base follows the LV base's motion. The inflow and outflow tracts are fixed during the simulations.

For the fluid region, zero pressure and zero tangential slip are applied at the boundary box $\partial\Omega$(Fig. 2.5)

$$\mathbf{u} \cdot \mathbf{t} = \mathbf{0}, \quad \mathbf{p} = \mathbf{0}. \tag{2.19}$$

where $\mathbf{u}$ is the Eulerian velocity and $\mathbf{t}$ is the unit tangential vector.

The boundary conditions applied on the top planes of the inflow and outflow tracts vary for the four cardiac phases, i.e. diastolic filling, isovolumetric contraction, systolic ejection and relaxation. In detail, the boundary conditions are

- Diastolic filling: for the LV region immersed in the fluid domain Ω (Fig. 2.5), a time-

dependent linearly ramped pressure, from 0 mmHg to the end-of-diastolic pressure $P_{\text{ED-LV}}$, is directly applied to the endocardial surface $\partial\Omega^s(t)$ of the LV region [60, 123, 127]

$$\mathbf{p}_{\text{loading}} = t/0.8 \times P_{\text{ED-LV}}, \quad 0 < t \leqslant 0.8\,\text{s}. \tag{2.20}$$

Boundary conditions for the inlet and outlet region are

$$\mathbf{u}_{\text{out}}(t) = \mathbf{0}, \quad p_{\text{in}}(t) = 0, \quad 0 < t \leqslant 0.8\,\text{s}. \tag{2.21}$$

- Isovolumetric contraction: the aortic valve and mitral valve are fully closed during the isovolumetric contraction, and the boundary conditions are

$$\mathbf{u}_{\text{out}}(t) = \mathbf{u}_{\text{in}}(t) = \mathbf{0}, \quad 0.8 < t \leqslant 0.84\,\text{s}. \tag{2.22}$$

- Systolic ejection: The aortic valve is assumed to open at 0.84 s, and a three-element windkessel model is used to provide a pressure boundary condition at the outlet boundary plane (Fig. 2.6)

$$p_{\text{out}} = p_{\text{WK}} \tag{2.23}$$

where p_{WK} is calculated by a windkessel circulation model [39]. When the backflow occurs at the outlet boundary plane ($q_{\text{out}} < 0$), the aortic valve is closed.

- Relaxation: The relaxation ends when the total duration for the four phases is 1.2 s. The boundary condition during relaxation is

$$\mathbf{u}_{\text{out}} = \mathbf{u}_{\text{in}} = \mathbf{0}. \tag{2.24}$$

Before starting the next cardiac cycle, we allow the LV model to be fully relaxed within a further duration of 0.8 s, during which the active tension is set to be zero, $\mathbf{u}_{\text{out}} = \mathbf{0}$ and $p_{\text{in}} = 0$. The blood can move freely in or out of the LV cavity through the mitral valve.

2.1.4 Numerical solutions

In the numerical implementation of the IB/FE LV model, the Eulerian equations of motion are discretized by a finite difference method, and the Lagrangian equations are discretized with a finite element method [40].

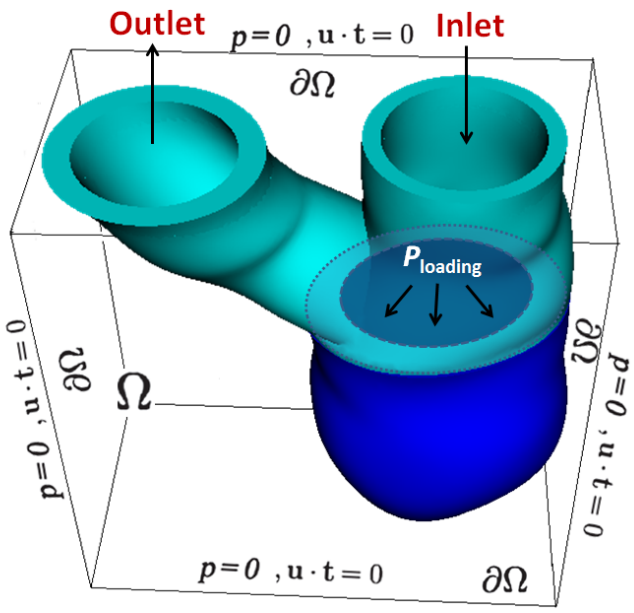

Figure 2.5: Illustration the loading pressure and boundary conditions applied to the LV model, reconstructed from Gao et al. [34]. The whole computational domain is represented by the black box with zero pressure and zero tangential slip along $\partial\Omega$, where $\mathbf{u}$ is the Eulerian velocity and $\mathbf{t}$ is the unit tangential vector. The LV cavity pressure loading $\mathbf{p}_{\text{loading}}$ is applied to the endocardial surface.

2.1.5 Parameters in the LV model

A time step size of $\Delta t = 1.22 \times 10^{-4}$ s is used in the diastolic and relaxation phases because of the explicit time stepping scheme employed by our implementation. The highly dynamic LV deformation and ventricular flow in systole require even smaller time steps, we use $0.25\,\Delta t$ in the early systole (0.1 s), and $0.125\,\Delta t$ in the left systolic phase.

A population-based end-of-diastolic pressure, $P_{\text{ED-LV}}$ =8 mmHg is chosen in (2.20), since it is impossible to measure the $P_{\text{ED-LV}}$ in a healthy volunteer.

The passive material parameters for the healthy LV in (2.14) are $a = 0.19$ kPa, $b = 5.08$, $a_f = 1.2$ kPa, $b_f = 4.15$, $a_{fs} = 0.24$ kPa, $b_{fs} = 1.3$. The scale factor for the active contractile tension force in (2.18) is chosen as $T_{\text{scale}} = 4$.

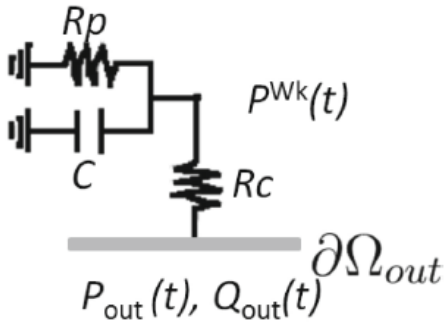

Figure 2.6: A three-element windkessel model is used as a boundary condition on the outlet boundary plane of the LV Gao et al. [35]. In the windkessel model, R_c denotes the characteristic resistance, R_p denotes the peripheral resistance and C denotes the arterial compliance. In the simulations, $R_c = 0.033$ (mmHg ml^{-1} s), $R_p = 0.79$ (mmHg ml^{-1} s) and $C = 1.75$ (ml mmHg^{-1}).

2.2 The systemic arteries model

As discussed in the previous chapter, the diameter of the blood vessels vary dramatically from the aorta to capillaries, and it is not feasible to include all the vessels to construct a mathematical model, since the number of vessels is too large for computational purposes. Therefore, only large and small arteries, i.e. those with a diameter larger than 100μm, are considered in this model. The geometry of large arteries including radius and length can be obtained from clinical measurements, such as MR images or CT scans, while the dimensions of the smaller arteries can also be measured, but due to their large number it is practically impossible to measure them all. Therefore, we model the larger arteries as structured trees based on measured data and model the smaller arteries in a simpler way as asymmetric structured tree tapering around 19 generations to reach the minimum radius 100μm.

2.2.1 Modelling of the large arteries

The large arteries are modelled as a bifurcating tree, in which each individual vessel is tapering along their length. The modelling of the large arteries are based on the following assumptions:

- The arteries in both sides of the body are symmetric and they are modelled identically, i.e. those vessels which are existing in both the left and right side of the body have the same dimensions. Hence, for these symmetric vessels with the same inflow, such as the iliac and femoral arteries, the pressure and flow rate are only calculated once for one side, and the other side is the same.
- The two coronary arteries, the intercostal arteries and the arteries branching from the celiac axis, and various branches from the subclavian, brachial, and carotid vessels have been neglected for computational reasons, since the flow rate in these vessels are much smaller than that of the other arteries.

Fluid dynamics of the large arteries

A typical vessel is modelled as an axisymmetric compliant cylinder with a rotation symmetric tubular surface S and two end-surfaces at $x = 0$ and $x = L$ (Fig. 2.7). We assume that:

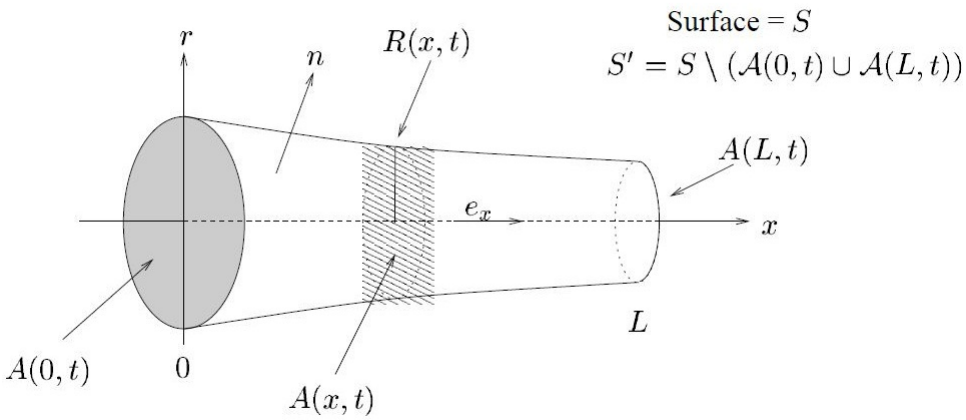

Figure 2.7: A tapering tube model of a typical vessel [88].

- S denotes the surface of a typical vessel, and $S' = S\backslash(A(0,t) \cup A(L,t))$ denotes the surface excluding the two boundary planes $A(0,t)$ and $A(x,t)$.
- The velocity of the surface S is $\boldsymbol{v} = (v_x(x,r,t), v_r(x,r,t))$, where x is the longitudinal coordinate and r is the radial coordinate.
- The velocity of the fluid enclosed within S is denoted by $\boldsymbol{u} = (u_x(x,r,t), u_r(x,r,t))$, where u_r is the radial velocity, and u_x is the axial velocity.

- The blood vessel wall is assumed to be impermeable, and applies the no-slip condition.
- The pressure of the fluid $p(x,t)$ is approximately independent of r. p_0 represents the diastolic pressure, which is constant during the simulation.

The conversation of volume gives:

$$\frac{\partial}{\partial t}\iiint_V dV + \iint_S (\boldsymbol{u}-\boldsymbol{v})\cdot\boldsymbol{n}\,dA = 0 \tag{2.25}$$

$$\Leftrightarrow \quad \frac{\partial}{\partial t}\int_0^L \left(\iint_A dA\right) dx + \iint_{A(0)\cup A(L)} (\boldsymbol{u}-\boldsymbol{v})\cdot\boldsymbol{n}\,dA + \iint_{S'} (\boldsymbol{u}-\boldsymbol{v})\cdot\boldsymbol{n}\,dA = 0 \tag{2.26}$$

$$\Leftrightarrow \quad \frac{\partial}{\partial t}\int_0^L A\,dx + \left[\iint_A u_x\,dA\right]_0^L + \iint_{S'} (\boldsymbol{u}-\boldsymbol{v})\cdot\boldsymbol{n}\,dA = 0. \tag{2.27}$$

where $A(x,t) = \pi r(x,t)^2$ is the cross-sectional area, and $\boldsymbol{n}$ is the outward unit normal to the surface S. Since we assume the wall moves with the fluid, i.e. $\mathbf{u} = \mathbf{v}$ on S', thus the last term in (2.27) vanish. By differentiating (2.27) with respect to L, and replacing L by x throughout gives

$$\frac{\partial A}{\partial t} + \frac{\partial}{\partial x}\iint_A u_x\,dA = 0 \tag{2.28}$$

where u_x is the axial velocity. The average velocity over the cross-sectional area is defined as

$$u = \frac{1}{A}\iint_A u_x\,dA. \tag{2.29}$$

By putting (2.29) into (2.28), we get

$$\frac{\partial A}{\partial t} + \frac{\partial (Au)}{\partial x} = 0 \tag{2.30}$$

With the term of flow rate $q = Au$, (2.30) can be written as

$$\frac{\partial A}{\partial t} + \frac{\partial q}{\partial x} = 0 \tag{2.31}$$

which is the one-dimensional continuity equation we need.

The conservation of x-momentum gives

$$\frac{\partial}{\partial t}\iiint_V \rho u_x\,dV + \iint_S \rho u_x (\boldsymbol{u}-\boldsymbol{v})\cdot\boldsymbol{n}\,dA + \iint_S (p(\boldsymbol{n}\cdot\boldsymbol{e_x}) - (\boldsymbol{dn})\cdot\boldsymbol{e_x})\,dA = 0 \tag{2.32}$$

$$\Leftrightarrow \quad \frac{\partial}{\partial t}\int_0^L \left(\iint_A \rho u_x\,dA\right) dx + \left[\iint_A \rho u_x^2 dA\right]_0^L + \iint_{S'} (p(\boldsymbol{n}\cdot\boldsymbol{e_x}) - (\boldsymbol{dn})\cdot\boldsymbol{e_x})\,dA$$
$$+ \int_0^L \left(\iint_A \frac{\partial p}{\partial x} dA\right) dx - \int_0^L \left(\int_0^{2\pi} (\boldsymbol{dn})\cdot\boldsymbol{e_x} R\,d\theta\right) \sqrt{1+\left(\frac{\partial R}{\partial x}\right)^2}\,dx = 0, \tag{2.33}$$

where ρ is the density, $\boldsymbol{d}$ is a tensor representing the shear stresses, $R(x,t)$ is the radius of the vessel, and $\boldsymbol{e_x}$ is the unit vector in the x-direction. The same as previously, we assume the wall move with the fluid, so the third term in (2.33) vanish. In [88], by assuming the tapering is small and can be neglected, the last integral in (2.33) can be written as

$$\begin{aligned}\iint_S (\boldsymbol{dn})\cdot\boldsymbol{e_x} &= \int_0^L \left(\int_0^{2\pi} (\boldsymbol{dn})\cdot\boldsymbol{e_x} R\,d\theta\right)\sqrt{1+\left(\frac{\partial R}{\partial x}\right)^2}\,dx \\ &= \int_0^L 2\pi\mu R\left[-2\frac{\partial u_x}{\partial x}\frac{\partial R}{\partial x}+\frac{\partial u_x}{\partial r}\right]_R dx, \end{aligned} \tag{2.34}$$

where μ is the viscosity. By putting (2.34) into (2.33), and differentiating it with respect to L, we get

$$\frac{\partial}{\partial t}\iint_A \rho u_x\,dA+\frac{\partial}{\partial x}\iint_A \rho u_x^2\,dA+\iint_A \frac{\partial p}{\partial x}\,dA-2\pi\mu R\left[-2\frac{\partial u_x}{\partial x}\frac{\partial R}{\partial x}+\frac{\partial u_x}{\partial r}\right]_R = 0. \tag{2.35}$$

With (2.29) and

$$\chi = \frac{1}{Au^2}\iint_A u_x^2\,dA. \tag{2.36}$$

(2.35) can be writen as

$$\rho\left(\frac{\partial(Au)}{\partial t}+\frac{\partial(\chi Au^2)}{\partial x}\right)+A\frac{\partial p}{\partial x}-2\pi\mu R\left[-2\frac{\partial u_x}{\partial x}\frac{\partial R}{\partial x}+\frac{\partial u_x}{\partial r}\right]_R = 0. \tag{2.37}$$

For laminar flow in slightly tapering vessel, the velocity profile is rather flat [61, 92], so that it can be assumed to be flat in the center but with a thin boundary layer of thickness δ (Fig. 2.8), hence

$$u_x = \begin{cases} u, & \text{for} \quad r \le R-\delta \\ u(R-r)/\delta & \text{for} \quad R-\delta < r \le R, \end{cases} \tag{2.38}$$

where $\delta = (\nu T)^{1/2} \approx 0.2$ cm for the aorta, in which $\nu = \mu/\rho$ is the kinematic viscosity. In this case, again ignoring the small tapering, i.e. neglect the terms of order $\left(\frac{\partial R}{\partial x}\right)^2$, the last term in (2.37) can be write as

$$-2\pi\mu R\left[-2\frac{\partial u_x}{\partial x}\frac{\partial R}{\partial x}+\frac{\partial u_x}{\partial r}\right]_R \approx \frac{2\pi\mu u R}{\delta}, \tag{2.39}$$

and

$$\chi = \frac{1}{Au^2}\left(\int_0^{R-\delta} u^2 2\pi r\,dr+\int_{R-\delta}^{R}\left(\frac{u(R-r)}{\delta}\right)^2 2\pi r\,dr\right) = 1-\frac{4\delta}{3R}+\frac{\delta^2}{2R^2}\approx 1. \tag{2.40}$$

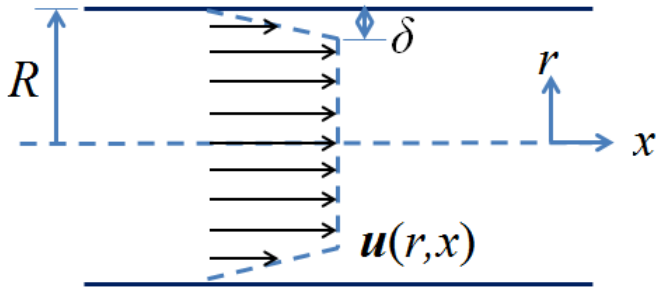

Figure 2.8: The velocity profile of the laminar flow in a typical vessel, with the assumption that the velocity $\mathbf{u}(r,x)$ is flat in the center with a thin boundary layer of thickness δ.

Then, (2.37) becomes

$$\frac{\partial(Au)}{\partial t}+\frac{\partial(Au^2)}{\partial x}+\frac{A}{\rho}\frac{\partial p}{\partial x}+\frac{2\pi\nu uR}{\delta}=0. \tag{2.41}$$

Finally, the momentum equation can be rewritten in terms of the flow $q=Au$,

$$\frac{\partial q}{\partial t}+\frac{\partial}{\partial x}\left(\frac{q^2}{A}\right)+\frac{A}{\rho}\frac{\partial p}{\partial x}+\frac{2\pi\nu uR}{\delta}=0. \tag{2.42}$$

Equations (2.31) and (2.42) are the basic equations for the one-dimensional theory for the wave propagation in the arteries. In order to solve for the three dependent variables, namely p, q and A, we need a third equation, the state equation, giving the relation between the pressure and the cross-sectional area, which is derived from the linear theory of elasticity. Assuming that the vessels are circular, that the thickness of the walls are much less than the radius ($h/r_0 \gg 1$), and the loading and deformation are axisymmetric, the external forces can be reduced to a circumferential tensile stress in the form

$$\tau=\frac{r(p-p_0)}{h}=\frac{E}{(1-\sigma_x\sigma_\theta)}\frac{(r-r_0)}{r_0}, \tag{2.43}$$

where $(r-r_0)/r_0$ is the corresponding circumferential strain, and $\sigma_x=\sigma_\theta=0.5$ are the Poisson ratios in the circumferential and longitudinal directions. Solving this equation for $p(x,t)-p_0$ yields

$$p(r_0,A)\equiv p(x,t)-p_0=\frac{4}{3}\frac{Eh}{r_0}\left(1-\sqrt{\frac{A_0}{A}}\right), \tag{2.44}$$

where $A_0=\pi r_0^2$ is the cross-sectional area and r_0 is the radius when $p=p_0$, and the term Eh/r_0 is given in (2.93).

The continuity equation (2.31) and the momentum equation (2.42) cannot be solved analytically, so a numerical method is needed. Before solving them numerically, they need to be written in the conservation form. We introduce

$$B(r_0(x), p(x,t)) = \frac{1}{\rho}\int A\,dp, \tag{2.45}$$

so that

$$\frac{\partial B}{\partial x} = \frac{A}{\rho}\frac{\partial p}{\partial x} + \frac{\partial B}{\partial r_0}\frac{dr_0}{dx}. \tag{2.46}$$

By adding (2.46) on both sides of (2.42), the momentum equation becomes

$$\frac{\partial q}{\partial t} + \frac{\partial}{\partial x}\left(\frac{q^2}{A} + B\right) = -\frac{2\pi\nu u R}{\delta} + \frac{\partial B}{\partial r_0}\frac{dr_0}{dx}, \tag{2.47}$$

where $\frac{\partial B}{\partial r_0}\frac{dr_0}{dx}$ does not contain any partial derivatives of p, and hence of A and q , so it can be evaluated directly. Combining (2.31) and (2.47) with the state equation (2.44), the total system equations can be written in the conservation form

$$\frac{\partial}{\partial t}\begin{pmatrix} A \\ q \end{pmatrix} + \frac{\partial}{\partial x}\begin{pmatrix} q \\ \frac{q^2}{A} + \frac{f}{\rho}\sqrt{A_0 A} \end{pmatrix} = \begin{pmatrix} 0 \\ -\frac{2\pi\nu q R}{\delta A} + \frac{1}{\rho}(2\sqrt{A}(\sqrt{\pi}f + \sqrt{A_0}\frac{df}{dr_0}) - A\frac{df}{dr_0})\frac{dr_0}{dx} \end{pmatrix}, \tag{2.48}$$

where $f = \frac{4Eh}{3r_0}$. In this work, these equations are solved numerically using a two-step LaxWendroff scheme [90].

2.2.2 Numerical solutions for the large arteries

The fluid dynamic equations for the large arteries are (2.31) and (2.33), and with the state equation (2.44), we get the conservation form shown in (2.48). Before we solve these equations, it is convenient to rewrite them in dimensionless form. In order to do this, we use three characteristic parameters r_c, q_c and ρ to determine the following dimensionless variables

$$\tilde{x} = \frac{x}{r_c} \quad \tilde{t} = \frac{t q_c}{r_c^3} \quad \tilde{r} = \frac{r}{r_c} \tag{2.49}$$

$$\tilde{A} = \frac{A}{r_c^2} \quad \tilde{q} = \frac{q}{q_c} \quad \tilde{p} = \frac{p r_c^4}{\rho q_c^2} \tag{2.50}$$

where $r_c = 1\,\mathrm{cm}$ denotes the characteristic radius of the vessels, $q_c = 10\,\mathrm{cm}^3\,\mathrm{s}^{-1}$ denotes the characteristic flow rate, and $\rho = 1.06\,\mathrm{g\,s}^{-3}$ is the density of the blood. Then, the

non-dimensional continuity equation and the momentum equation can be written in the following form

$$\frac{\partial \tilde{A}}{\partial \tilde{t}} + \frac{\partial \tilde{q}}{\partial \tilde{x}} = 0 \tag{2.51}$$

$$\frac{\partial \tilde{q}}{\partial \tilde{t}} + \frac{\partial}{\partial \tilde{x}}\left(\frac{\tilde{q}^2}{\tilde{A}}\right) + \tilde{A}\frac{\partial \tilde{p}}{\partial \tilde{x}} = -\frac{2\pi\tilde{r}}{\delta \mathscr{R}}\frac{\tilde{q}}{\tilde{A}} \tag{2.52}$$

where $\mathscr{R}$ is the Reynolds number $\mathscr{R} = \rho q_c/(\mu r_c) = q_c/(\nu r_c)$. Combined with the state equation (2.44), the conservation form is

$$\frac{\partial}{\partial \tilde{t}}\begin{pmatrix}\tilde{A}\\ \tilde{q}\end{pmatrix} + \frac{\partial}{\partial \tilde{x}}\begin{pmatrix}\tilde{q}\\ \frac{\tilde{q}^2}{\tilde{A}} + f\sqrt{\tilde{A}_0\tilde{A}}\end{pmatrix} = \begin{pmatrix}0\\ -\frac{2\pi\tilde{r}}{\delta\mathscr{R}}\frac{\tilde{q}}{\tilde{A}} + (2\sqrt{\tilde{A}}(\sqrt{\pi}f + \sqrt{\tilde{A}_0}\frac{df}{d\tilde{r}_0}) - \tilde{A}\frac{df}{d\tilde{r}_0})\frac{d\tilde{r}_0}{d\tilde{x}}.\end{pmatrix}. \tag{2.53}$$

If we drop the tildes, these equations can be rewritten as follows

$$\frac{\partial}{\partial t}\mathbf{U} + \frac{\partial}{\partial x}\mathbf{R} = \mathbf{S} \tag{2.54}$$

where $\mathbf{U}$, $\mathbf{R}$ and $\mathbf{S}$ are given by

$$\mathbf{U} = (A, q), \tag{2.55}$$

$$\mathbf{R} = (R_1, R_2) = \left(q, \frac{q^2}{A} + f\sqrt{A_0 A}\right), \tag{2.56}$$

$$\mathbf{S} = (S_1, S_2) = \left(0, -\frac{2\pi\nu qR}{\delta A} + \frac{1}{\rho}\left(2\sqrt{A}\left(\sqrt{\pi}f + \sqrt{A_0}\frac{df}{dr_0}\right) - A\frac{df}{dr_0}\right)\frac{dr_0}{dx}\right). \tag{2.57}$$

Richtmeyer's two-step version of the Lax–Wendroff scheme

In this work, these equations are solved numerically using Richtmeyer's two-step version of the Lax–Wendroff explicit scheme Peskin [97]. When discritising varables, $\mathbf{U}_m^n = \mathbf{U}(m\Delta x, n\Delta t)$, in which $m = 0, , 1 ..., M$, $n = 0, , 1 ..., N$, $\Delta x = L/M$ where L is the length of the vessel and M is the number of points along the x-axis, and $\Delta t = T/N$ where T is the length of period and N is the number of time-steps in the period.

- **Interior points**

The solutions for the interior points (excluding boundary) are determined by four intermediate points at half step $(m+1/2, n+1/2)$ as follows (Fig. 2.9)

$$\mathbf{U}_m^{n+1} = \mathbf{U}_m^n - \frac{\Delta t}{\Delta x}\left(\mathbf{R}_{m+1/2}^{n+1/2} + \mathbf{R}_{m-1/2}^{n+1/2}\right) + \frac{\Delta t}{2}\left(\mathbf{S}_{m+1/2}^{n+1/2} + \mathbf{S}_{m-1/2}^{n+1/2}\right), \tag{2.58}$$

where $\mathbf{R}^{n+1/2}_{m\pm1/2}$ and $\mathbf{R}^{n+1/2}_{m\pm1/2}$ are determined by (2.56) and (2.57) using two intermediate points at step $(m\pm1/2, n+1/2)$. Then $\mathbf{U}^{n+1/2}_{m\pm1/2}$ can found by the following scheme

$$\mathbf{U}^{n+1}_{j} = \frac{\mathbf{U}^{n}_{j+1/2}+\mathbf{U}^{n}_{j-1/2}}{2} + \frac{\Delta t}{2}\left(-\frac{\mathbf{R}^{n}_{j+1/2}+\mathbf{R}^{n}_{j-1/2}}{h} + \frac{\mathbf{S}^{n+1/2}_{m+1/2}+\mathbf{S}^{n+1/2}_{m-1/2}}{2}\right). \tag{2.59}$$

where $j = m+1/2, m-1/2$.

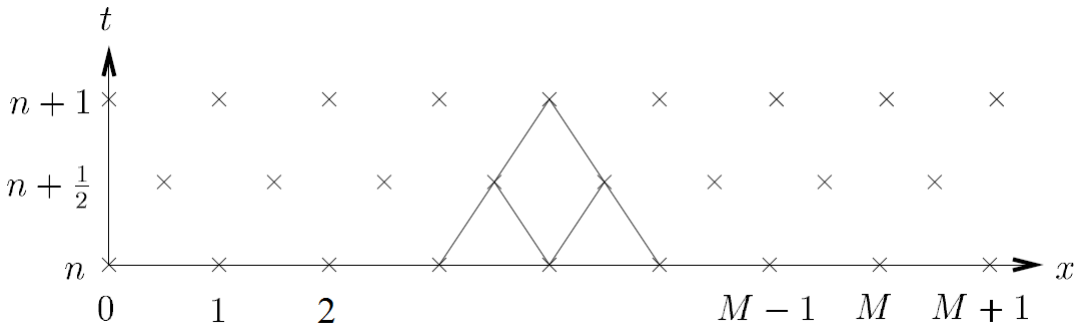

Figure 2.9: Richtmeyer's two-step version of the Lax–Wendroff scheme for the interior points [90]. The intermediate points are determined for calculating Q and A at $n+1$ time step.

- **Inflow boundary condition**

From (2.53), the cross-sectional area A is determined by q at the boundary. For Lax–Wendroff scheme at the inlet boundary, all variables marked with a cross are known (Fig. 2.10). In order to determine A^{n+1}_a, $q^{n+1/2}_{-1/2}$ needs to be evaluated. At the $(n+1)^{\text{st}}$ time step, we introduce a ghost point $q^{n+1/2}_{-1/2}$ marked with a circle in Fig. 2.10

$$q^{n+1/2}_{0} = \frac{1}{2}\left(q^{n+1/2}_{-1/2} + q^{n+1/2}_{1/2}\right) \tag{2.60}$$

$$\Leftrightarrow \quad q^{n+1/2}_{-1/2} = 2q^{n+1/2}_{0} - q^{n+1/2}_{1/2}. \tag{2.61}$$

Then A^{n+1}_a can be found from (2.53),

$$A^{n+1}_a = A^{n}_a - \frac{\Delta x}{\Delta t}\left(q^{n+1/2}_{a+1/2} + q^{n+1/2}_{a-1/2}\right). \tag{2.62}$$

Then the value of $\bar{p}^{n+1}_0$ is determined by the conservation equations.

Since the inflow boundary condition changes when the two models are coupled, this part will be redefined in detail in the next chapter.

- **Outflow boundary condition**

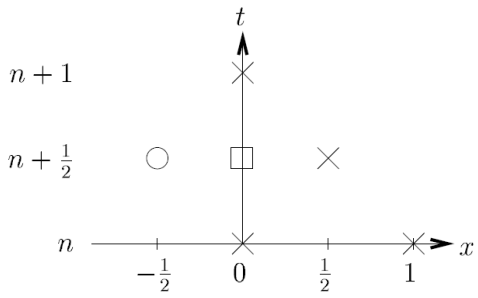

Figure 2.10: The Lax-Wendroff scheme at the inlet boundary in the systemic circulation model. All known variables are marked with crosses; the ghost point is marked with a circle; the boundary condition is applied at the point marked with a square.

The outflow boundary condition for each terminal large artery is determined by the convolution integral in (2.90).

- **Bifurcation condition**

At each bifurcation, we assuming that there is no leakage, the outflow from any parent vessel p_p at the outlet $x = L_p$ must be balanced by the inflows into the two daughter vessels q_{d_1}, q_{d_2} at the inlet $x = 0$ for each vessel (Fig. 2.11),

$$q_p = q_{d_1} + q_{d_2}, \tag{2.63}$$

and with the continuity of the pressure, we have

$$p_p = p_{d_1} = p_{d_2}. \tag{2.64}$$

2.2.3 Modelling of the small arteries

The diameters of the small arteries are approximately 2000–30 μm, from the aorta to the arterioles, it will have approximately 26 generations if the arteries are bifurcating as a binary tree [88]. It is practically infeasible to deal with such a huge amount of vessels, so we model them in a structured and optimal way, i.e. an asymmetric structured tree (Fig. 2.12), and without tapering along each vessel, so that p is a function of A only. In this case, the structured trees do not mimic the real geometry of the vessels, but are based on general statistical relationships estimated from literature data [55, 110].

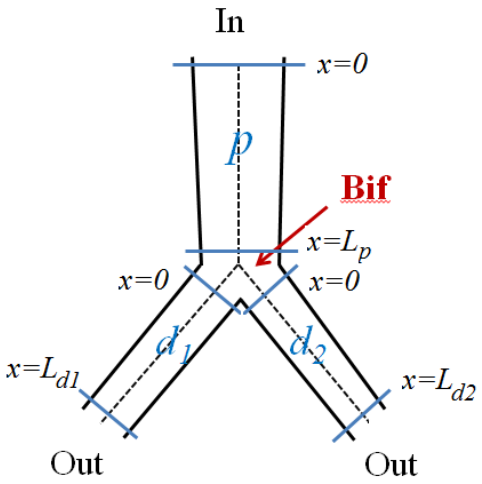

Figure 2.11: Illustrating the boundary conditions at the bifurcation, in which the subscript p denote the parent vessel, and d_1, d_2 denote the two daughter vessels. The boundary condition is applied between the outlet plane $x = L_p$ in the parent vessel and the inlet planes $x = 0$ in the daughter vessels with conservation of flow, $q_p = q_{d_1} + q_{d_2}$,, and continuity of the pressure, $p_p = p_{d_1} = p_{d_2}$.

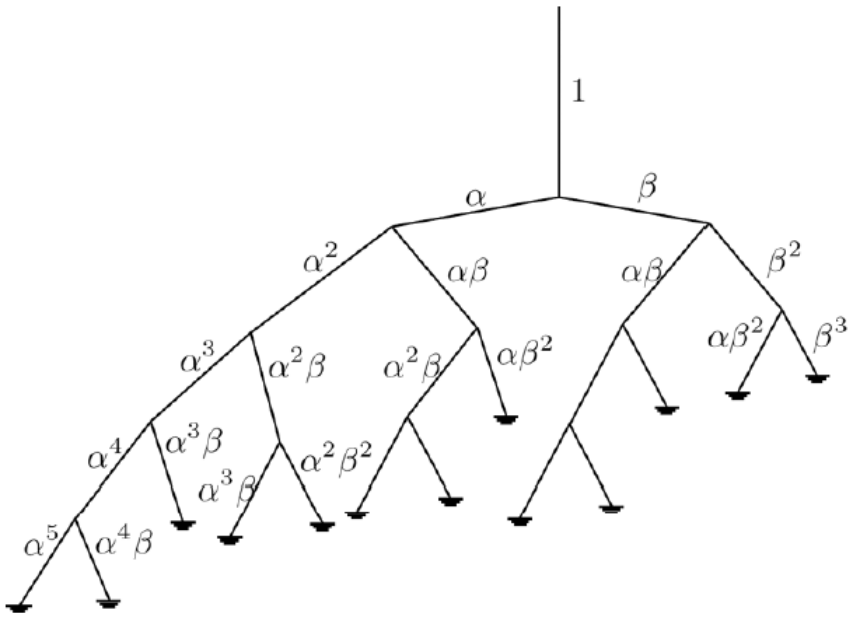

Figure 2.12: The structured-tree model for the small artery, and at each bifurcation the radii of the daughter vessels are scaled by a factor α and β, respectively [91].

- **Fluid dynamics of the small arteries**

Since the amount of each group of small arteries is huge, it is not computationally feasible to solve a non-linear model for such a big number of vessels. A further simplification is to linearize the model. Based on a previous study originally suggested by Womersley [132], [5], and [93], the small arteries is simulated as a linear hydrodynamic model. For axisymmetric flow with no swirl, the x-momentum equation can be write as

$$\frac{\partial u_x}{\partial t} + u_x \frac{\partial u_x}{\partial x} + u_r \frac{\partial u_x}{\partial r} + \frac{1}{\rho}\frac{\partial p}{\partial x} = \frac{\nu}{r}\frac{\partial}{\partial r}\left(r\frac{\partial u_x}{\partial r}\right). \tag{2.65}$$

We assume the radius of the vessel varies slowly with x, and then the second and third terms in (2.65) vanish, giving

$$\frac{\partial u_x}{\partial p} + \frac{1}{\rho}\frac{\partial p}{\partial x} = \frac{\nu}{r}\frac{\partial}{\partial r}\left(r\frac{\partial u_x}{\partial r}\right). \tag{2.66}$$

Since the propagation of the blood flow and pressure can be assumed to be periodic for each heart beat, and thus we can assume that all variables are periodic. Then, they can be written in the frequency domain using a Fourier series expansions of the form

$$u_x(r,x,t) = \sum_{k=-\infty}^{\infty} U_x(r,x,\omega_k)e^{i\omega_k t}, \tag{2.67}$$

$$p(x,t) = \sum_{k=-\infty}^{\infty} P(x,\omega_k)e^{i\omega_k t}, \tag{2.68}$$

$$q(x,t) = \sum_{k=-\infty}^{\infty} Q(x,\omega_k)e^{i\omega_k t}, \tag{2.69}$$

with Fourier coefficients given by

$$U_x(r,x,\omega_k) = \frac{1}{T}\int_{-T/2}^{T/2} u_x(r,x,t)e^{-i\omega_k t}dt, \tag{2.70}$$

$$P_x(x,\omega_k) = \frac{1}{T}\int_{-T/2}^{T/2} p(x,t)e^{-i\omega_k t}dt, \tag{2.71}$$

$$Q_x(x,\omega_k) = \frac{1}{T}\int_{-T/2}^{T/2} q(x,t)e^{-i\omega_k t}dt, \tag{2.72}$$

where $\omega_k = 2\pi k/T$ denotes the angular frequency. Hence, (2.66) becomes

$$i\omega U_x + \frac{1}{\rho}\frac{\partial P}{\partial x} = \frac{\nu}{r}\frac{\partial}{\partial r}\left(r\frac{\partial U_x}{\partial r}\right). \tag{2.73}$$

Since the tapering of the small vessels is neglected, the solution to (2.73) is given by

$$U_x = \frac{1}{i\omega\rho}\frac{\partial P}{\partial x}\left(1 - \frac{J_0(rw_0/r_0)}{J_0(w_0)}\right), \tag{2.74}$$

where $J_0(x)$ is the zeroth order Bessel function, and $w_0^2 = i^3 w^2$ ($w^2 = r_0^2 \omega/\nu$) is the Womersley number. Since the flow rate is given by

$$Q = 2\pi \int_0^{r_0} U_x r dr \quad \Leftrightarrow \quad i\omega Q + \frac{A_0}{\rho}\frac{\partial P}{\partial x}(1 - F_J) = 0, \tag{2.75}$$

where

$$F_J = \frac{2J_1(w_0)}{w_0 J_0(w_0)}. \tag{2.76}$$

The continuity equation for the small arteries is the same as the one used for the large arteries in (2.31), and similarly it can be transformed to

$$i\omega CP + \frac{\partial Q}{\partial x} = 0, \tag{2.77}$$

where C is the compliance which can be approximated by

$$C = \frac{dA}{dp} = \frac{3A_0 a}{2Eh}\left(1 - \frac{3pa}{4Eh}\right)^{-3} \approx \frac{3A_0 a}{2Eh}, \tag{2.78}$$

since $Eh \gg pa$. These equations (2.75) and (2.77) are used to simulate the pressure and flow propagations in the small arteries, and they can be solved analytically. By differentiating (2.75) with respect to x and inserting the result for $\frac{\partial Q}{\partial x}$ into (2.77) gives

$$\frac{\omega^2}{c^2}Q + \frac{\partial^2 Q}{\partial x^2} = 0 \quad or \quad \frac{\omega^2}{c^2}P + \frac{\partial^2 P}{\partial x^2} = 0 \tag{2.79}$$

where c is the wave propagation velocity

$$c = \sqrt{\frac{A_0(1 - F_J)}{\rho C}}. \tag{2.80}$$

The solutions of (2.79) take the form

$$Q(x, \omega) = a\cos(\omega x/c) + b\sin(\omega x/c), \tag{2.81}$$

$$P(x, \omega) = i\sqrt{\frac{\rho}{CA_0(1 - F_J)}}(-a\sin(\omega x/c) + b\cos(\omega x/c)), \tag{2.82}$$

where a and b are arbitrary constants of integration. This analytical solution provides a frequency-dependent relationship between the pressure and the flow rate in the form of an frequency dependent impedance

$$Z(x, \omega) = \frac{P(x, \omega)}{Q(x, \omega)}, \tag{2.83}$$

where P plays the role of voltage, Q plays the role of current as in an electrical networks. Hence, the impedance can be solved by

$$Z(x,\omega) = \frac{ig^{-1}(b\cos(\omega x/c) - a\sin(\omega x/c))}{a\cos(\omega x/c) + b\sin(\omega x/c)}, \tag{2.84}$$

where

$$g = \sqrt{CA_0(1-F_J)/\rho}. \tag{2.85}$$

Let $x = 0$ and $x = L$ in (2.84), the relation between the root impedance $Z(0,\omega)$ and the terminal impedance $Z(L,\omega)$ can be found as

$$Z(0,\omega) = \frac{ig^{-1}\sin(\omega L/c) + Z(L,\omega)\cos(\omega L/c)}{\cos(\omega L/c) + igZ(L,\omega)\sin(\omega L/c)}. \tag{2.86}$$

Thus, the input impedance for zero frequency can be found as

$$Z(0,0) = \lim_{\omega->0} Z(0,\omega) = \frac{8\mu l_{rr}}{\pi r_0^3} + Z(L,0), \tag{2.87}$$

where $l_{rr} = L/r_0$ is the length-to-radius ratio.

Boundary condition for the small arteries

- **Bifurcation condition**

At each bifurcation, the radii of the daughter vessels are scaled linearly by factors α (< 1) and β (< 1) relative to their parent vessel as shown in Fig. 2.12,

$$r_{d_1} = \alpha r_{\mathrm{p}}, \quad r_{d_2} = \beta r_{\mathrm{p}}, \tag{2.88}$$

where d_1 and d_2 denote the two daughter vessels, and p denote the parent vessel.

With the continuity of pressure and conservation of flow at each bifurcation shown in (2.64) and (2.63), the impedance relation can be written as

$$\frac{1}{Z_p} = \frac{1}{Z_{d_1}} + \frac{1}{Z_{d_2}} \tag{2.89}$$

where the subscript p refers to the patient vessel, and d_1, d_2 refer to two daughter vessels.

- **Outflow boundary condition**

From (2.89), if we know the impedance of all the terminal vessels, we can work out the root impedance by using (2.89) at each bifurcation from the bottom of the structured tree up to the top. Then the impedance $z(x,t)$ in the time domain can be calculated by inverse

Fourier transform for $Z(x,\omega)$, and an analytic relation between p and q can be get from the convolution theorem

$$p(x,t) = \int_{t-T}^{t} q(x,\tau)z(x,t-\tau)d\tau \tag{2.90}$$

which provides the outflow boundary condition at the end of each terminal large arteries.

2.2.4 Parameters in the systemic arterial model

- **Parameters for the large arteries**

The radius r of each tapering vessel follows an exponential curve with the tapering factor $k = \log(\frac{r_{\text{bot}}}{r_{\text{top}}})/L$ as follows,

$$r(x) = r_{\text{top}}\exp(kx) = r_{\text{top}}(\frac{r_{\text{bot}}}{r_{\text{top}}})^{x/L} \tag{2.91}$$

where r_{bot}, r_{top} are the bottom and top radii, and L is the length of the vessel, which are found from measurements for each vessel. The geometrical data for the proximal, distal radius and the length for each artery are listed in Table. 2.1, which are got from the MR images of a healthy volunteer Olufsen et al. [90].

Mathematically, the property of the arterial wall can be described by the volume compliance C in this form,

$$C = \frac{dV}{dP} \approx \frac{3A_0L}{2}\frac{r_0}{Eh} \tag{2.92}$$

where V is the volume of the segment, P is the pressure, r_0 is the radius, $A_0 = \pi r_0^2$ is the cross-sectional area, L is the length of the artery, E is the Young's modulus, and h is the wall thickness.In this equation, the term Eh/r_0 can be fitted to experiment data (Stergiopulos et al. [113]), and the fitted function has the form

$$\frac{Eh}{r_0} = k_1\exp(k_2 r) + k_3 \tag{2.93}$$

where $k_1 = 2.0\times10^7\ \text{g}\,\text{s}^{-2}\,\text{cm}^{-1}$, $k_2 = 22.53\ \text{cm}^{-1}$, and $k_3 = 8.65\times10^5\ \text{g}\,\text{s}^{-2}\,\text{cm}^{-1}$.An increase of the Young's modulus E in the term Eh/r_0 corresponds to a decreasing of the compliance or an increasing of the stiffness in the arteries.

- **Parameters for the small arteries**

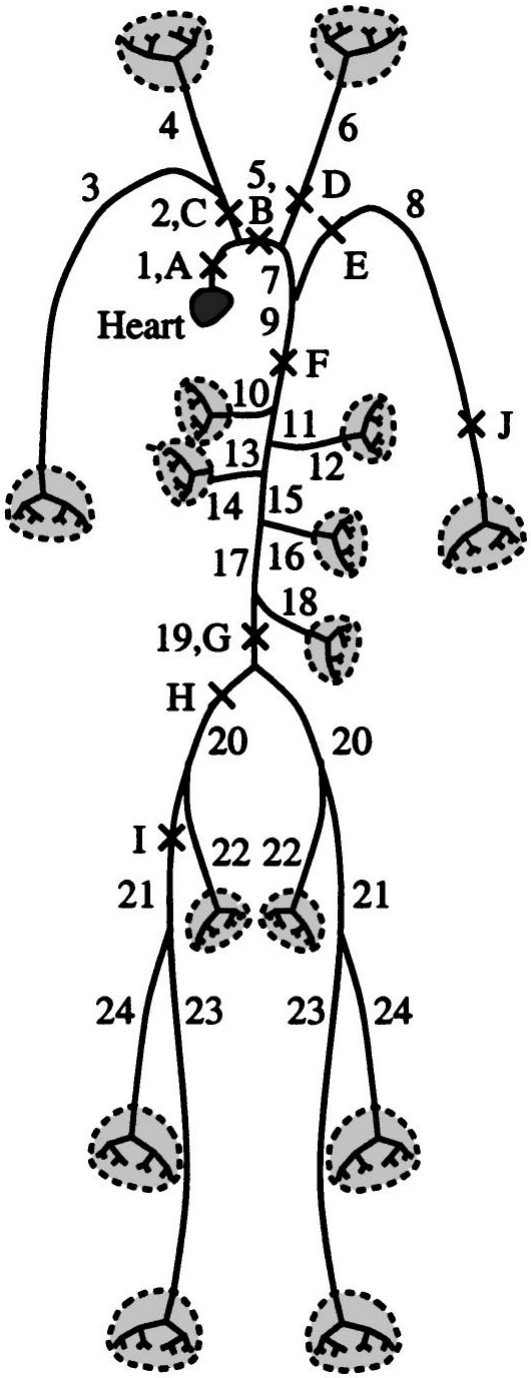

Figure 2.13: The large arteries in the systemic arteries model [91]. Detailed geometry information of each arteries is shown in Table 2.1.

In a cylindrical vessel, the relation determining the radius changes over an arterial bifurcation is given by Uylings [121],

$$r_p^{\xi} = r_{d_1}^{\xi} + r_{d_2}^{\xi}, \tag{2.94}$$

where $\xi = 3.0$ corresponds to laminar flow, and $\xi = 2.33$ corresponds to turbulent flow. The area ratio and asymmetry ratio are given by

$$\eta = (r_{d_1}^2 + r_{d_2}^2)/r_p^2, \quad \gamma = (r_{d_2}/r_{d_1})^2. \tag{2.95}$$

By using the relations in (2.94) and (2.95), the scaling parameters are determined as follows,

$$\alpha = (1 + \gamma^{\xi/2})^{-1/\xi}, \quad \beta = \alpha\sqrt{\gamma}. \tag{2.96}$$

In this model, the radius exponent and the asymmetry ratio are chosen as $\xi = 2.76$ and $\gamma = 0.41$, then values for other parameters are determined by (2.95) and (2.96), i.e. $\eta = 1.16$, $\alpha = 0.9$, $\beta = 0.6$.

The structured tree is terminated when the radius of the vessel r is smaller than a given minimum value $r_{min} = 10\mu$m. For the terminal vessel with the length L, the impedance is given and set to be zero, i.e. $Z_N(L,0) = 0$, where N is the number of the generation.

No.	Artery	L (cm)	r_{top} (cm)	r_{bot} (cm)	r_{min} (cm)
1	Ascending aorta	7.0	1.25	1.14	—
5	Aortic arch	1.8	1.14	1.11	—
7	Aortic arch	1.0	1.11	1.09	—
9	Thoracic aorta	18.8	1.09	0.85	—
11	Abdominal aorta	2.0	0.85	0.83	—
13	Abdominal aorta	2.0	0.83	0.80	—
15	Abdominal aorta	1.0	0.80	0.79	—
17	Abdominal aorta	6.0	0.79	0.73	—
19	Abdominal aorta	3.0	0.73	0.70	—
20	External iliac	6.5	0.45	0.43	—
21	Femoral	13.0	0.43	0.40	—
24	Femoral	44.0	0.40	0.30	0.01
22	Internal iliac	4.5	0.20	0.20	0.01
23	Deep femoral	11.0	0.20	0.20	0.01
2	Anonyma	3.5	0.70	0.70	—
3, 8	Subcl. and brach.	43.0	0.44	0.28	0.01
4	R. com. carotid	17.0	0.29	0.28	0.02
6	L. com. carotid	19.0	0.29	0.28	0.03
10	Celiac axis	3.0	0.33	0.30	0.02
12	Sup. mesenteric	5.0	0.33	0.33	0.02
14,16	Renal	3.0	0.28	0.25	0.02
18	Inf. mesenteric	4.0	0.20	0.18	0.01

Table 2.1: Geometrical data for the top, bottom radii and length for the large arteries.

Chapter 3

Coupling of the left ventricle (LV) and the systemic arteries (SA) models

The coupling between the LV and SA models is achieved by matching the pressure and flow rate at the interface plane between two models, i.e. the circulation model feeds back the pressure as a boundary condition to the LV model, and the flow rate from the LV is used as the input for the SA model (Fig. 3.1). The aortic valve is not modelled in the coupled model yet, so we model the function of the AV as follows: the AV opens when the pressure in the LV just exceeds the pressure in the proximal aorta adjacent to the valve; the AV closes when the flow rate is negative at the boundary plane in the LV proximal to the AV. To solve the governing equations of the system, which also incorporate the fluid-structure interaction and the active contraction of the myocardium, we use the IB/FE code [40] together with the Lax–Wendroff scheme of [91]. This is an explicit method and a sufficiently small time step Δt needs to be used to ensure numerical stability.

This chapter first describes the interface between three-dimensional LV and one-dimensional SA models, followed by the numerical methods used to solve the equations governing the fluid structure interactions at the interface. As this is a multiscale model, the time integration conditions are explained in detail. Finally, the numerical stability of the coupling is analysed.

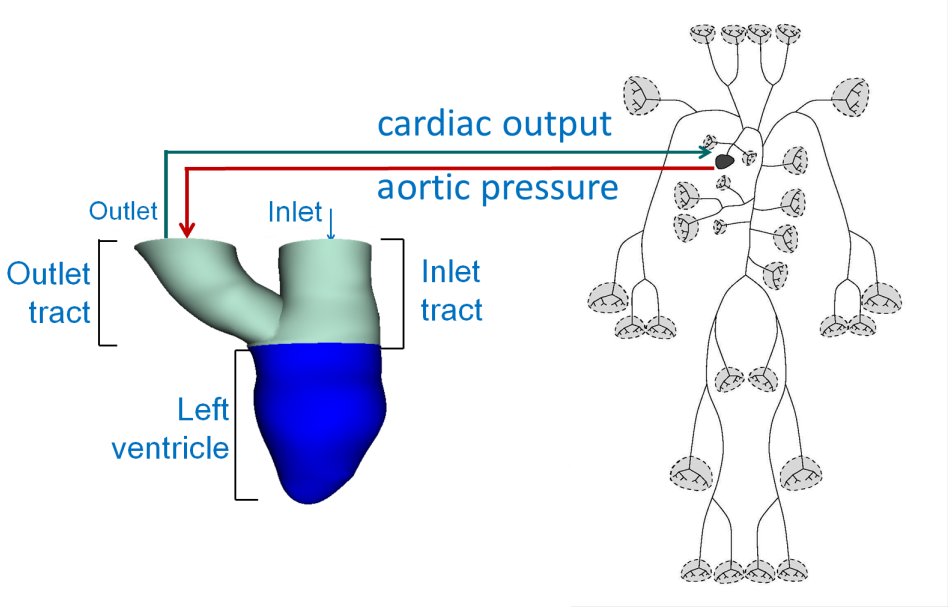

Figure 3.1: Coupling the 3-D LV model and the 1-D SA model.

3.1 Description of the interface between 3D and 1D domains

The key idea of the coupling is to simulate the wave propagation properly between the two models, which leads to a discussion of the treatments of the inflow boundary of the SA model and the outflow boundary in the LV model. To describe the coupling of the two models, we first consider two domains Ω_{3D} and Ω_{1D}, representing the outlet tract in the LV model and inlet of the ascending aorta in the SA model (Fig. 3.2), and the interface $\Gamma_a\,(x = a)$ is the upper boundary plane of outlet tract as well as the beginning of the ascending aorta.

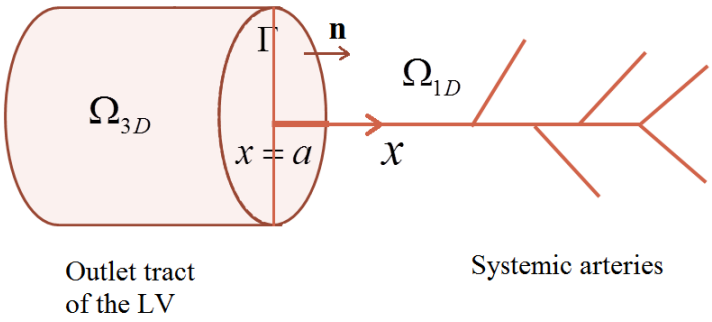

Figure 3.2: The interfacial plane $x = a$ at the location of the aortic valve (AV) connects the 3D model of the LV and the 1-D model of the aorta in the systemic arteries.

During systole, at the interface $\Gamma(x = a)$, the cross-sectional averaged flow rate and pressure are continuous across the interface, i.e.

$$\bar{p}_- = \bar{p}_+, \quad \text{where} \quad \bar{p}_- = \frac{1}{|\Gamma|}\int_\Gamma p \, \mathrm{d}A, \tag{3.1}$$

$$\bar{q}_- = \bar{q}_+, \quad \text{where} \quad \bar{q}_- = \int_\Gamma \mathbf{u}\cdot\mathbf{n} \, \mathrm{d}A. \tag{3.2}$$

in which $\mathbf{u}$ is the velocity of the fluid, $\bar{p}$ is the cross-sectional averaged pressure, $\bar{q}$ is the cross-sectional averaged flow rate, $\mathbf{n}$ is the outward unit normal to the surface Γ_a, and the subscript $-$ denotes variables from the 3D model, and $+$ denotes variables from the 1D model.

3.2 Coupling procedure during one cardiac cycle

3.2.1 Initialization of the coupled model

Normally, the SA model needs 4 to 6 periods before it gets into a steady phase, and it is too time consuming if we couple it with the 3D LV model directly and wait until the 7^{th} period to get the converged results. Thus, we run the circulation model for 6 periods as initialization for the coupled model, and during these periods, a converged cardiac output from the LV model with Windkessel boundary condition is used as inflow for the circulation model (Fig. 3.3), and the corresponding pressure in the ascending aorta during these period is shown in Fig. 3.4. After 6 periods initialization, the pressure in the circulation system has converged to a steady stage. The end-of-diastolic arterial pressure (P_{EDA}) at the end of the 6^{th} period is recorded and used to determine the opening time of the aortic valve by comparing it with the pressure in the LV proximal to the AV during isovolumetrc contraction.

3.2.2 Diastolic filling in the LV

A typical cardiac cycle in the coupled model starts from the beginning of the diastolic filling, when the aortic valve is fully closed. During diastolic filling, a zero-velocity condition is applied at the boundary of the aortic tract, and the mitral valve is opened to allow

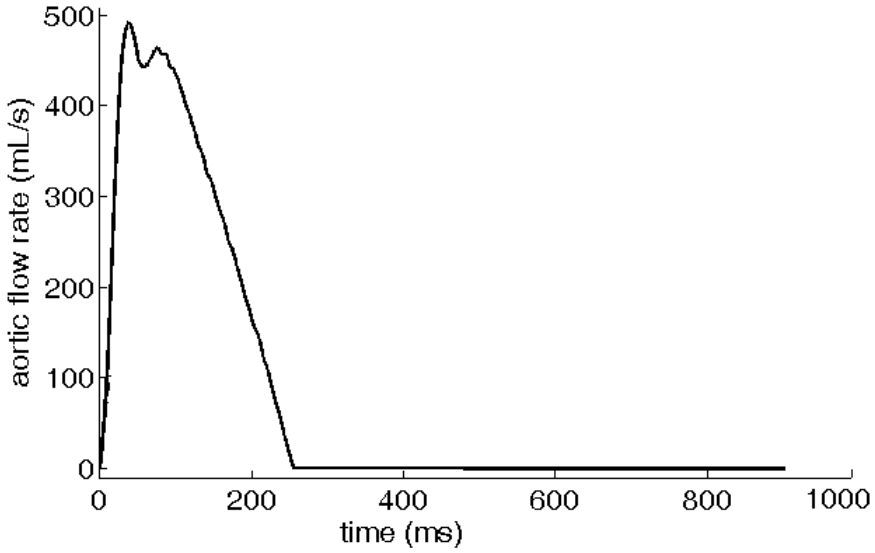

Figure 3.3: The cardiac output from the LV model with a windkessel boundary condition, used as inflow boundary condition for the SA model during initialization.

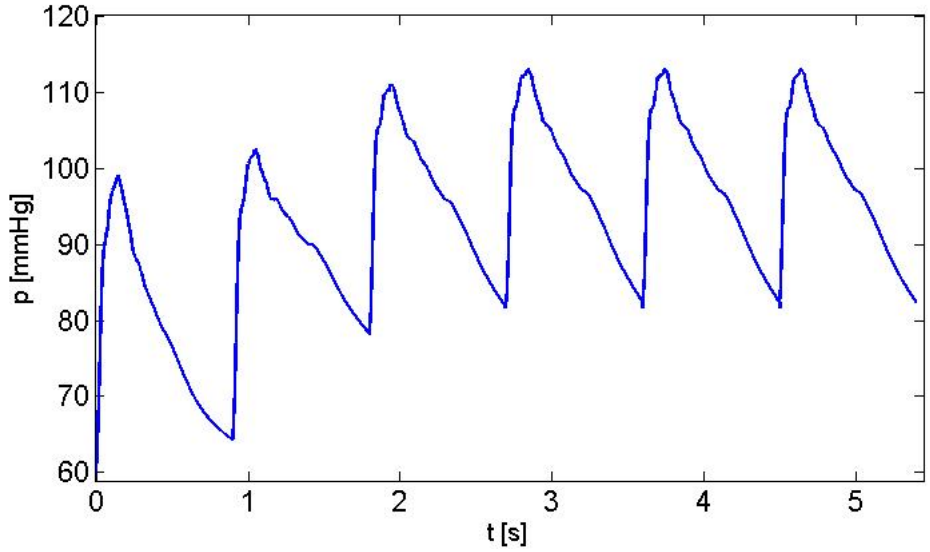

Figure 3.4: The pressure at the mid point of the ascending aorta during initialization.

flow into the LV, i.e. a free velocity boundary condition is applied at the boundary plane of the atrium tract, and a fixed end-of-diastolic pressure 8 mmHg is applied at the inner surface of the myocardium, which simulates the passive diastolic filling. Diastolic filling takes 0.8 s before the next stage, isovolumetric contraction, starts.

3.2.3 Isovolumetric contraction of the LV

From 0.8 s, LV isovolumetric contraction starts, and during this period, the cross-sectional averaged pressure $\bar{p}_- = \int_\Gamma p/|\Gamma| \mathrm{d}A$ in the aortic tract is compared at each time step with the pressure in the ascending aorta at the root of the systemic arteries. Once the pressure $\bar{p}_-$ first exceeds the pressure $\bar{p}_+$ ($\bar{p}_- > \bar{p}_+$), systole begins, and LV and systemic arteries are coupled. The pressure $\bar{p}_-$ increases every time step in the LV model, while the pressure $\bar{p}_+$ is a fixed pressure recorded from the end of the sixth initialization period. The duration of isovolumetric contraction is about $0.4 - 0.5$ s before systole starts.

3.2.4 The coupling during systole

During systole, the aortic valve is fully open and the LV model uses a pressure boundary condition, while the mitral valve is fully closed with a zero-velocity boundary condition. The cross-sectional averaged flow rate in the aortic tract at the interface plane $\bar{q}_-$ is tested at each time step; once it becomes negative ($\bar{q}_- < 0$), corresponding to a reversed flow, systole stops and so does the coupling. After the aortic valve is closed, there is no flow propagation or interaction between the LV and the systemic arteries, so that two models are disconnected thereafter. The duration of systole in the coupled model is about 0.25 s.

3.2.5 Relaxation in the LV and systemic diastole in the arteries

After the discoupling of two models, the LV model moves into the isovolumetric relaxation phase, during which time, a zero-velocity boundary condition is applied at boundary planes of both the aortic and the atrial tracts. Since the computational duration of the full cardiac cycle in the LV model is 2.0 s, the time for isovolumetric relaxation is about 0.85 s; it is longer than the physiological relaxation time to ensure the computational stability and to make sure the LV is fully relaxed and returns to the same early diastolic volume each cycle in order to start another period. At the same time, the SA model enters the systemic diastolic phase. The SA model has a physiologically realistic period of 0.9 s. After the systole, a zero flow rate boundary condition is applied as inflow to the SA model for the rest of the cardiac cycle.

3.2.6 Implementation of the boundary conditions

Inflow boundary condition for the SA model

When the two models are coupled, the flow rate at the outlet boundary of the aortic tract in the LV model is used as inflow for the SA model. From (2.53), in the SA model, the cross-sectional area A is determined by q at the boundary. For the Lax–Wendroff scheme at the inlet boundary, all variables marked with a cross are known (Fig. 3.5). In order to determine A_a^{n+1}, $q_{a+1/2}^{n+1/2}$ needs to be evaluated. At the $(n+1)^{\text{st}}$ time step, we introduce a ghost point $q_{a-1/2}^{n+1/2}$ marked with a circle in Fig. 3.5

$$q_a^{n+1/2} = \frac{1}{2}\left(q_{a-1/2}^{n+1/2} + q_{a+1/2}^{n+1/2}\right) \Leftrightarrow \tag{3.3}$$

$$q_{a-1/2}^{n+1/2} = 2q_a^{n+1/2} - q_{a+1/2}^{n+1/2}. \tag{3.4}$$

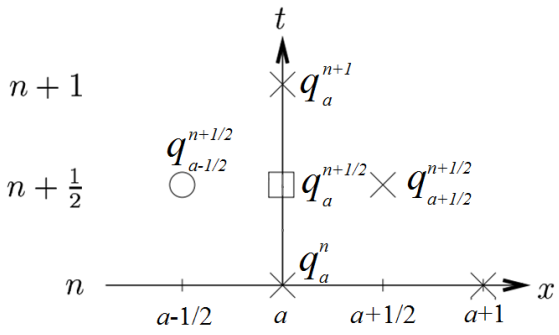

Figure 3.5: The Lax-Wendroff scheme at the inlet boundary in the SA model when the LV and the SA models are coupled. All known variables are marked with crosses; the ghost point is marked with a circle; the boundary condition is applied at the point marked with a square.

At the interface, $q_a^{n+1/2}$ (marked with a square in Fig. 3.5) is determined by using the corresponding flow rate from the LV model at $\bar{q}_-^{n+1}$ and $\bar{q}_-^n$ on the interface,

$$q_a^{n+1/2} = (\bar{q}_-^n + \bar{q}_-^{n+1})/2, \tag{3.5}$$

which are different from (2.60) used in Olufsen *et al*. (2012) [91]. Then A^{n+1} can be found from (2.53),

$$A_a^{n+1} = A_a^n - \frac{\Delta x}{\Delta t}\left(q_{a+1/2}^{n+1/2} + q_{a-1/2}^{n+1/2}\right). \tag{3.6}$$

The value of $\bar{p}_a^{n+1}$ is determined by equation stateequ, feeding back to the LV model as the inlet pressure boundary condition, $\bar{p}_-^{n+1} = \bar{p}_+^{n+1}$.

Outflow boundary condition for the LV model

Since the LV and the SA models are coupled during systole, the arterial model is used to provide the downstream boundary condition at the outlet boundary plane. As described previously, by assuming the pressure at the interface between two models are the same, i.e. $\bar{p}_- = \bar{p}_+$, we can calculate the cross-sectional area-averaged pressure in the aorta distal to the AV $\bar{p}_+$ at each time step and feeding back to the 3D outlet domain in the LV model, $\bar{p}_-^{n+1} = \bar{p}_+^{n+1}$. The systolic ejection phase ends when the LV is no longer to pump any blood through the aortic valve, i.e. backflow occurs at the interface in the LV proximal to the AV ($q_+ < 0\,\mathrm{mL\,s^{-1}}$), and the SA model is then detached from the LV model.

3.3 Time integration conditions

In the SA model, the evolution of the pressure pulse takes place in real time throughout the whole period in the systemic arteries. The length of time step Δt is fixed as $\Delta t_{\mathrm{SA}} = T/N = 0.9/8192 \approx 1.099 \times 10^{-4}$ s, in which T is the length of period and N is the number of time step during one period. In the LV model, as described in Section 2.1, the systole phase takes place in real time, but the diastolic filling and relaxation of the LV are not calculated in physiological time, rather they occur on a slower time scale to ensure numerical stability. The length of the basic time step in the LV model is $\Delta t_{\mathrm{LV}} = 1.221 \times 10^{-4}\,\mathrm{s}$, and during systole, it is decreased to $0.25\,\Delta t_{\mathrm{LV}} = 3.052 \times 10^{-5}\,\mathrm{s}$ in the early systole (approximately the first 100 ms), and $0.125\,\Delta t_{\mathrm{LV}} = 1.526 \times 10^{-5}\,\mathrm{s}$ in the rest of systole.

In effect, we run two clocks, one for each model. Physiological time is represented by the time t_{SA} in the systemic arteries model; and t_{LV} is the 'computational' time in the LV model. After initialization is complete, we set $t_{\mathrm{SA}} = 0$ when the aortic valve opens, and define time points in the SA model by

$$t_{\mathrm{SA}}^m = m\,\Delta t_{\mathrm{SA}}, \quad m = 0, 1, 2, \ldots, \tag{3.7}$$

where $t_{\mathrm{SA}}^0 = 0$, and the flow rate at the interface is $q_+^0 = 0\,\mathrm{mL\,s^{-1}}$. Time points in the LV model are denoted by

$$t_{\mathrm{LV}}^n = n\,\Delta t_{\mathrm{LV}}, \quad n = 0, 1, 2, \ldots, \tag{3.8}$$

where $t_{\mathrm{LV}}^{0} = 0$, and the flow rate is $q_{-}^{0} = 0\,\mathrm{mL\,s^{-1}}$ at the interface. The time integration during one cardiac cycle is shown in Fig. 3.6. Interpolation is used to couple events happening in the LV model at time t_{LV} with time t_{SA} in the SA model. A flow diagram for the implementation of the coupling is shown in Fig. 3.7.

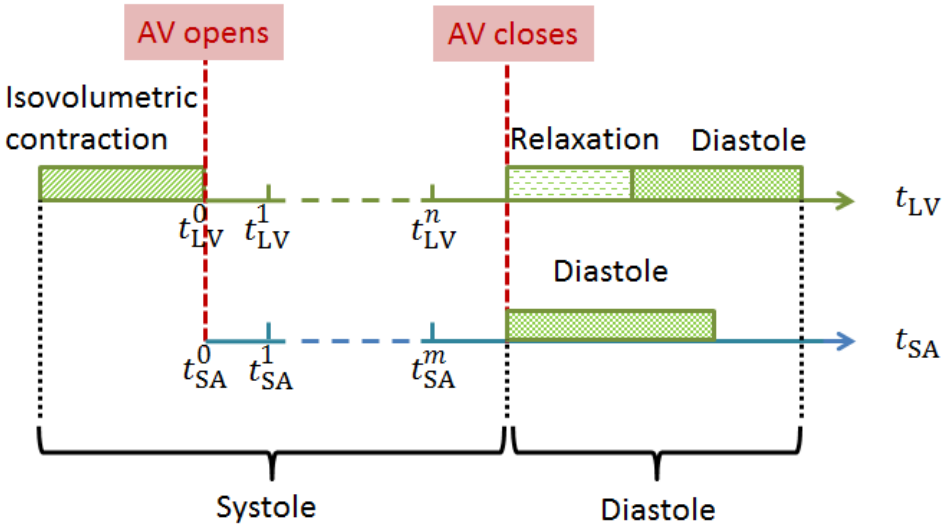

Figure 3.6: The time integration for the LV and SA models during one cardiac cycle. Physiological time is represented by the time t_{SA} in the systemic arteries model; and t_{LV} is the 'computational' time in the LV model.

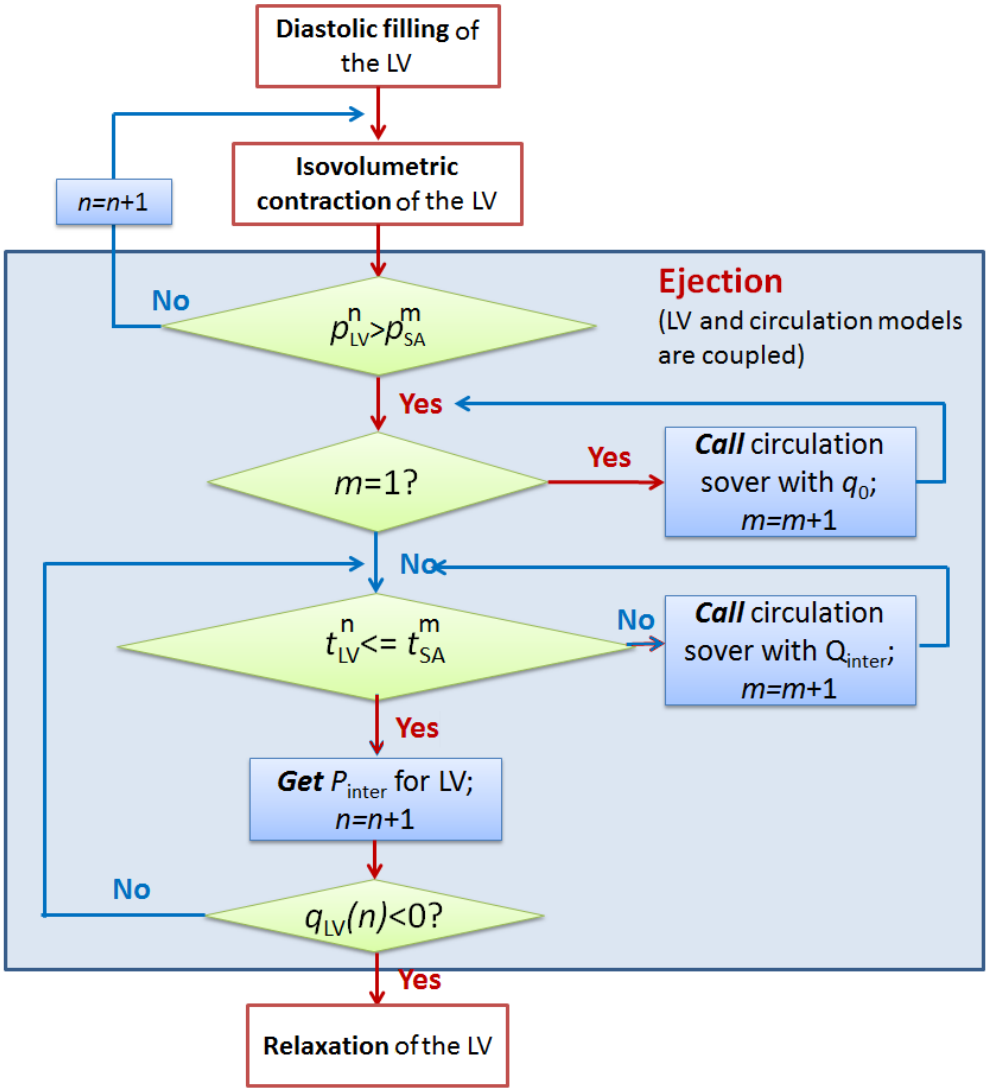

Figure 3.7: Flow diagram for the coupling the LV and the SA models during systole. p_{inter} and q_{inter} are the interpolated pressure and flow rate as given by equations (3.9) and (3.10)

The algorithm for interpolating p and q are as follows:

Algorithm 1: algorithm for interpolating p and q in the coupled model

if $AV_{open} = \texttt{True}$ & $AV_{close} = \texttt{False}$ **then**

if $m = 1$ **then**

Interpolation: $q_+^m = f_1(q_-^n, q_+^0, t_{\mathrm{LV}}^n, t_{\mathrm{SA}}^m, t_{\mathrm{LV}}^0, t_{\mathrm{SA}}^0)$**end**

$Solver_{\mathrm{SA}}(\mathrm{q}_+^m, q_+^{m-1}, p_+^m)$

$m = m + 1$

end

else

while $t_-^n \leqslant t_-^m$ **do**

Interpolation: $q_+^m = f_1(q_-^n, q_-^{n-1}, t_{\mathrm{LV}}^n, t_{\mathrm{SA}}^m, t_{\mathrm{LV}}^0, t_{\mathrm{SA}}^0)$

$\mathrm{Solver}_{\mathrm{circulation}}(\mathrm{q}_+^m, q_+^{m-1}, p_+^m)$

$m = m + 1$

end

if $t_-^n > t_+^m$ **then**

interpolation

end

: $p_-^n = f_2(p_+^m, p_+^{m-1}, t_{\mathrm{LV}}^n, t_{\mathrm{SA}}^m, t_{\mathrm{LV}}^0, t_{\mathrm{SA}}^0)$

end

if $q_-^n < 0$ **then**

$\mathrm{AV}_{\mathrm{close}} = \texttt{True}$

end

$n = n + 1$

where the interpolation equations f_1 and f_2 are given as follows:

$$f_1: \quad q_+^m = \frac{(q_-^n - q_-^{n-1}) * (t_{\mathrm{SA}}^m - t_{\mathrm{LV}}^n)}{t_{\mathrm{LV}}^n - t_{\mathrm{LV}}^{n-1}} + q_-^{n-1}, \tag{3.9}$$

$$f_2: \quad p_-^n = \frac{(p_+^m - p_+^{m-1}) * (t_-^n - t_+^{m-1})}{t_+^m - t_+^{m-1}} + p_+^{m-1}. \tag{3.10}$$

3.4 Parameters in the coupled model

In the coupled model, most parameters values are kept the same as those in the isolated LV and circulation model [35, 90], and only a few parameters are changed in order to make the coupling physiologically consistent.

Since the geometry of the LV and the systemic arteries are based on different healthy subjects, we use 1.25 cm as the radius at the beginning of the ascending aorta in the circulation model to match with the measurement radius $r_{\mathrm{aorta}} = 1.2505$ cm, from the MR images of the LV model [35].

Since no valve model is included in the coupled model, we assume that the aortic valve opens by a pressure difference between the interface of two models, and it closes when the reversed flow occurs in the aortic tract at the interface plane. This means we only model the fully opened and fully closed actions of the aortic valve, and neglecting the opening and closing processes. Another assumption is that the two models are coupled only during systole, and after systole, they are disconnected and allows to finish their own period. In Chapter 6, we will describe a more complex LV-AV-arterial model with a proper AV model coupled at the interface between the LV and the SA models, and discuss the differences and improvements.

The opening of the aortic valve is decided by the end-of-diastolic arterial pressure (P_{EDA}) in the coupled model, i.e. when the pressure in the LV proximal to the AV exceed the P_{EDA} in the circulation model, the aortic valve opens. Since the measured value of P_{EDA} from the healthy subject for modelling the LV is 85 mmHg, the SA model should provide a similar downstream in the LV model in order to provide physiologically comparable results. This has been done by setting the transmural pressure $p_0 = 60$ mmHg (in (2.43)) in the SA model giving $P_{\mathrm{EDA}} = 83$ mmHg. The transmural pressure p_0 in the SA model is constant that specifies the external pressure due to the tissues surrounding.

Chapter 4

Results of the standard case

In this chapter, the results of the pressure and flow waveforms of the coupled LV-SA model are presented in a standard case, which is defined by using measurements of two healthy subjects for modelling the LV and systemic arteries described in Gao et al. [35] and Olufsen et al. [90]. The results are compared with clinical measurements, and based on this standard case, some applications for simulating disease-related conditions will be presented in the next chapter.

4.1 Parameters in the Standard case

In the standard case, most parameter values are from measurements as in previous papers Hao *et al*. [35] and Olufsen *et al*. Olufsen et al. [90], and only a few is by chosen to provide reasonable results as described in Section 2.1.5 and Section 2.2.4.

The values of basic parameters in the coupled model are given in Table 4.1.

Name	Parameter	Value	Equation
Length of period (SA)	T_{SA} (s)	0.9	
Length of time step (SA)	Δt_{SA} (s)	1.099×10^{-4}	
Blood density	ρ ($\mathrm{g\,s^{-3}}$)	1.06	(2.33)
Inlet r of the ascending aorta	r_{aorta} (cm)	1.25	
Minimun radius of vessels	r_{min} (μm)	100	
Transmural pressure	p_0 (mmHg)	60	
Coefficient of Eh/r_0	k_1 ($\mathrm{g\,s^{-2}\,cm^{-1}}$)	2.00×10^7	(2.93)
Coefficient of Eh/r_0	k_2 ($\mathrm{cm^{-1}}$)	-22.53	(2.93)
Coefficient of Eh/r_0	k_3 ($\mathrm{g\,s^{-2}\,cm^{-1}}$)	4.65×10^6	(2.93)
Radius exponent	ξ	2.76	(2.94)
Asymmetry ratio	γ	0.41	(2.95)
Length of period (LV)	T_{LV} (s)	2.0	
Basic length of time step (LV)	Δt_{LV} (s)	1.22×10^{-4}	
End-of-diastolic pressure	P_{ED} (mmHg)	8	
Scale factor of active tension	T_{scale}	4	(2.18)
Coefficient of W	a (kPa)	0.19	(2.14)
Coefficient of W	b	5.08	(2.14)
Coefficient of W	a_{f} (kPa)	1.2	(2.14)
Coefficient of W	b_{f}	4.15	(2.14)
Coefficient of W	a_{fs} (kPa)	0.24	(2.14)
Coefficient of W	b_{fs}	1.3	(2.14)

Table 4.1: Choice of parameter values for the standard case.

4.2 Results in the standard case

After the first initial period in the coupled LV-SA model, the results are converged to a steady stage, so we are analyzing the results from the second period and afterward from the coupled model to study the interactions between the LV and the arterial system. The averaged computational time is 168 hours per one coupled period with 7 parallel CPUs.

4.2.1 Pressure and flow rate in the LV

Figures. 4.1 (a) and (b) show the deformed LV endocardial surface (coloured by red) at the end of diastole and the end of systole, superimposed with corresponding long axis cine MR images. The deformed LV geometry agrees well with the cine images.

Figure 4.2 shows the LV pressure-volume loop in one cardiac cycle along with the velocity field in the longitudinal section in different phases during the second coupled period. Figure 4.2 (a) shows the initial LV deformation at $t = 0.0$ s. During diastole, the LV volume increases from 70 mL to 143 mL (Fig. 4.2 (c)) in 800 ms, and a clear filling vortex in the LV can be seen in the mid-diastole (Fig. 4.2 (b)). During the isovolumetric contraction, the myocaridum starts to actively contract with both the MV and the AV closed (Fig. 4.2 (d)). When the pressure inside LV cavity is higher than the pressure in the aorta (83 mmHg), the AV opens and the systolic ejection begins. The velocity fields at the early-systole, mid-systole and late-systole are shown in Fig. 4.2 (e)–(g), and with the increasing of the LV pressure, the maximum velocity of the ejection domain increases in the middle systole, and then decreases with the decreasing of the LV pressure. The systolic ejection continues until the AV closes when the flow rate in the LV proximal to the AV is zero. The stroke volume in systole is around 74.7 mL, corresponding to an ejection fraction (EF) of 53%, a 4% difference compared with the MR image measured EF (57%). After systole, the myocaridum relaxes with both the MV and the AV closed to get back to a fully relaxed phase at the end of this cardiac cycle (Fig. 4.2 (h)).

Figure 4.3 compares the simulated aortic volumetric flow rate to the MR image measurements. The peak aortic flow rate from the coupled model is around 494 $\mathrm{mL\,s^{-1}}$, which shows less than 1% difference compared with the MR image measured value of 500 $\mathrm{mL\,s^{-1}}$. However the peak value arrives earlier in the coupled model compared to the in-vivo measurements, which is partially caused by the lack of an aortic valve in our model. Since a zero velocity boundary condition is applied on the boundary planes of the aortic and atrium trunks after systole, the flow rate from the coupled model stays zero when the AV is closed. The total ejection period is 260 ms, 40 ms less than the MR image measurements, shown in Fig. 4.3.

Figure 4.4 shows the detailed LV dynamics during systole including the prescribed intra-

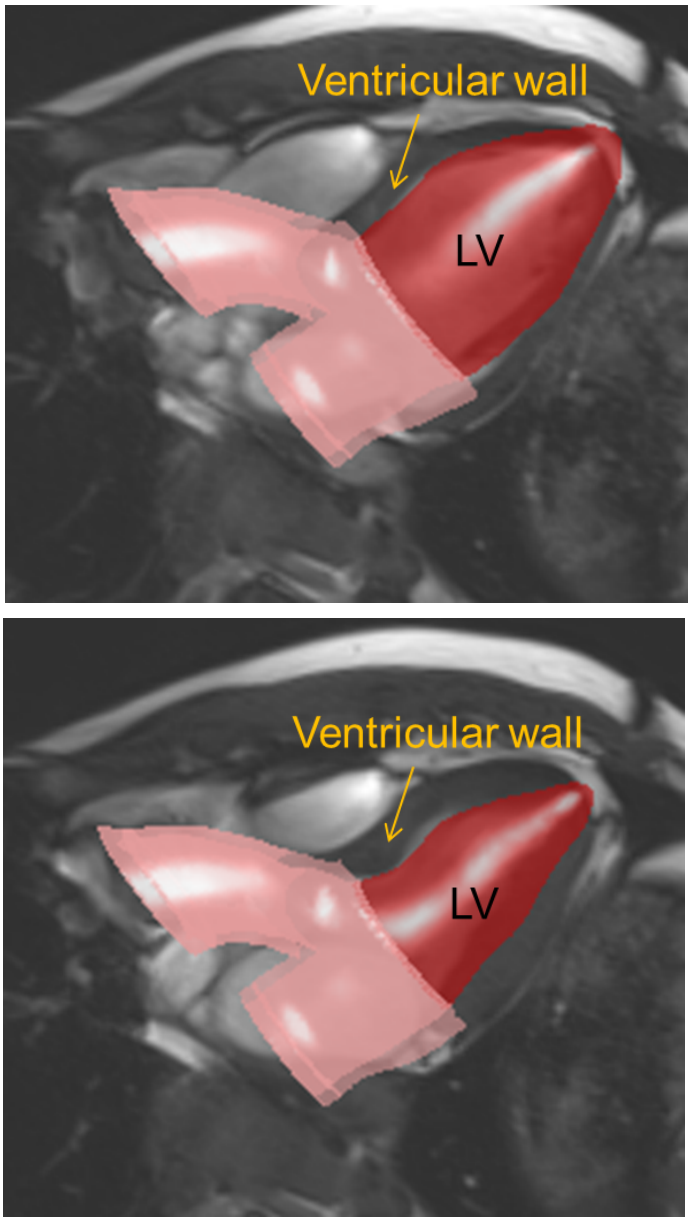

Figure 4.1: The deformed LV geometry at end of diastole (a) and end of systole (b) superimposed with cine MR images.

cellular calcium transient, aortic flow rate, average active tension, and LV cavity pressure and volume, normalized with corresponding peak values. At the beginning of systole (0 – 50 ms), the intracellular calcium transient increases quickly, the generated active tension follows the calcium transient but slightly delayed, and the LV pressure nearly follows the active tension generation, while the LV pressure is not high enough to open the AV. After isovolumetric contraction, the AV opens. Even though the calcium transient begins to decrease, the generated active tension increases slowly and maintained at a relatively

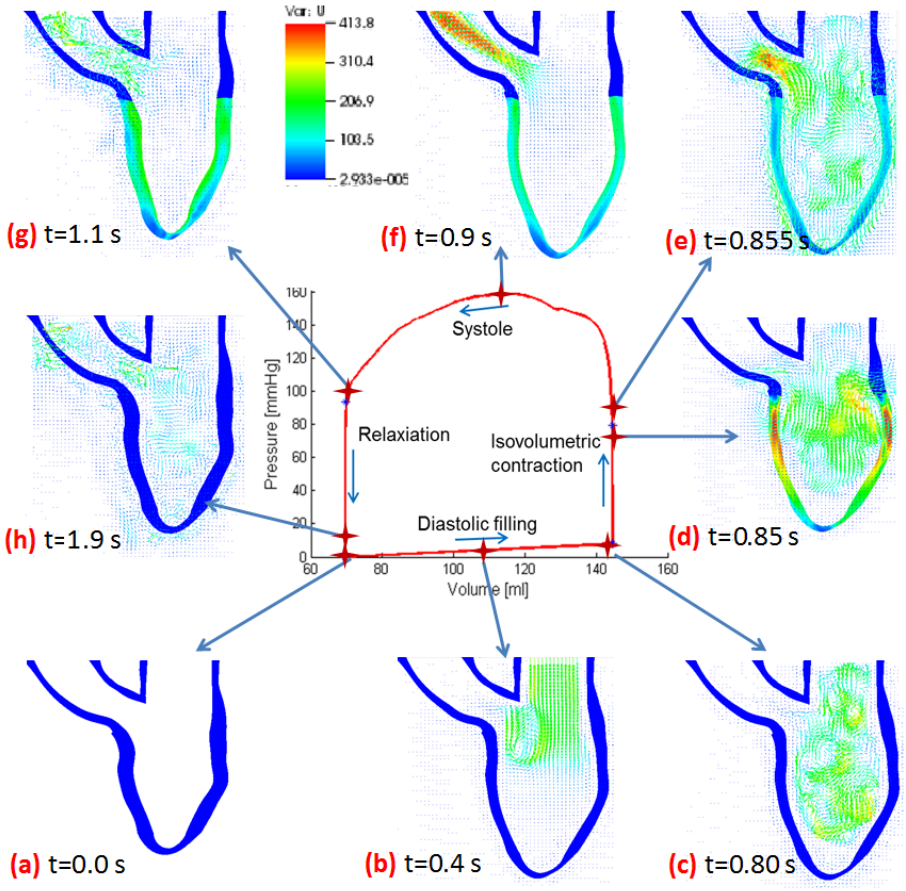

Figure 4.2: The pressure-volume loop (center) and velocity field in the LV with the active tension of the myocardium at different phases during the second caridac cycle in the coupled model, i.e. from the initial stage at $t = 0.0$ s (a), mid-diastole at $t = 0.4$ s (b) and the end-of-diastole at $t = 0.8$ s (c), end of isovolumetric contraction at $t = 0.85$ s (d), early systole at $t = 0.855$ s (e), middle systole at $t = 0.9$ s (f), end of systole at $t = 1.1$ s (g), and the end of relaxation at $t = 1.9$ s (h).

high level, because the tension depends not only on the intracellular calcium transient, but also on myocardial stretch and its rates. The peak active tension is about 74 ms later than the intracellular calcium transient peak. The LV pressure follows the same trend as the active tension. The aortic flow rate increases quickly after the AV opens, and reaches the peak. The first peak of the flow rate arrives 43 ms earlier than the peak LV pressure and the active tension, but 32 ms later than the intracellular calcium transient.

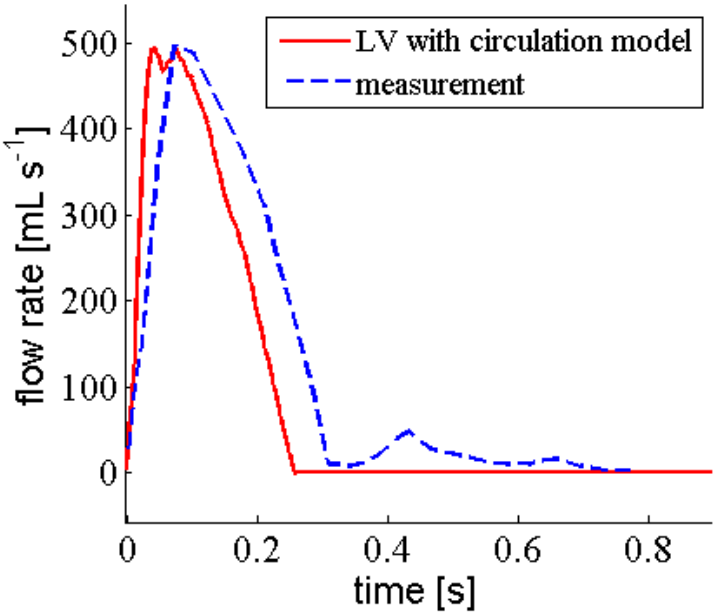

Figure 4.3: The aortic flow rate from the coupled model (solid) compared with in vivo MRI measurements (dashed).

4.2.2 Pressure and flow rate in the systemic arteries

In order to have a closer look at the pressure and flow waveforms in the arteries and provide more informative picture of the systemic circulation, we analyze the pressures and the flow rates in the 24 large arteries and they are observed divided naturally into three groups (Fig. 4.5), i.e. aorta, coeliac arteries, and other long arteries.

The first group consist of the segments of the aorta, i.e. the beginning of the ascending aorta to the aortic arch, the thoracic aorta and down to the end of the abdominal aorta.

Figure 4.6 shows the pressure and flow waveforms through the aorta. The wave forms are plotted at the midpoint in each artery during one cardiac cycle. Comparing the pressure waves at different positions in the aorta in Fig. 4.6 (a), it shows that the peak pressure increases form the proximal aorta to the distal arteries and a clear trend of time delay when the peak pressure arrives in the distal arteries during systole. The increasing of the peak pressure is due to the tapering effect of the vessels. At the beginning of diastole (around 0.25 s), there shows a pronounced dicrotic notch in the ascending aorta, and the notch tends to fade away in the distal arteries (Fig. 4.6 (a)). This notch relates to the reflected

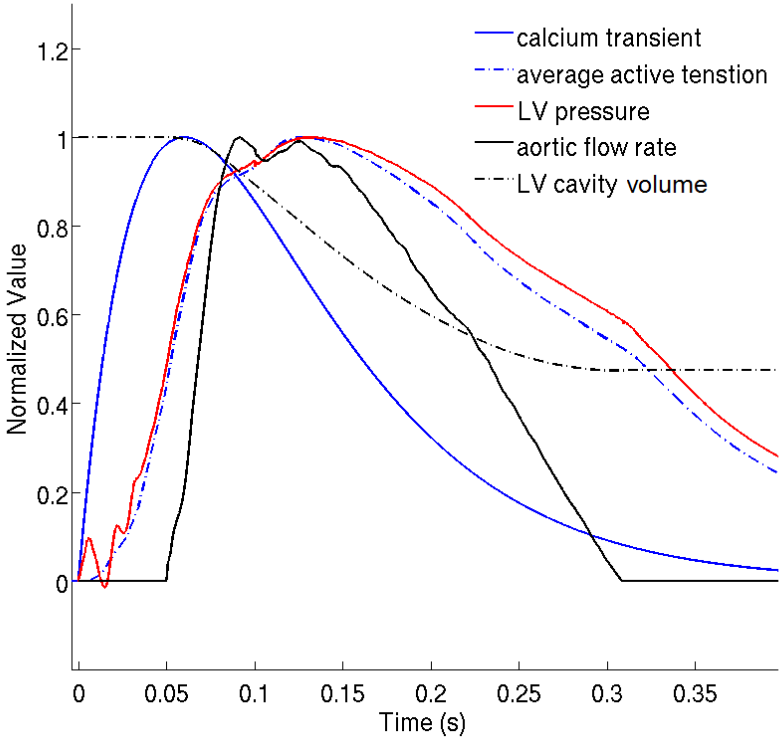

(a)

Figure 4.4: Normalized calcium transient (peak: $10^{-7}\,\mu$ mol), average active tension (peak: 101.5 kPa), LV pressure (peak: 159 mmHg), aortic flow rate (peak: 495 mL s^{-1}) and LV cavity volume (peak: 143 mL), 0 s is the beginning of isovolumetric contraction (end of diastole). Data are only from the systolic phase and normalized with peak values.

flow at the end of systole (Fig. 4.6 (b)). Figure 4.6 (b) compares the flow rate along the aorta. It shows that the peak flow rate decreases from the proximal artery to the distal artery, since the cross-sectional area of the proximal artery is larger, thus more volume flux can be maintained in it than that received in the distal artery. Similarly, there shows a clear trend of time delay of the peak wave in the distal arteries. Table 4.2 summarizes the peak pressure (P^*), peak flow rate (Q^*), and the arriving time of peak values T_P^* and T_Q^* in these arteries are listed in Table 4.2.

The second group are the coeliac arteries separating from the segments of the aorta. The pressure and flow rate profiles at the midpoints of these arteries are shown in Fig. 4.7. The pressure profiles of these arteries are quite similar to each other, since they are side branches from aorta and their inlet locations are within 10 cm in distance, thus the pressure drop is small among these arteries.The flow rates in these coeliac arteries is much lower

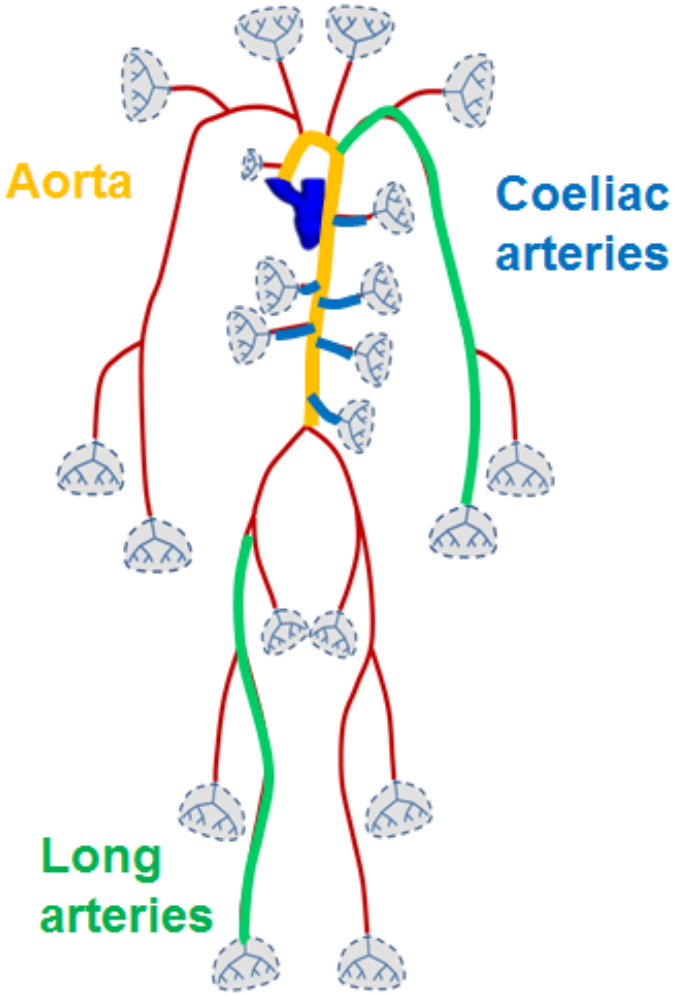

Figure 4.5: Three groups of large arteries, i.e. aorta (yellow), coeliac arteries (blue), and long arteries (green).

than those in the segments of aorta, ranging from $1\,\mathrm{mL\,s^{-1}}$ to $36.5\,\mathrm{mL\,s^{-1}}$ (Fig. 4.7 (b)), since the inlet diameter of these arteries is much smaller (around $1/3$) than that in the segments of the aorta at the bifurcation. The wave profiles become flatter and show a lower peak from the superior mesenterior artery to the celiac axis artery, the renal artery and the inferior mesenteric artery, which follows the order of the inlet diameter. In other words, the coeliac artery with larger inlet cross sectional area contains more flux and shows a higher peak value than the small coeliac arteries.

The third group are long segments of arteries, such as carotid (19 cm), brancial (43 cm)

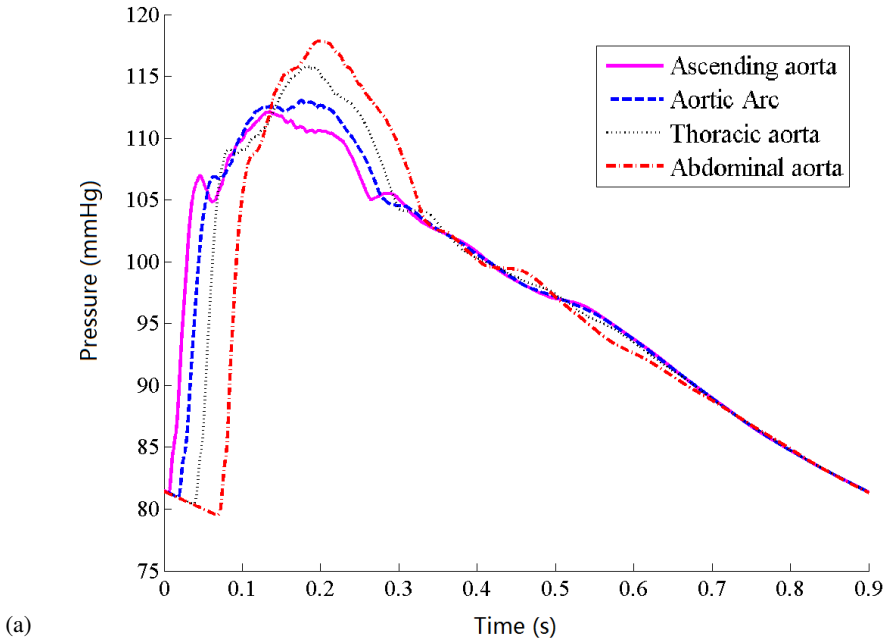

(a)

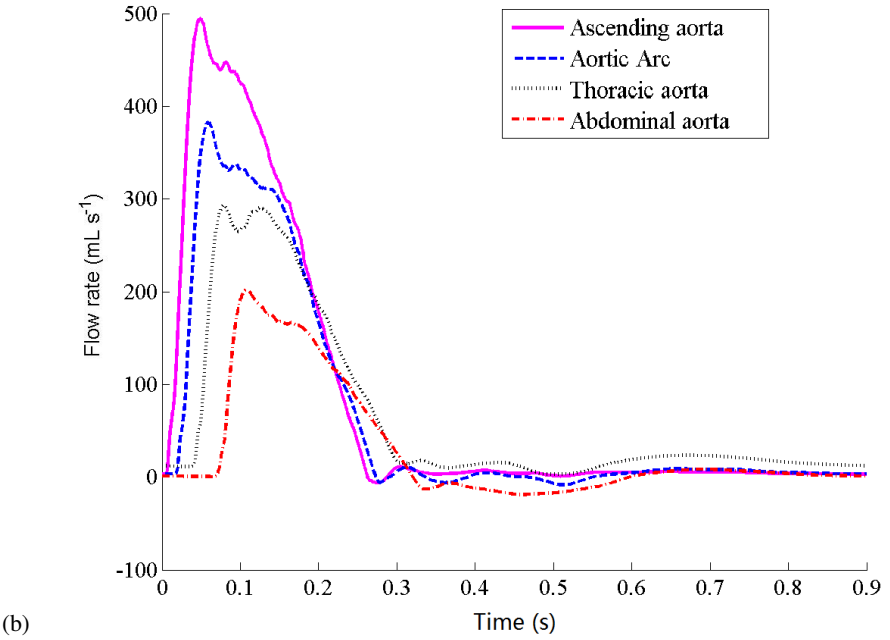

(b)

Figure 4.6: The pressure (a) and the flow rate (b) at the midpoints in the ascending aorta, aortic arc, thoracic aorta and abdonimal aorta in one period.

and femoral arteries (44 cm). Both the pressure and flow rate drops a lot along these arteries. Fig. 4.8 (a) shows that the more distal artery has a longer delay of the peak pressure. The pressure drops are 11 mmHg, 8 mmHg and 5 mmHg in the carotid, brachial and the femoral arteries. The peak flow rate decreases more than 50% along these arteries,

	P^* (mmHg)	Q^* (mL s^{-1})	T_P^* (ms)	T_Q^* (ms)
Ascending aorta	112.1	494.5	135.2	49.2
Aortic arc	113.0	382.8	175.5	58.5
Thoracic aorta	115.7	293.3	194.3	79.0
Abdonimal aorta	117.8	202.3	205.6	107.4

Table 4.2: Summary of the pressure, flow rate and arriving time of peak values in the ascending aorta, aortic arc, thoracic aorta and abdonimal aorta during one cardiac cycle

and a large amount of back flow shows up at the end of the brachial and femoral arteries. As the pulse propagates along the arteries, we see the peak occurs later in the more distal vessels. Compared with the time when the peak pressures arrive in these arteries, the peak flow rates arrive 61 ms, 73 ms and 128 ms earlier in the carotid, brachial and the femoral arteries.

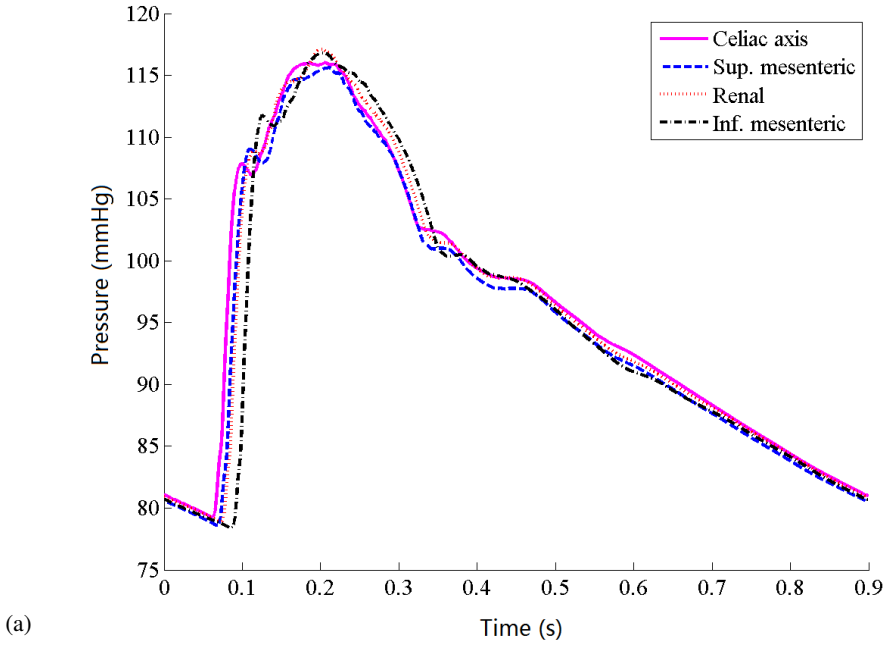

(a)

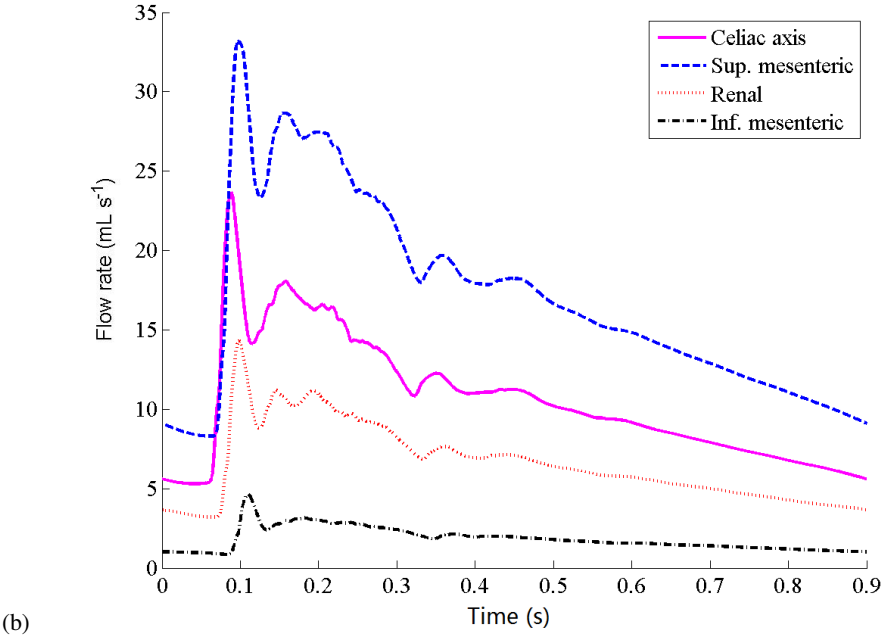

(b)

Figure 4.7: The pressure (a) and the flow rate (b) at the midpoints in the coeliac arteries, i.e. the celiac axis, superior mesenteric, renal and inferior mesenteric arteries in one period.

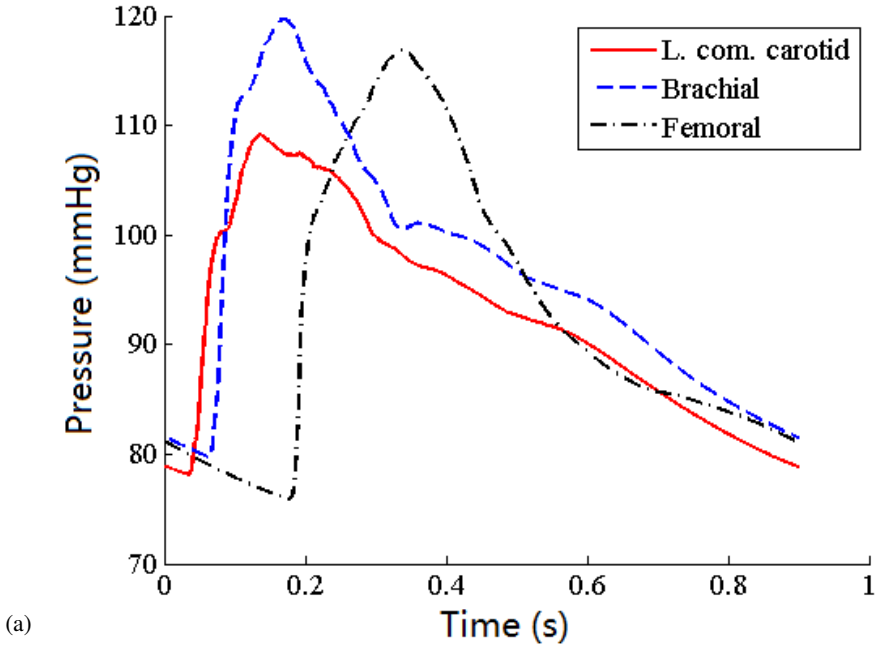

(a)

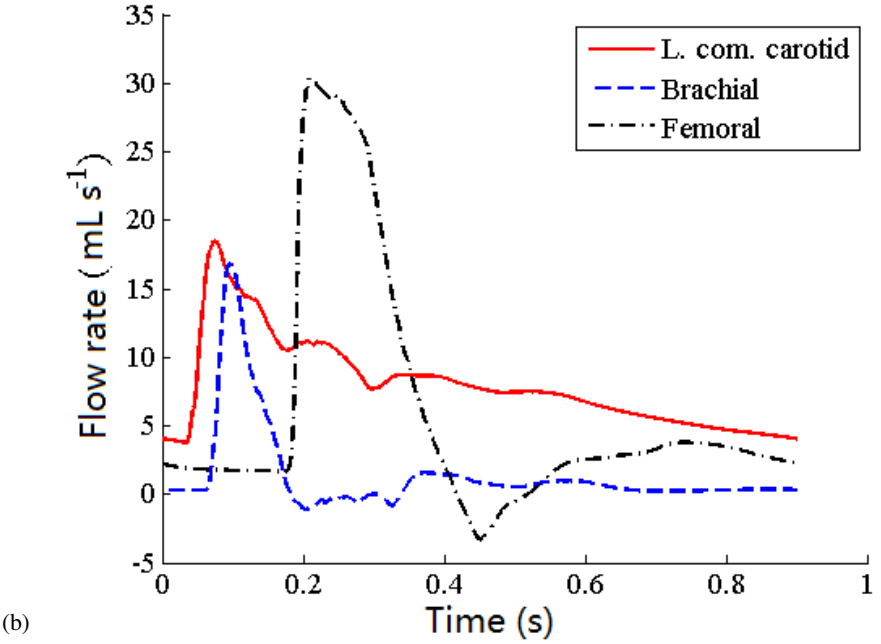

(b)

Figure 4.8: The pressure (a) and the flow rate (b) at the midpoints in the long arteries, i.e. left common carotid, brachial and femoral arteries in one period.

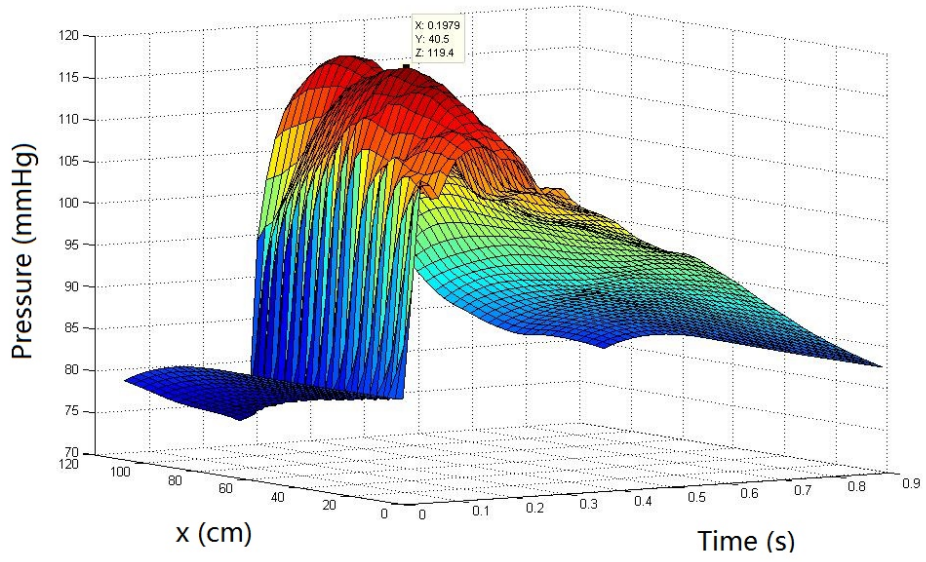

(a)

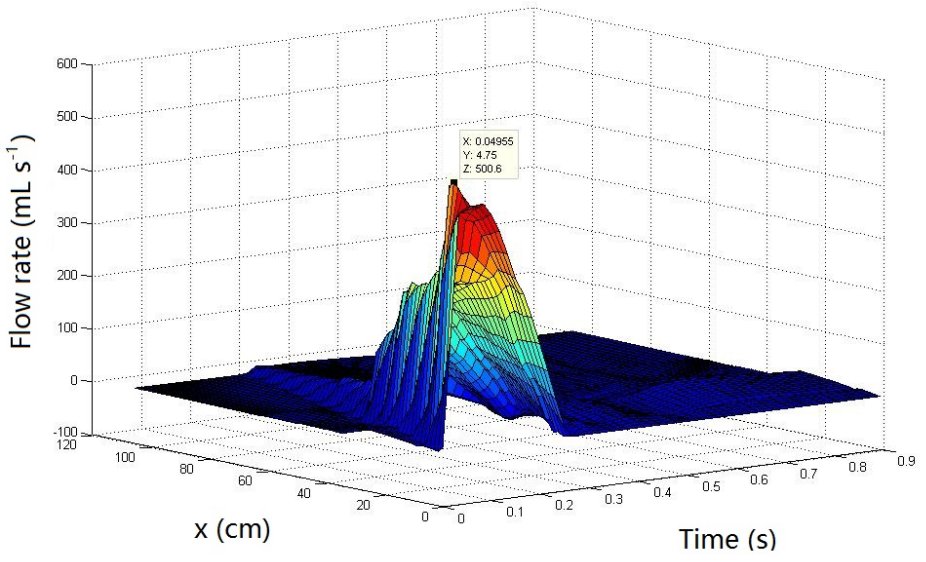

(b)

Figure 4.9: The pressure (a) and flow rate (b) from the beginning of the ascending aorta to the end of the femoral artery (artery numbers: 1, 5, 7, 9, 11, 13, 15, 17, 19, 20, 21,and 24 in Fig. 2.13) as functions of x and t during one cardiac cycle. Peak pressure is 119.4 mmHg, and peak flow rate is 500.6 mL s^{-1}.

4.3 Discussion

In this chapter, we have presented computational results of the coupled model in a normal case, and make comparisons with the published experiment data [35], specifically the LV pressure, the cardiac output profile, the stroke volume and the ejection fraction.

The peak flow rate arrives earlier in the coupled LV-SA model compared to the in-vivo measurements, which is due to the absence of the aortic valve. We will discuss it in Chapter 6 when a simple lumped-parameter aortic valve model is coupled in the LV-SA system.

The ejected blood volume during systole is 73 mL, corresponding to an ejection fraction of 53%, a 4% difference compared with the measured EF (57%), and it is within the range of EF values for a healthy subject Mahadevan et al. [72]. We can see that the LV dynamics are well described and simulated in the coupled model. The systolic and diastolic pressure in the brachial artery are 120 mmHg and 79 mmHg, which are within the range of the general physiological data, in which the systolic and diastolic pressure are 124.1 ± 11.1 mmHg, and 77.1 ± 7.1 mmHg [107]. The pressure and flow rate from the proximal aorta to the distal artery capture the basic characteristics of wave propagation in the systemic arteries [93].

The peak LV pressure (159.1 mmHg) is close to the experiment data (150 mmHg) with less than 3% difference [35]. However, compared with the peak pressure in the aorta distal to the AV (112.1 mmHg), there shows a 47 mmHg pressure drop. The high pressure drop is due to the geometry of the outlet tract, which is artificially designed based on the MR images at early systole. The diameter is measured as 1.8 cm at that time, and during systole, the diameter of the valvular region is expanding to 2.5 cm in mid-systole, but this expanding procedure has not been fully modelled in the LV model, while we keep the outlet tract rigid in order to apply boundary conditions easily. The effects of changing the diameter of valvular region will be discussed in Chapter 7. A more complete expanding action of the valvular region or a more patient-specific model can be developed in future study to provide more comparable results with the measurements.

Chapter 5

Simulating disease-related cases

Changing the preload and afterload lead to changes in the LV function [57]. The preload is the initial stretching of the cardiac myocytes prior to contraction, and there are several factors that determine the ventricle preload, such as venous blood pressure, ventricular compliance, heart beat rate, outflow resistance, inflow resistance, etc [57]. The afterload is the ”load” against which the heart must contract to eject blood, and a major component of the ventricular afterload is the aortic pressure [57]. In order to study how the preload and afterload affect the ventricular-arterial system, we apply this LV-SA model to simulate four pathological conditions, i.e. stiffening of the arterial wall, functional rarefaction, shortening of the diastolic phase (as an early exploration of increasing the heart beat rate), and changes in the end-of-diastolic pressure, representing different preload and afterload conditions. We show results of the pressure and flow rate waveforms in the LV and the SA compared with the results from the standard case. The comparisons give a general idea of how pathology affect the preload and afterload, and thus affecting functions of the ventricular-arterial system.

5.1 Description of pathological conditions

Case 1. Stiffening the arterial wall of systemic arteries

There are clinical observations of age-associated changes in arterial wall structure and functions, and the most consistent and well-reported changes are wall thickening and a

reduction of elastic properties (stiffening) in the large arteries [64]. There are plenty of clinical measurements that relate to the stiffness of the arteries [6, 64, 126], and a basic one is measuring the pulse wave velocity (PWV) along the vessel, which is related to the average stiffness of the arterial wall [3]. In biomechanics, the Moens–Korteweg equation describes the relationships between PWV and the incremental elastic modulus E_{int} of the arterial wall as follows

$$PWV = \sqrt{\frac{E_{\text{int}}h}{2r\rho}}, \tag{5.1}$$

where h is the wall thickness, r is the vessel radius, and ρ is the blood density. Avolio et al. [6] shows measurements of PWV for 480 subjects between ages 3 and 89 years, and giving a linear trend of averaged aortic PWV over age

$$\text{PWV} = 9.2\,\text{AGE} + 615. \tag{5.2}$$

From this equation, the PWV increases approximately by 23% and by 46% in subjects from age 20 to 40 and 60, corresponding to around 50% and 100% increase of the elastic terms $E_{\text{int}}h/2r\rho$ in (5.2). As described in Section 2.2, by increasing the value of Eh/r_0 in (2.93) in our model, see Fig.5.1, we can model the stiffening of the vessels. The increasing stiffness of the arterial wall (or the decrease of the arterial compliance) relates to increasing of the LV afterload. Two examples, increasing the stiffness of arterial walls by 50% and 100% for the large and small arteries are studied in this case.

Case 2. Functional rarefaction

Since vessels of diameters between 100 μm and 300 μm have a significant impact on the pressure and flow rate in the large arteries, it is important to study and to understand the effects of vascular beds [38, 82]. Vascular rarefaction is a vascular disease caused by a reduction in the density of small arterioles associated with essential systemic hypertension [49]. Since the systemic hypertension increases the LV afterload, this is another case to study the effects of LV afterload in the ventricular-arterial system. In this study, the vascular rarefaction is simulated by changing parameters to reduce the amount of vessels in the vascular beds, while keeping the minimum radius of the small vessels $r_{min} = 100$ μm fixed. In (2.94) and (2.95), it shows that only any decreasing of either ξ or γ leads to a decrease in η, which alters the total number of vessels in a structured tree. Thus, the vascular bed becomes rarefied (i.e. the total number, and thus density, of vessels is

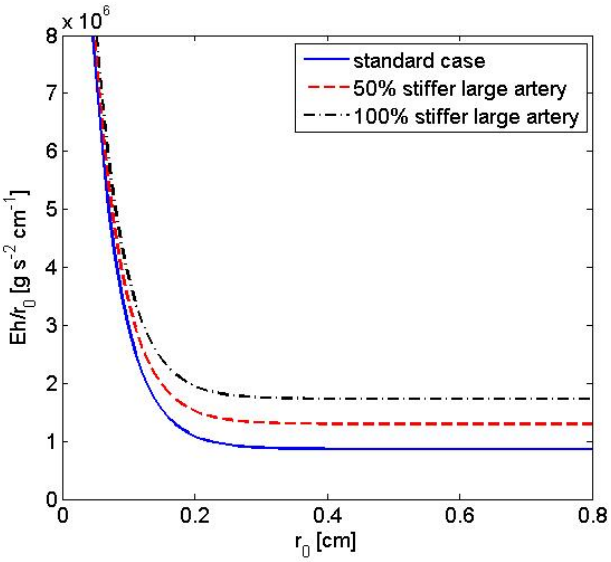

Figure 5.1: Increasing Eh/r_0 to simulate an increase of the arterial wall stiffness, where k_3 in (2.93) is increased by 50% (dash) and 100% (dash-dot) respectively.

reduced). In this model, $\xi = 2.76$ and $\gamma = 0.4048$, represent normal values for a healthy subject. The severity of vascular rarefaction is simulated by decreasing the radius exponent ξ to 2.6 (decreasing by 6%) and 2.4 (decreasing by 13%), respectively. The effects of changing the radius exponent on the total number of vessels are shown in Table 5.1.

ξ	α	β	Number of vessels	change (%)
2.4	0.8858	0.5672	1.04×10^4	-70.95
2.5	0.8941	0.5725	1.43×10^4	-59.93
2.6	0.9017	0.5774	1.96×10^4	-45.34
2.76	**0.9113**	**0.5835**	$\mathbf{3.57\times10^4}$	**0**
2.9	0.921	0.5897	6.40×10^4	78.82
3	0.9265	0.5932	9.73×10^4	171.98

Table 5.1: The effects of changing radius exponent ξ in (2.94) on the vascular density in the vascular beds and scaling factors α and β. The changing of total number of vessels is for the vascular beds connected to one of the terminal arteries, the celiac axis artery.

Case 3. Shortening the systemic diastolic phase

Heart beat rate is a reliable reflection of the many physiological factors, and it can be affected by a variety of impacts, such as aging [106] and exercise [54]. In order to study

how the heart beat rate affects the ejection phase in the LV and systemic arteries, we artificially shorten the duration arterial diastolic phase as an early exploration of increasing the heart beat. Basically, by shortening the systemic diastolic phase, the end-of-diastolic arterial pressure P_{EDA} in the ascending aorta will be raised. This results in a higher opening pressure at the beginning of systole in the coupled model. The effects of shortening the diastolic phase is simulated by shortening the length of period in the systemic circulation model from 0.9 s to 0.8 s, 0.75 s, 0.6 s and 0.5 s, corresponding to an increase of heart beat rate from 67 b/min to 75 b/min, 100 b/min, and 120 b/min.

Case 4. Changing the end-of-diastolic pressure

The end-of-diastolic pressure is an important factor in the Frank–Starling study of the cardiac funtion [57], and it is also important for calculating the preload in the LV based on the Laplace law,

$$\text{Preload (wall stress)} = \frac{P_{\text{ED-LV}} \cdot R_{\text{ED-LV}}}{2h}, \tag{5.3}$$

where $P_{\text{ED-LV}}$ is the end-of-diastolic pressure, $R_{\text{ED-LV}}$ is the left ventricular end-of-diastolic radius, and h is the thickness of the ventricular wall. Increasing the $P_{\text{ED-LV}}$ leads to an increase in LV preload. A population-based $P_{\text{ED-LV}} = 8$ mmHg is chosen in the standard case, but it can vary when the heart disease occurs [78]. By varying the value of $P_{\text{ED-LV}}$ in the LV-SA model, we study how the LV preload affects the LV and systemic arterial mechanics. The effects of preload is simulated by decreasing the $P_{\text{ED-LV}}$ to 6 mmHg and increasing it to 10 mmHg respectively.

5.2 Results of changing stiffness of systemic arteries in the coupled model

Figure 5.2 shows the changes in average active tension, LV pressure and the aortic flow rates during systole when varying the stiffnesses of the large or small arteries. Stiffness changes in the small arteries have no effect on the LV functions compared to the standard case. As the stiffness of the large arteries increases, the average active tension increases slightly mainly at late systole with little effect in the early systole as in Fig. 5.2(a). Similar trends can be found for the LV pressure in Fig. 5.2(b). Table 5.2 summarizes the end-of-diastolic arterial pressure (P_{EDA}), peak aortic pressure (P_a^*), peak LV pressure (P_{LV}^*), peak

aortic flow rate (Q_a^*), the stroke volume (V_s) and the ejection period (T_{ej}) during systole. It shows that the aortic flow rate with the stiffest large arteries is slightly less than the standard case, with a difference of 2.6% for the peak value, and 6% in the stroke volume per beat. The LV functions are mainly affected the stiffness in the large arteries in the coupled model, with increased arterial stiffness from 50% to 100%, the P_{EDA} decreases from 10% to 19%, the peak LV pressure increases from 1.5% to 3.5%, the peak aortic pressure decreases from 1.4% to 2.7% with decreased cardiac output per beat from 1.9% to 6%. Over long time, these changes for homeostasis may promote heart remodelling to compensate for the decrease in stroke volume per beat.

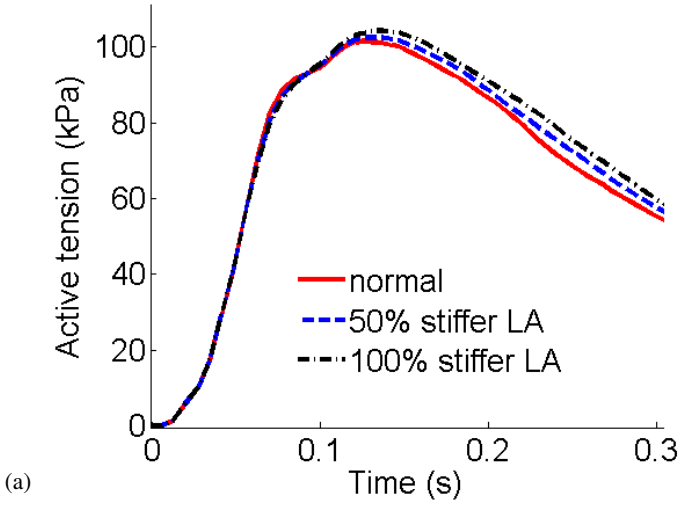

(a)

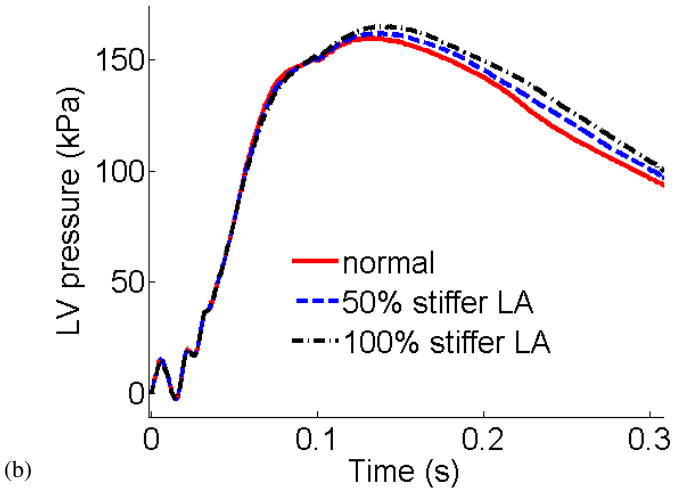

(b)

Figure 5.2: Averaged active tension (a) and the LV pressure (b) in systole for stiffer large arteries

The effects of stiffening of the walls of the large arteries on the pressure profiles are

	P_{EDA} (mmHg)	P_{a}^{*} (mmHg)	P_{LV}^{*} (mmHg)	Q_{a}^{*} ($\mathrm{mL\,s^{-1}}$)	V_{s} (mL)	T_{ej} (ms)
standard case	81.31	110.3	159.23	494.53	74.68	259.3
50% stiffer LA	74.68	123.73	161.72	487.45	72.27	257.6
100% stiffer LA	69.55	133.78	164.89	481.02	70.24	257.8
50% stiffer SA	83.3667	112.7	159.8	493.8	74.404	258.3
100% stiffer SA	81.4475	110.2	159.0	493.1	74.869	258.6

Table 5.2: Effects of variation of arterial stiffness on systolic LV function

the same in three groups of large arteries, but the effects of flow rate are different between these groups, i.e. aorta, coeliac arteries, and long arteries. The pressure profiles in the large arteries show an increase of the peak values and decrease of trough values (Fig. 5.3 (a), (c) and (e)). At the midpoint of the ascending aorta, the peak systolic pressure is increased by 3.8% and 8.0% and at the midpoint of the femoral artery it increases by 7.5% and 16.8% when stiffening the large arteries by 50% and 100%, compared with standard case (Fig. 5.3 (a), (e)). The peak flow rate decreases in the aorta and long arteries with an earlier arrival of the backflow (Fig. 5.3 (d), (f)), but the peak flow rate increases in the coeliac arteries with a more pronounced second peak and lower trough flow rate (Fig. 5.3 (d)). Fig. 5.3 (f) shows an earlier arrival of peak flow rate compared to the standard case, which are 37.2 ms (50% stiffer large arteries) and 54.4 ms (100% stiffer large arteries) at the midpoint of the femoral artery. Increasing the stiffness of the arterial walls in small arteries has less effect on both pressure and flow rate in the arteries than increasing the arterial stiffness of the large arteries.

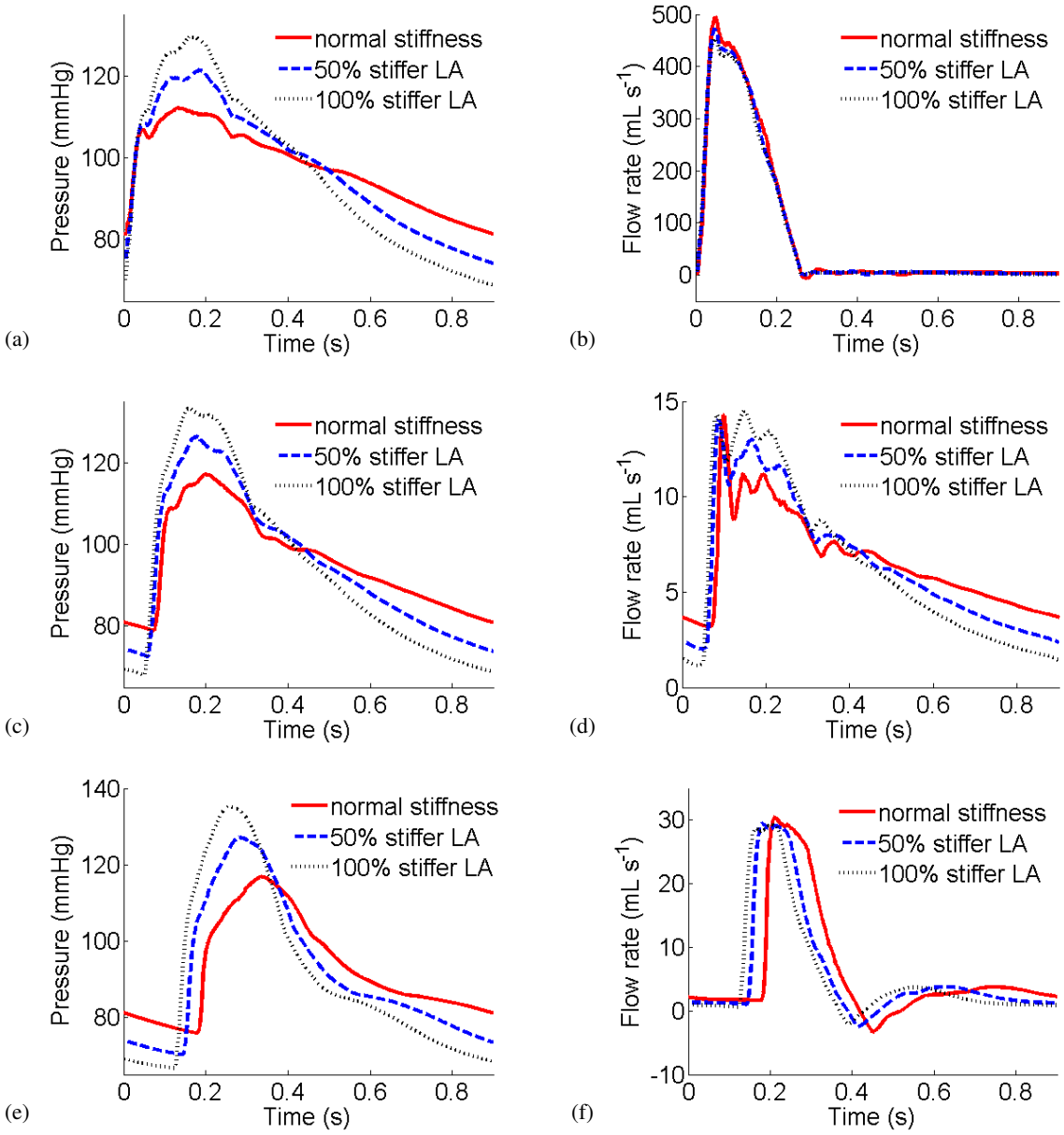

Figure 5.3: Comparisons of the pressure (left) and flow rate (right) in the ascending aorta ((a), (b)), the renal artery ((c), (d)) and the femoral artery ((e), (f)) when stiffening the arterial wall of large arteries by 50% (first row) and 100% (second row).

5.3 Results of functional rarefaction

Figure 5.4 shows the change of systolic LV dynamics with the severity of rarefaction in the circulation model. With increased severity, the generated active tension increases in order to pump sufficient blood to the remote vascular bed, as shown in Fig. 5.4 (a). The peak active tension is increased from 101.5 kPa to 102.8 kPa and 105.2 kPa with the increasing

severity of rarefaction. It also suggests the averaged power of the LV increases when there is a rarefaction in the vascular bed. The systolic LV pressure also increases with increased rarefaction (Fig. 5.4 (b)), for the most severe case ($\xi = 2.4$), the LV peak pressure is 8 mmHg (7.1 %) higher than the standard case. Because the LV is working harder to pump enough blood in systole, differences for the aortic flow rates across AV are less than 0.5% of the standard case (Table 5.3). In general, with increased severity of rarefaction, the aortic flow rates decrease slightly with shorter systolic ejection periods. For the most severe case ($\xi = 2.4$), the stroke volume per beat is 4.2% less than the standard case, which could trigger the heart remodelling in order to maintain the same cardiac output over long times. Table 5.3 summarizes the end-of-diastolic arterial pressure (P_{EDA}), peak aortic pressure (P_a^*), peak LV pressure (P_{LV}^*), peak aortic flow rate (Q_{a}^*), the stroke volume (V_{s}) and the ejection period (T_{ej}) during systole with different severity of rarefaction.

	P_{EDA} (mmHg)	P_{a}^* (mmHg)	P_{LV}^* (mmHg)	Q_{a}^* ($\mathrm{mL\,s^{-1}}$)	V_{s} (mL)	T_{ej} (ms)
$\xi = 2.4$	93.17	120.47	165.44	498.52	71.56	249.8
$\xi = 2.6$	84.40	114.32	161.16	495.40	73.72	255.1
$\xi = \mathbf{2.76}$ **(standard)**	81.31	112.12	159.23	494.53	74.68	259.3

Table 5.3: Summary of rarefaction's effect on systolic LV function

The effects of the functional rarefaction on the pressure are the same for the three groups of the large arteries, which shows an increase of both the peak and the trough pressure (Fig. 5.5 (a), (c) and (e)). In the ascending aorta, the peak pressure increases 4.4 mmHg and 11.2 mmHg (Fig. 5.5 (a)), and it increases 6.1 mmHg and 15 mmHg in the femoral artery compared with standard case with the increasing severity of rarefaction ($\xi = 2.76$ (standard) to $\xi = 2.6, 2.4$) (Fig. 5.5 (e)). The trough pressure increases 6.4 mmHg and 16.8 mmHg in the ascending aorta, and it increases 1 mmHg and 11.1 mmHg in the femoral artery with the increasing severity of rarefaction. Due to the shortening and tapering of the small arteries at each end of the terminal large arteries, the flow rate caused by the functional rarefaction shows a slightly higher peak and an increased reflected wave in the large arteries (Fig. 5.5 (b), (d) and (f)). The peak flow rate increases by less than 0.5% in the ascending aorta, but it increases by 3.9% and 8.9% with more pronounced back flow in the femoral artery compared with standard case with the increasing severity of rarefac-

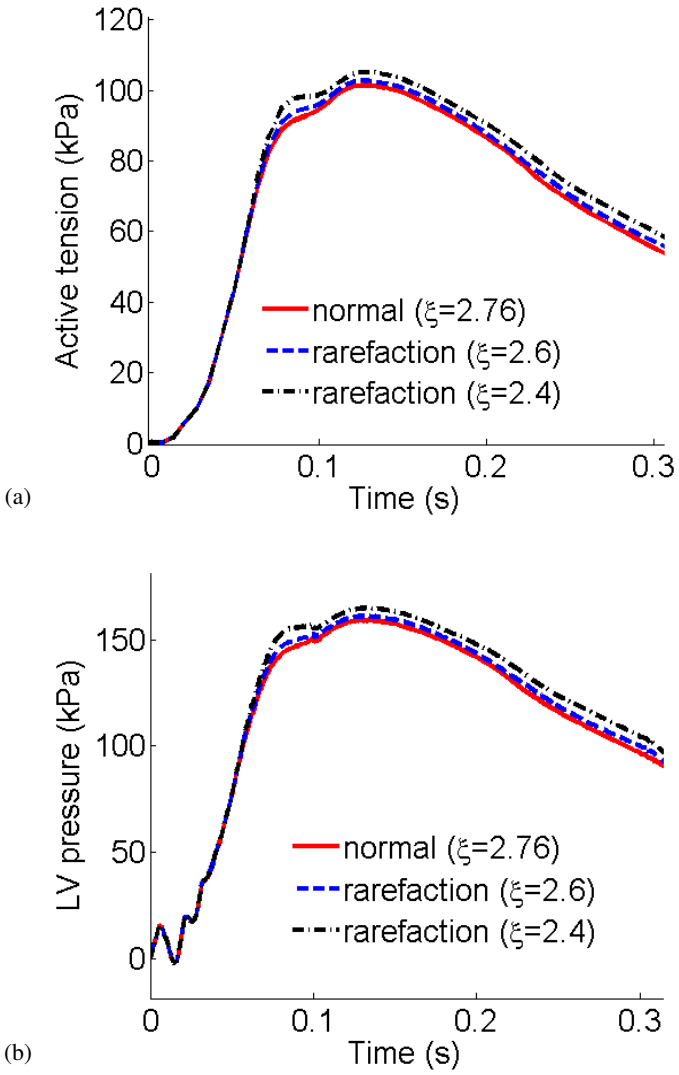

Figure 5.4: Averaged active tension (a) and the LV pressure (b) in systole for different severity of rarefaction.

tion. In the coeliac arteries group, the peak flow rates remains the same, but after the first peak, the flow rate decreases faster and stays at a lower value when rarefaction occurs, as shown in Fig. 5.5 (d).

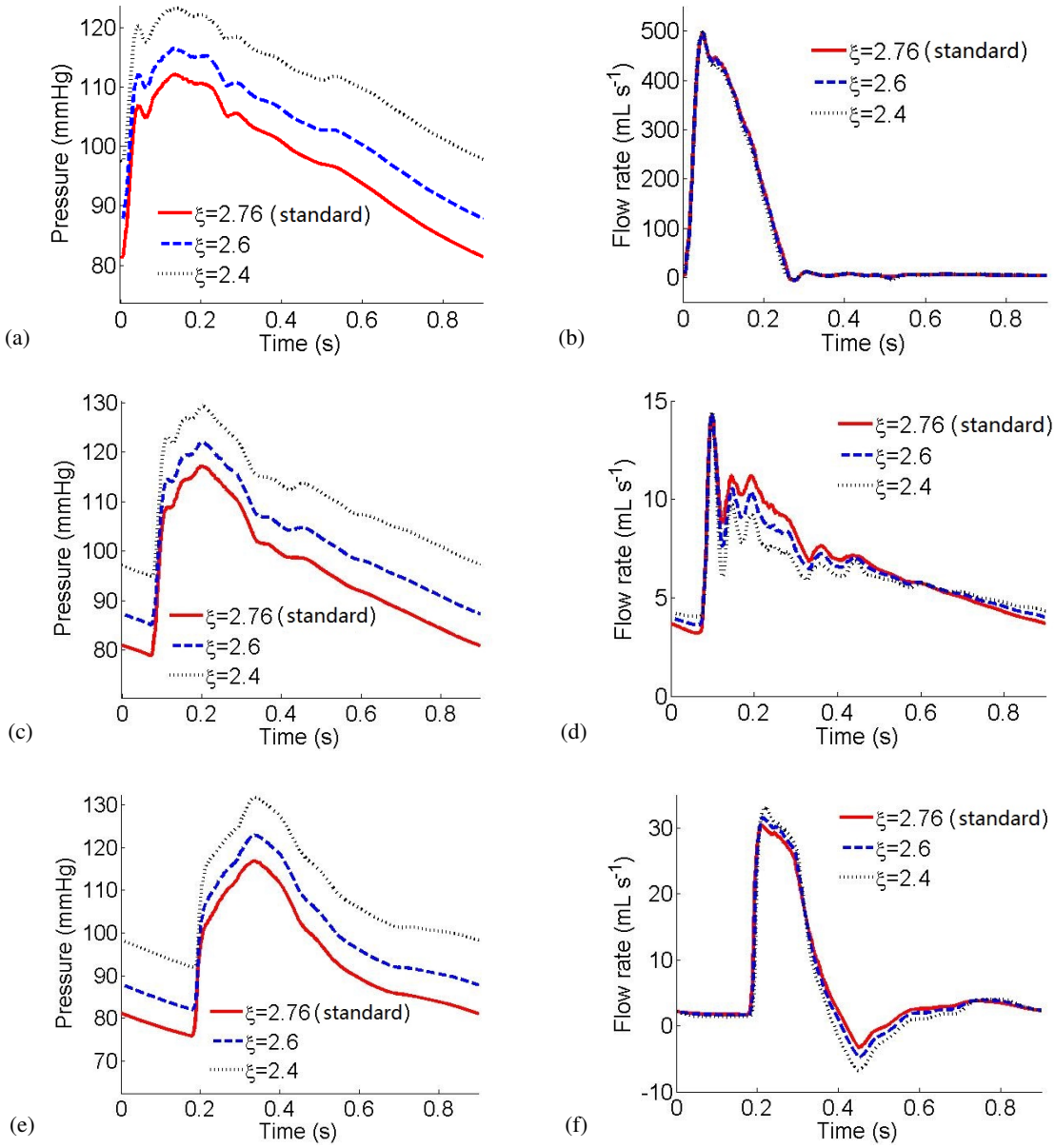

Figure 5.5: Comparisons of the pressure (left) and flow rate (right) in the ascending aorta ((a), (b)), the renal artery ((c), (d)) and the femoral artery ((e), (f)) with different severities of functional rarefaction (severe rarefaction from $\xi = 2.6$ to $\xi = 2.4$).

5.4 Results of shortening the diastolic phase in the coupled model

When we shorten the diastolic phase, the length of period is shortened (from 0.9 s (standard) to 0.75 s, 0.6 s and 0.5 s), and the active tension increases correspondingly. The increased active tension can be explained by the increased end-of-diastolic arterial pressure (P_{EDA}) (from 81 mmHg (standard), to 89 mmHg, 100 mmHg, and 106 mmHg for

	P_{EDA} (mmHg)	P^*_{a} (mmHg)	P^*_{LV} (mmHg)	Q^*_{a} ($\mathrm{mL\,s^{-1}}$)	V_{s} (mL)	T_{ej} (ms)
$\mathbf{T_{period} = 0.9\,s}$ **(standard)**	81.31	112.12	159.23	494.53	74.68	259.3
$T_{\mathrm{period}} = 0.75\,\mathrm{s}$	88.87	116.59	162.05	498.05	73.50	255.8
$T_{\mathrm{period}} = 0.6\,\mathrm{s}$	100.25	123.22	166.79	503.24	71.63	250.9
$T_{\mathrm{period}} = 0.5\,\mathrm{s}$	106.10	129.7	170.0	500.60	69.87	248.2

Table 5.4: Summary of the effect of shortening the diastolic phase on systolic LV function

T= 0.9, 0.75 0.6 and 0.5 s) provided by the systemic circulation model. Higher P_{EDA} requires slightly longer isovolumetric contraction to generate a high enough LV pressure. The isovolumetric contraction duration is 58 ms for T= 0.5 s, 55 ms for T= 0.6 s, 52 ms for T= 0.75 s and 50 ms for the standard case. Similarly, the LV pressure also is higher with shorter systemic diastolic phase due to the enhanced active tension. Because of the delayed opening of the AV, the cardiac output per beat is slightly less than the standard case with shorter systemic diastolic phase. In the coupled model with T= 0.5 s, even thought the stroke volume per beat is 6.5% less than the standard case, the cardiac output per minute is nearly 1.7 times. Table 5.4 summarizes the end-of-diastolic arterial pressure (P_{EDA}), peak aortic pressure (P^*_a), peak LV pressure (P^*_{LV}), peak aortic flow rate (Q^*_{a}), the stroke volume (V_{s}) and the ejection period (T_{ej}) during systole by shortening the systemic diastolic phase.

Since the systemic diastolic phase is shortened, the P_{EDA} is raised. The pressure in three groups of large arteries shows the same trend with a much higher peak and higher trough pressure (Fig. 5.7 (a), (c) and (e)). In the ascending aorta, the peak pressure increases 4.4 mmHg, 11.1 mmHg and 16.6 mmHg and the trough pressure increases 7.8 mmHg, 20.1 mmHg and 26.5 mmHg when the length of period is shortened from 0.9 s to 0.75 s, 0.6 s and 0.5 s (Fig. 5.7 (a)). In contract, the differences of peak and trough pressures are smaller in the renal and femoral arteries (Fig. 5.7 (c), (e)). In Figs. 5.7 (b) and (f), the flow rate in the ascending aorta does not change much, but it decreases 3.4%, 13.1% and 14.9% in the femoral artery when T= 0.75 s, 0.6 s and 0.5 s compared with standard case. While the flow rate increased dramatically in the coeliac arteries (Fig. 5.7 (d)), especially the trough flow rate, which are increased by 18.9%, 67.6% and 94.6% in the renal artery when T= 0.9 s is shortened to T= 0.75, 0.6, 0.5 (s).

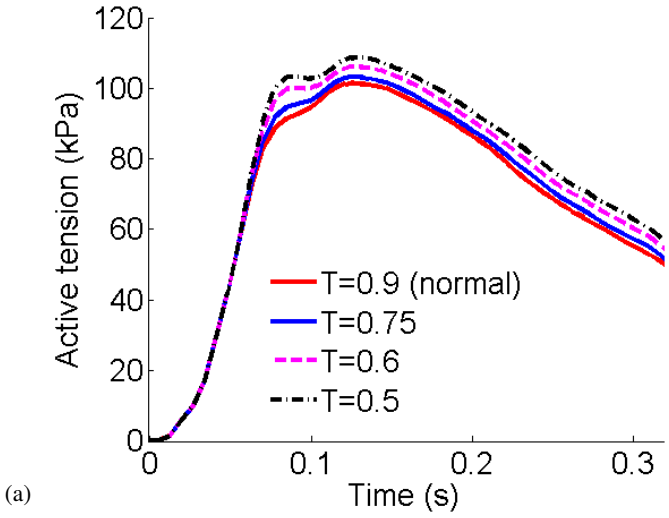

(a)

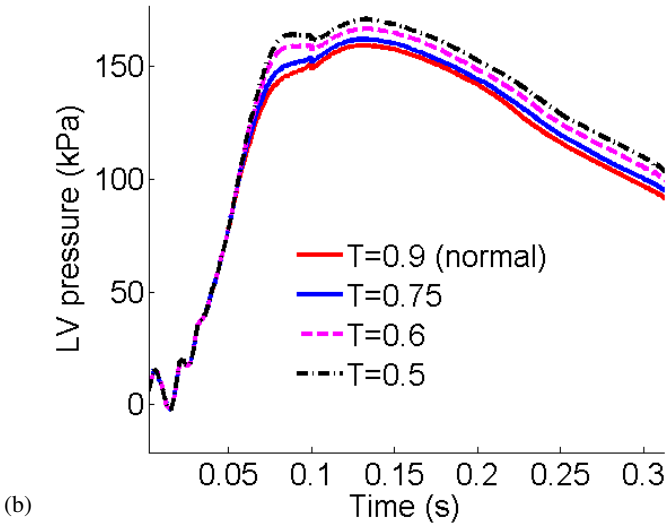

(b)

Figure 5.6: Averaged active tension (a) and the LV pressure (b) in systole when shortening systemic diastolic phase.

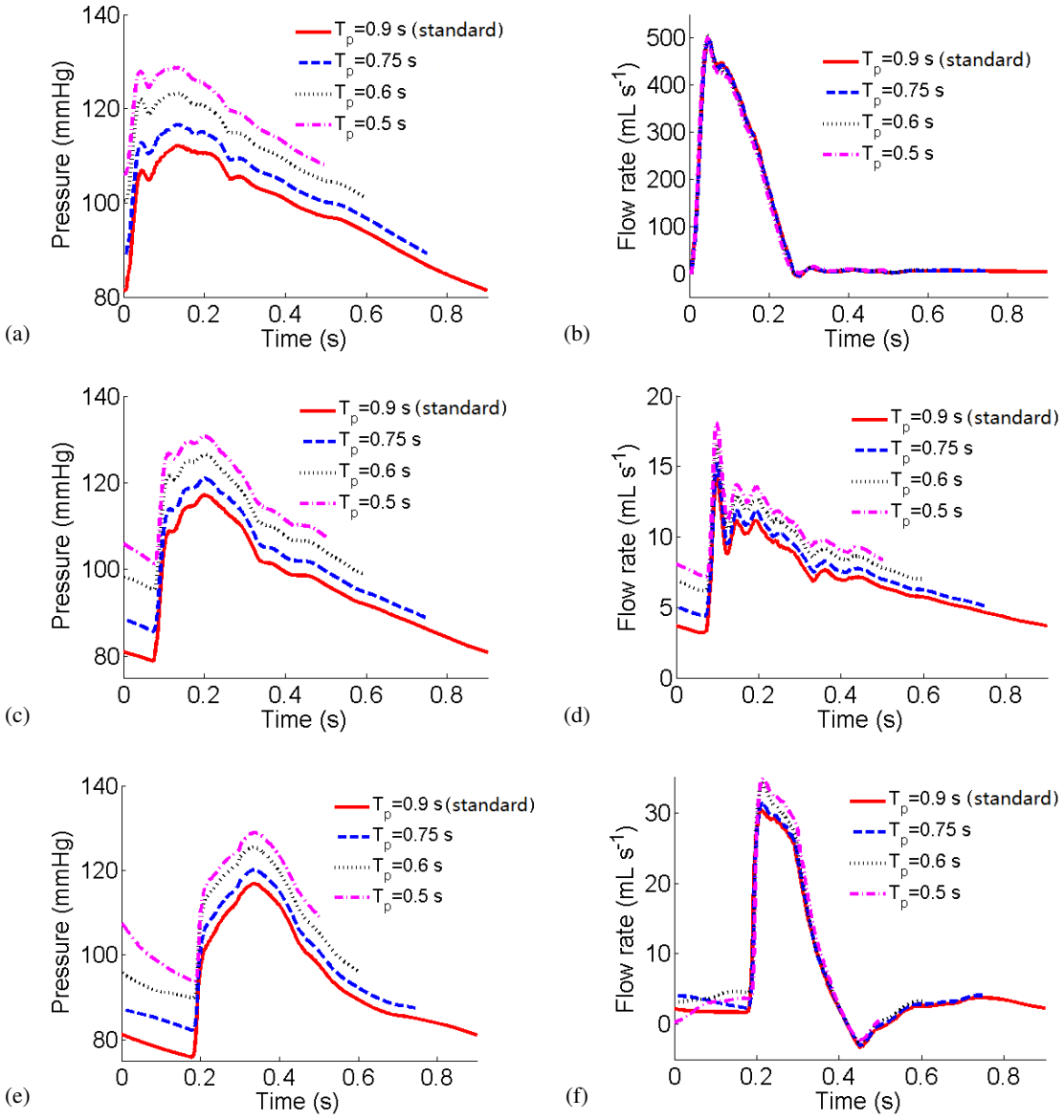

Figure 5.7: Comparisons of the pressure (left) and flow rate (right) in the ascending aorta ((a), (b)), the renal artery ((c), (d)) and the femoral artery ((e), (f)) when shortening the systemic diastolic phase. The length of period changed correspondingly from $T_{\mathrm{p}} = 0.9\,\mathrm{s}$ to $T_{\mathrm{p}} = 0.75, 0.6, 0.5\,\mathrm{s}$.

5.5 Results of changing end-of-diastolic pressure in coupled model

The results show that changing the $P_{\text{ED-LV}}$ has a big effect on the pressure-volume loop (Fig. 5.9 (d)), which shows a 4.64% increase of end-of-diastolic volume and 5.03% increase of the peak LV pressure when increasing the end-of-diastolic pressure from 8 mmHg to 10 mmHg. It also shows an 6.54% decrease in end-of-diastolic volume and 9.37% decrease of the peak LV pressure when decreasing the end-of-diastolic pressure from 8 mmHg to 6 mmHg. Changing the end-of-diastolic pressure also has substantial effect on the cardiac output per beat which is decreased by 13% with lower end-of-diastolic pressure and increased by 9.76% with the higher end-of-diastolic pressure. The length of ejection phase is shortened by 12.6 ms and lengthened by 11.2 ms, corresponding to 6 mmHg and 10 mmHg $P_{\text{ED-LV}}$ compared with the standard case (8 mmHg). Table 5.5 summarizes the end-of-diastolic arterial pressure (P_{EDA}), peak aortic pressure (P_a^*), peak LV pressure (P_{LV}^*), peak aortic flow rate (Q_{a}^*), the stroke volume (V_{s}) and the ejection period (T_{ej}) during systole for different value of $P_{\text{ED-LV}}$.

	P_{EDA} (mmHg)	P_{a}^* (mmHg)	P_{LV}^* (mmHg)	Q_{a}^* ($\text{mL}\,\text{s}^{-1}$)	V_{s} (mL)	T_{ej} (ms)
$P_{\text{ED-LV}}$ = 6 mmHg	78.72	108.65	145.80	459.43	65.22	247.0
$P_{\text{ED-LV}}$ = 8 mmHg (standard)	81.31	112.12	159.23	494.53	74.68	259.3
$P_{\text{ED-LV}}$ = 10 mmHg	81.31	114.51	168.42	509.12	82.14	269.1

Table 5.5: Summary of end diastolic pressure's effect on systolic LV function

The results of the pressure shows an equal change of the peak but barely change the trough pressure in all three groups of arteries when changing the $P_{\text{ED-LV}}$ in the LV, and the major change of pressure occurs after 100 ms during systole. Fig. 5.8 (a) shows that the peak pressure decreased by 3.05% with lower end-of-diastolic pressure (6 mmHg) and it increased by 2.24% with higher end-of-diastolic pressure (10 mmHg) in the ascending aorta. Changing the $P_{\text{ED-LV}}$ has substantial effect on the flow rate in the large arteries which is more dramatical compared to other disease-related cases (Fig. 5.8 (b), (d) and (f)). The peak flow rate decreased by 7.1% when $P_{\text{ED-LV}}$=6 mmHg and it increased by 3.0% when $P_{\text{ED-LV}}$=10 mmHg in the ascending aorta (Fig. 5.8 (b)). In Fig. 5.8 (f), the peak flow rate decreased by 7.5% when $P_{\text{ED-LV}}$=6 mmHg and increased by 3.8% when $P_{\text{ED-LV}}$=10 mmHg

in the femoral artery compared with the standard case ($P_{\text{ED-LV}}$=8 mmHg).

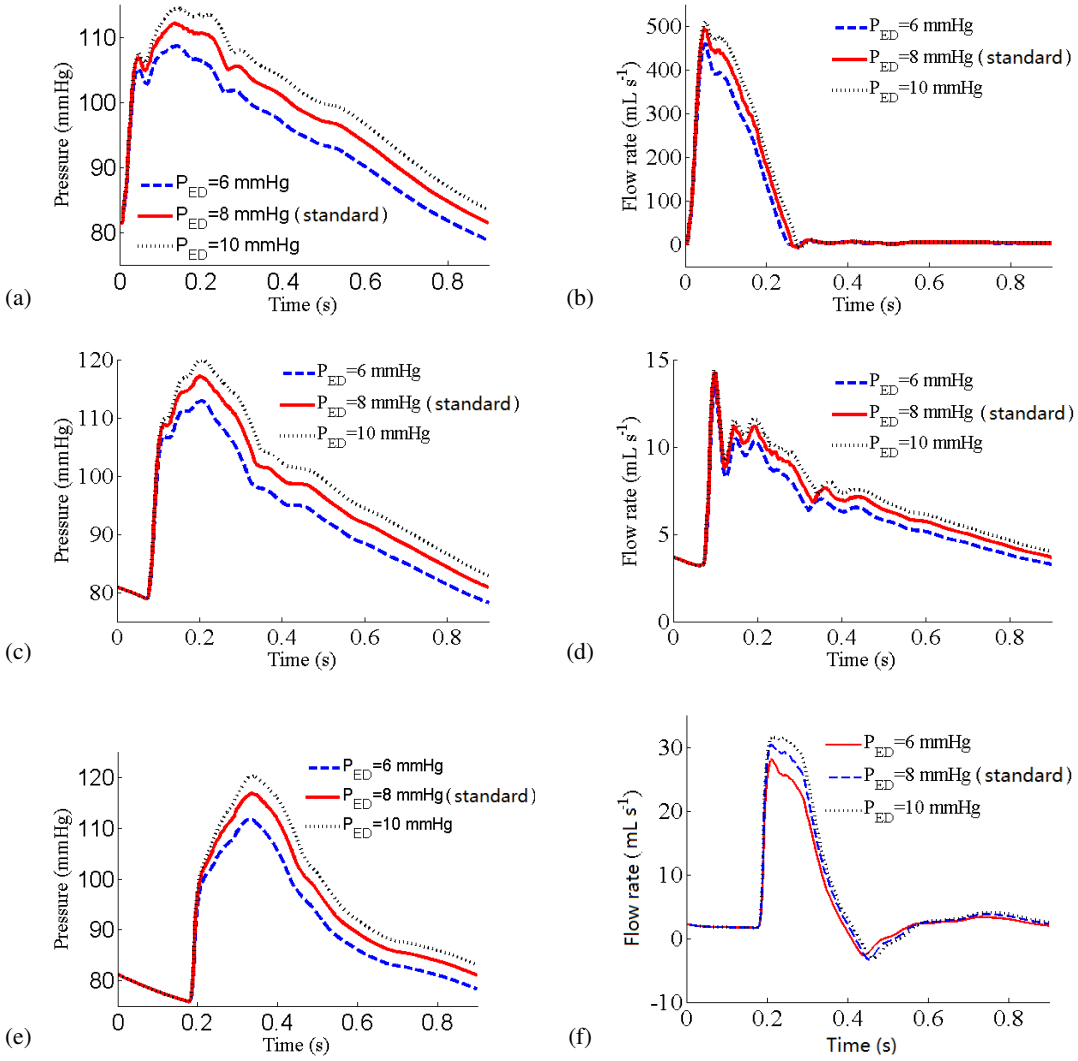

Figure 5.8: Comparisons of the pressure (left) and flow rate (right) in the ascending aorta ((a), (b)), the renal artery ((c), (d)) and the femoral artery ((e), (f)) when changing the $P_{\text{ED-LV}} = 8$ mmHg to $P_{\text{ED-LV}} = 6, 10$ mmHg.

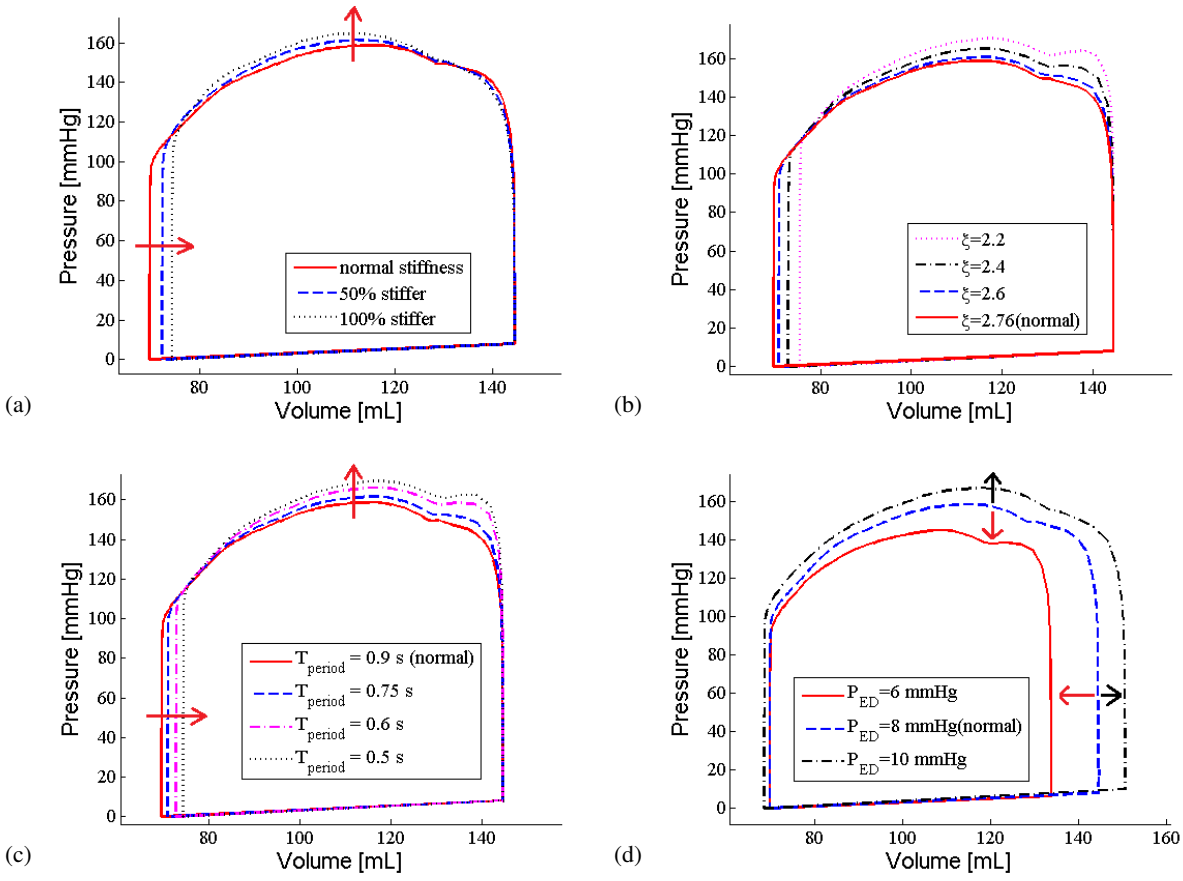

Figure 5.9: Comparisons of the pressure-volume loops of the left ventricle between the standard case and disease-related cases. The effects of stiffening the large arteries, functional rarefaction, shortening the diastolic phase, and changing the end-of-diastolic pressure are shown from left to right.

5.6 Comparison with an isolated systemic model

The results of the standard case and disease-related cases 1-3 are compared with the results calculated using Olfusen *et al*.'s [91] model with the cardiac output from coupled model in the standard case as inlet flow rate boundary condition instead of a dynamic LV, and the other parameters are kept the same as those in the coupled model. Thus, we can compare the difference between the circulation model with and without a dynamic LV, which is important for both mathematical modelling and clinical analysis.

In Figs. 5.10 and 5.11, both the pressure and flow rate from coupled model (red) show the same trends compared with circulation model (blue) simulating different situations of diseases. However, the peak values for pressure and flow rate are different between two models, in which the peak pressures and flow rates in the coupled model are lower than those in the circulation model.

The results show that the difference of the peak pressure is 3.8 mmHg in the ascending aorta (Fig. 5.10 (a)), and 3.2 mmHg in the femoral artery (Fig. 5.10 (b)) when stiffening the large arteries by 100%. The peak flow rate in the coupled model is also lower than that in the circulation model. The difference of peak flow rate is 27.6 mL in the ascending aorta (Fig. 5.11 (a)), and 1.7 mL in the femoral artery (Fig. 5.11 (b)) when stiffening the large arteries by 100%.

The results of the most severe functional rarefaction ($\xi = 2.4$) show that the coupled model has a lower peak pressure in three groups of large arteries than the circulation model, and the major difference occurs from the middle systole and ends with lower end of systemic diastolic pressure compared with the circulation model. The difference of the trough pressure is approximately 2 mmHg in the ascending aorta and the femoral artery (Fig. 5.11 (c) and (d)). The flow rate from the coupled model shows a faster decrease after the first peak in the aorta and limb arteries compared with those in the circulation model (Fig. 5.11 (c), (d)). It also shows a shorter ejection phase and an earlier arrival of back waves in the coupled model compared with the circulation model (Fig. 5.11).

The effects of shortening the systemic diastolic phase in two models are quite the same, but the peak pressure and peak flow rate are slightly lower in the coupled model than those in the circulation model (Figs. 5.10 (e), (f) and Figs. 5.11 (e), (f)). The peak pres-

sure arrives 3.2 ms earlier in the femoral artery from the coupled model than that in the circulation model (Fig. 5.10 (f)).

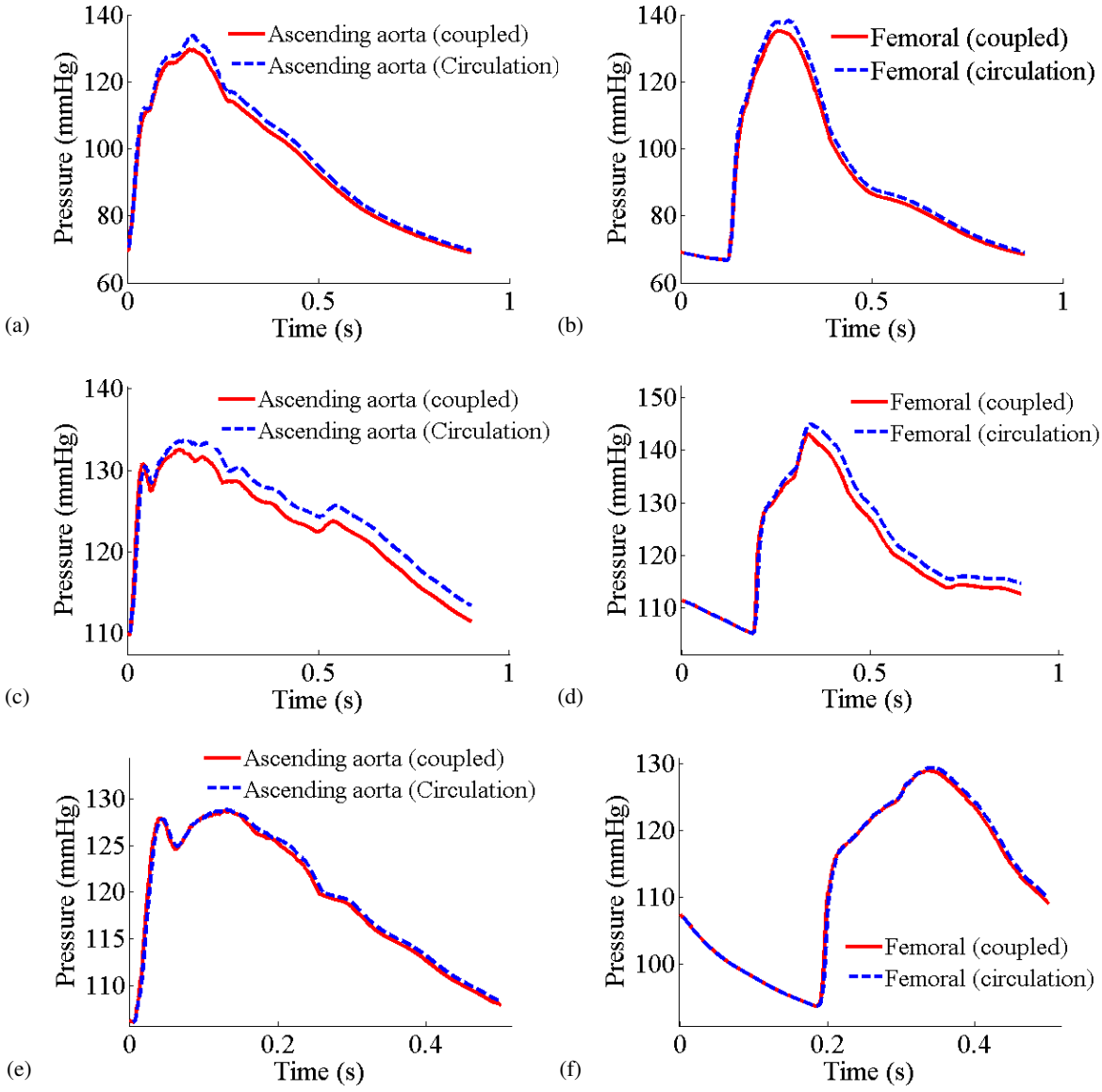

Figure 5.10: Comparisons of the pressure in the aorta ((a), (c) and (e)), and the limb arteries ((b), (d) and (f)) between the coupled model and the circulation model with prescribed cardiac output. The effects of stiffening the large arteries by 100%, the most sever functional rarefaction ($\xi = 2.4$), and shortening the diastolic phase (T$=0.5$ s) are from the top to the bottom in each group.

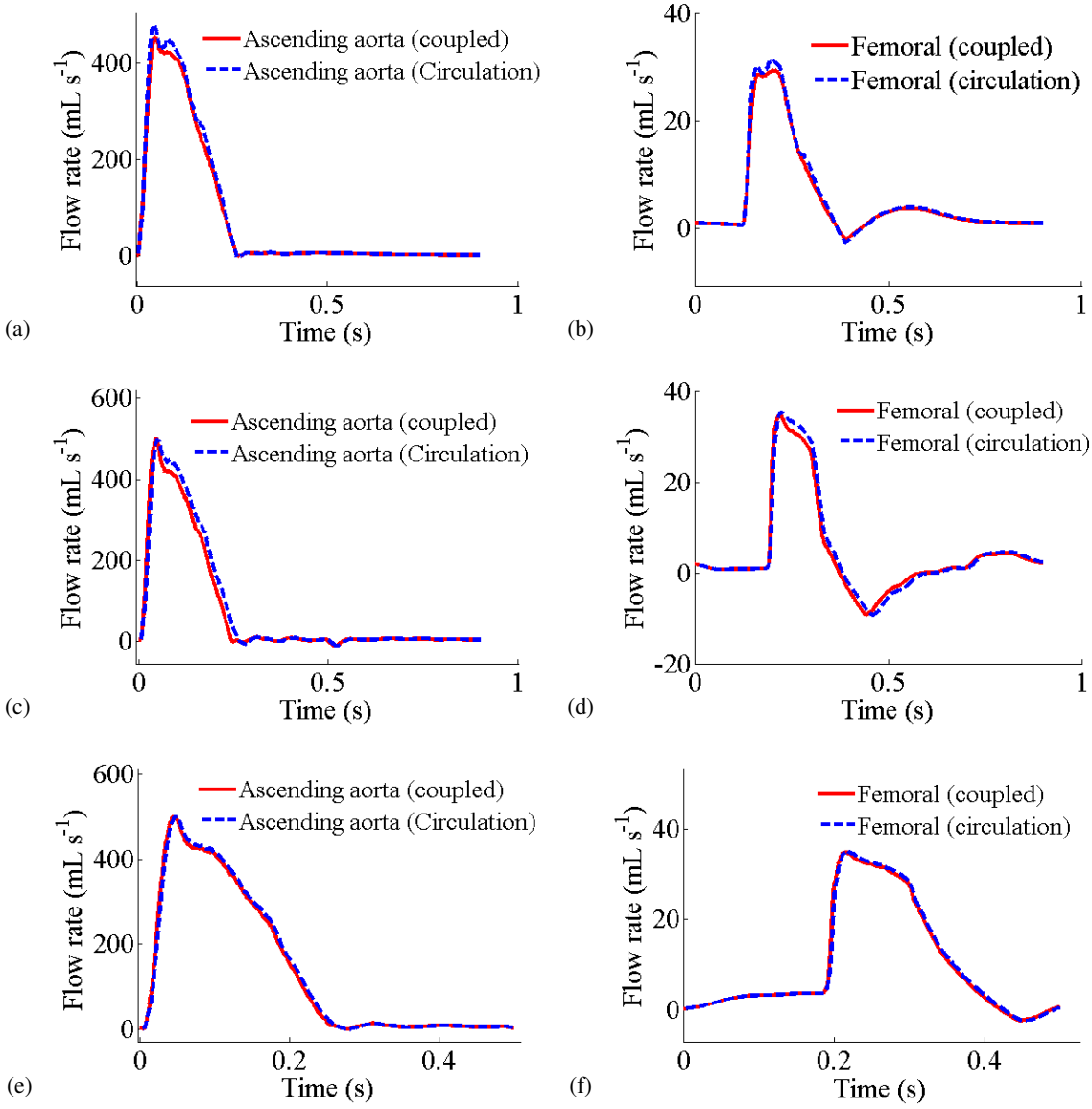

Figure 5.11: Comparisons of the flow rate in the aorta ((a), (c) and (e)), and the limb arteries ((b), (d) and (f)) between the coupled model and the circulation model with prescribed cardiac output. The effects of stiffening the large arteries by 100%, the most sever functional rarefaction ($\xi = 2.4$), and shortening the diastolic phase (T$=0.5$ s) are from the top to the bottom in each group.

5.7 Discussion

In this chapter, we simulate four pathological cases and present the effects on the LV function and the systemic arteries for each case, i.e. stiffening of the large arteries, functional rarefaction in the vascular beds, shortening the systemic diastolic phase, and varied end-of-diastolic pressure. The results show that different pathology conditions have different effects on the ventricular preload and afterload, thus affect the LV contractility and the pressure and flow rate in the arteries.

The first two cases are related to increased afterload, and the last case relates to an increase or a decrease in preload, while changing the heart beat rate affects both preload and afterload, but in this study we only model the changing of afterload by shortening the arterial diastolic phase.

- Stiffening of the large arteries correspond to an decrease of arterial compliance, which leads to an increase of the aortic pressure, and the increase of aortic pressure is regarded as an increase of ventricular afterload.
- The functional rarefaction increases both the peak and the mean pressures in the LV and along the large arteries, which agrees with the hypothesis that rarefaction in vascular beds may lead to hypertension in the large arteries [2, 85]. Since it increases the aortic pressure, this case also relates to an increase of ventricular afterload.
- Shortening the arterial diastolic phase leads to a higher than normal end-of-diastolic pressure in the aorta, so the LV contracts for a longer to reach a higher AV opening pressure during systole, which indicates an increase of ventricular afterload. The results quantify the increasing of both the peak and trough pressure along the arterial tree during systole, which corresponds to the physiological phenomena that the shortening of diastolic phase leads to higher LV and arterial pressures [57]. The results also show a decrease of the ejection duration, which agreed with the study of Wilkinson et al. [130].
- Increasing $P_{\text{ED-LV}}$ corresponds to an increase of the end-diastolic volume, and thus increase the LV preload. Changing the $P_{\text{ED-LV}}$ also has an effect of flow rate in the arteries, unlike the other three disease-related cases, in which the flow rates in the LV and in the aorta barely change.

Effects on the stroke volume

The stroke volume is determined by the end-of-diastolic volume and end-of-systolic volume, $V_s = V_{\text{ES}} - V_{\text{ED}}$. The results show that increasing the afterload leads to an increase of the end-of-systolic volume, and thus decrease the stroke volume, while increasing the preload increases the end-of-diastolic volume, and contribute to an increase of the stroke volume. The effects on the stroke volume is summarized in Fig. 5.12.

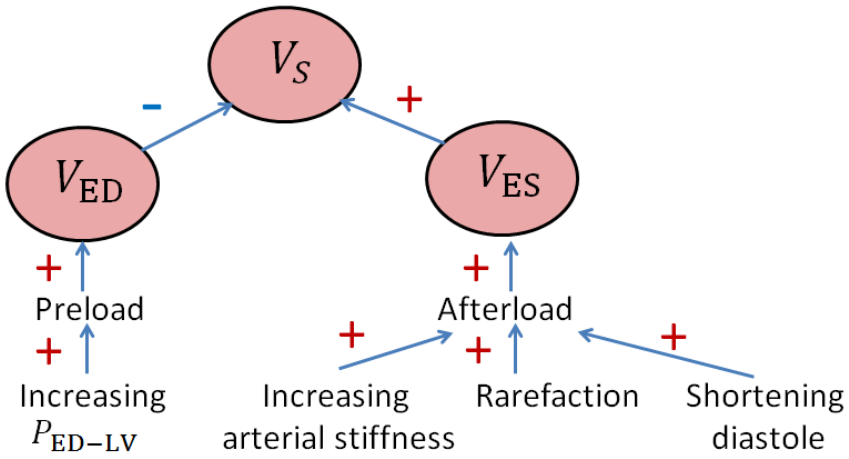

Figure 5.12: Effects of preload and afterload on the stroke volume. '+' denotes increase; '−' denotes decrease.

Effects on the ventricular contractility

A common effect of the first three pathological conditions on the ventricular contractility is that they all lead to an increases of the active tension in the LV during systole. The results of changing $P_{\text{ED-LV}}$ in the fourth case show that increasing $P_{\text{ED-LV}}$ increases the LV active contraction, while decreasing $P_{\text{ED-LV}}$ has the opposite effect. The effect of the LV inotropy is summarized in Fig. 5.13, which agreed with the study of Klabunde [57].

Effects on the aortic pressure

The aortic pressure is mainly determined the stroke volume and the aortic compliance Klabunde [57]. In this study the effects of four pathological conditions relate to changes in the stroke volume and the arterial compliance. To be specific, stiffening the large arteries and the functional rarefaction decreases the arterial compliance, and decrease the stroke volume, which ends up to an increase of the aortic pressure. Shortening the arterial diastolic phase

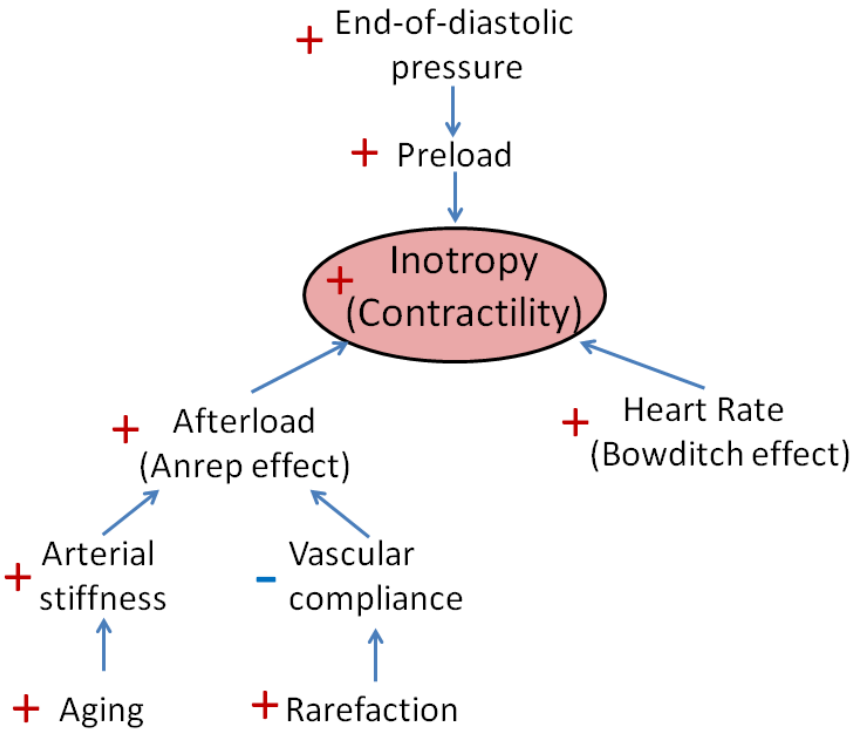

Figure 5.13: A re-sketched diagram of factors relate to increased inotropy based on the study of Klabunde [57]. '+' denotes increase; '−' denotes decrease.

leads to an increase of the end-of-diastolic arterial pressure, and a decrease of the stroke volume, which leads to an increase of the aortic pressure. Increasing the $P_{\text{ED-LV}}$ increases the V_{ED}, leading to an increase of the stroke volume, and thus increase the aortic pressure, while decreasing the $P_{\text{ED-LV}}$ has the opposite effect.

Effects on the pressure-volume loops

By comparing the P-V loops in Fig. 5.9 (a), (b) and (c), we observe that there is a trend for the cardiac output to be maintained by slightly changing the end-of-diastolic volume when disease occurs in the systemic arteries. However, when the end-of-diastolic pressure is changed (Fig. 5.9 (d), the cardiac output changes dramatically, and this affects both the LV pressure and the flow rate significantly throughout the system. Thus, when disease occurs in the arterial system, the LV works with increased inotropy and suffers higher LV pressure than normal, and changes in inotropy are a prominent feature of cardiac muscle, that lead to remodelling over long times [57].

Comparing the results from the coupled model with those from the circulation model with a prescribed cardiac output as inflow in Section 3.6, it demonstrates that the both the pressure and flow rate from the coupled model are lower than those from the circulation model with prescribed cardiac output. In the coupled model, when disease occurs, the LV tends to increase the active tension and decrease the cardiac output to reduce the increase of pressure in the arterial system, as well as to decrease the flow rate in the late systole.

Chapter 6

Effects of aortic valve stenosis

The main interactions between the LV and the systemic arteries depend on the ejection phase during systole. Thus, in order to provide more physiological conditions, we couple a lumped-parameter (0D) valve model between the LV and the SA model to develop a cardio-valvular-arterial model (LV-AV-SA model).

In this chapter, we first describe the mathematical definition of the 0D AV model. Secondly, the 3D-0D-1D system is presented, and the coupling and time-integration conditions during systole are described. Thirdly, we explain how to choose the parameters in the AV model when it is coupled in the LV-SA system. Two different conditions of the AV, i.e. a normal condition referring to for a healthy subject, and disease condition referring to a mild stenosis of the AV, are simulated in the coupled LV-AV-SA model. The results of the LV-AV-SA model with two AV conditions are compared with the standard case (without an AV) in the LV-SA model, followed by a discussion at the end of this chapter.

6.1 Modelling the aortic valve

Model description

The active valve motion is simulated by a lumped-parameter (0D) valve model first designed by Sun et al. [115], in which the pressure drop across the valve is described by the

Bernoulli equation

$$\Delta p = Bq|q| + L\frac{dq}{dt}, \tag{6.1}$$

where Δp is the pressure difference across the valve, q is the flow rate through the valve, B is a Bernoulli resistance and L is the blood inertance. The Bernoulli resistance B corresponds to the pressure difference caused by the convective acceleration and the dynamic pressure losses due to the diverging flow field downstream of the vena contracta, while the blood inertance L relates to the pressure differences caused by the rapid acceleration and deceleration of the blood across the valve. The Poiseuille-type viscous losses (proportional to q) are small compared with convective acceleration and inertance effects, and thus are neglected [115]. Mynard et al. [80] further developed this valve model by relating the two coefficients B and L to some physiological variables, instead of using constant values as in Sun et al. [115]. Thus this valve model can be used to investigate a larger range of context, including the normal valve function and pathological conditions, such as valve stenosis, valve regurgitation, etc. The Bernoulli resistance is defined as [80]

$$B = \frac{\rho}{2A_{\text{eff}}^2}, \tag{6.2}$$

where ρ is the blood density, A_{eff} is the effective valve area. The blood inertance is defined as

$$L = \frac{\rho l_{\text{eff}}}{A_{\text{eff}}}, \tag{6.3}$$

where l_{eff} is the effective length. To describe the valve motion, the effective area is considered to be a variable and we define a valve state index ($0 \leqslant \zeta \leqslant 1$; $\zeta = 0$, valve closed; $\zeta = 1$, valve fully open) such that

$$A_{\text{eff}}(t) = [A_{\max}(t) - A_{\min}(t)]\zeta(t) + A_{\min}(t) \tag{6.4}$$

where $A_{\max}(t)$ and $A_{\min}(t)$ are the maximum and minimum effective areas defined as

$$A_{\min}(t) = M_{\text{rg}} A_{\text{ann}}(t), \tag{6.5}$$

$$A_{\max}(t) = M_{\text{st}} A_{\text{ann}}(t) \tag{6.6}$$

where A_{ann} is the annulus area. Changing the values of parameters M_{rg} and M_{st} represents different valve conditions. A healthy valve is characterized by $M_{\text{rg}} = 0$ and $M_{\text{st}} = 1$. $M_{\text{rg}} > 0$ represents a regurgitant (or leaky) valve, since $A_{\min} > 0$, and the valve is not fully closed. By contrast, $M_{\text{st}} < 1$ represents valve stenosis, since $A_{\max} < A_{\text{ann}}$, such that

the valve is not fully open. In this study, it is assumed that the rate of valve opening and closing is determined by only two variables: (1) the pressure drop Δp between the immediate proximal and distal sites of the valve; and (2) the current valve position ζ. The rate of opening (occurs when $\Delta p \geqslant 0$) is determined by

$$\frac{d\zeta}{dt} = (1-\zeta)K_{\text{vo}}(\Delta p - \Delta p_{\text{open}}) \tag{6.7}$$

where K_{vo} is the opening rate coefficient (units: $\text{mmHg}^{-1}\,\text{s}^{-1}$). The rate of valve closing (occurs when $\Delta p < 0$) is determined by

$$\frac{d\zeta}{dt} = \zeta K_{\text{vc}}(\Delta p - \Delta p_{\text{close}}) \tag{6.8}$$

where K_{vc} is the closing rate coefficient (units: $\text{mmHg}^{-1}\,\text{s}^{-1}$).

At each time step, the coefficients in (6.1) are calculated from (6.2) and (6.3), and the updating flow rate is calculated by a first order discretisation of (6.1), yielding

$$q^{n+1} = q^n + \frac{\Delta t}{L}(\Delta p^n - Bq^n|q^n|). \tag{6.9}$$

An initial valve state and flow rate, $\zeta^0 = 0$ and $q^0 = 0$, are specified at the start of the simulation. To demonstrate the valve's performance, a sinusoidal pressure difference with increasing amplitude is imposed as input (Fig. 6.1 (a)),

$$\Delta p(t) = (n+1)\sin(t), \quad t \in [n\pi, (n+1)\pi], \quad \text{for} \quad n = 0, 1, ..., 5. \tag{6.10}$$

The corresponding valve motion ζ and the flow rate q predicted by the AV model are shown in Fig. 6.1 (b) and (c). As the pressure difference grows, the opening and closing of the valve become faster, and the peak of flow rate increases, while increasing the opening and closing rate coefficients K_{vo}, and K_{vc} has the same effects on the opening and closing rates of the valve, but only small effects on the flow rate.

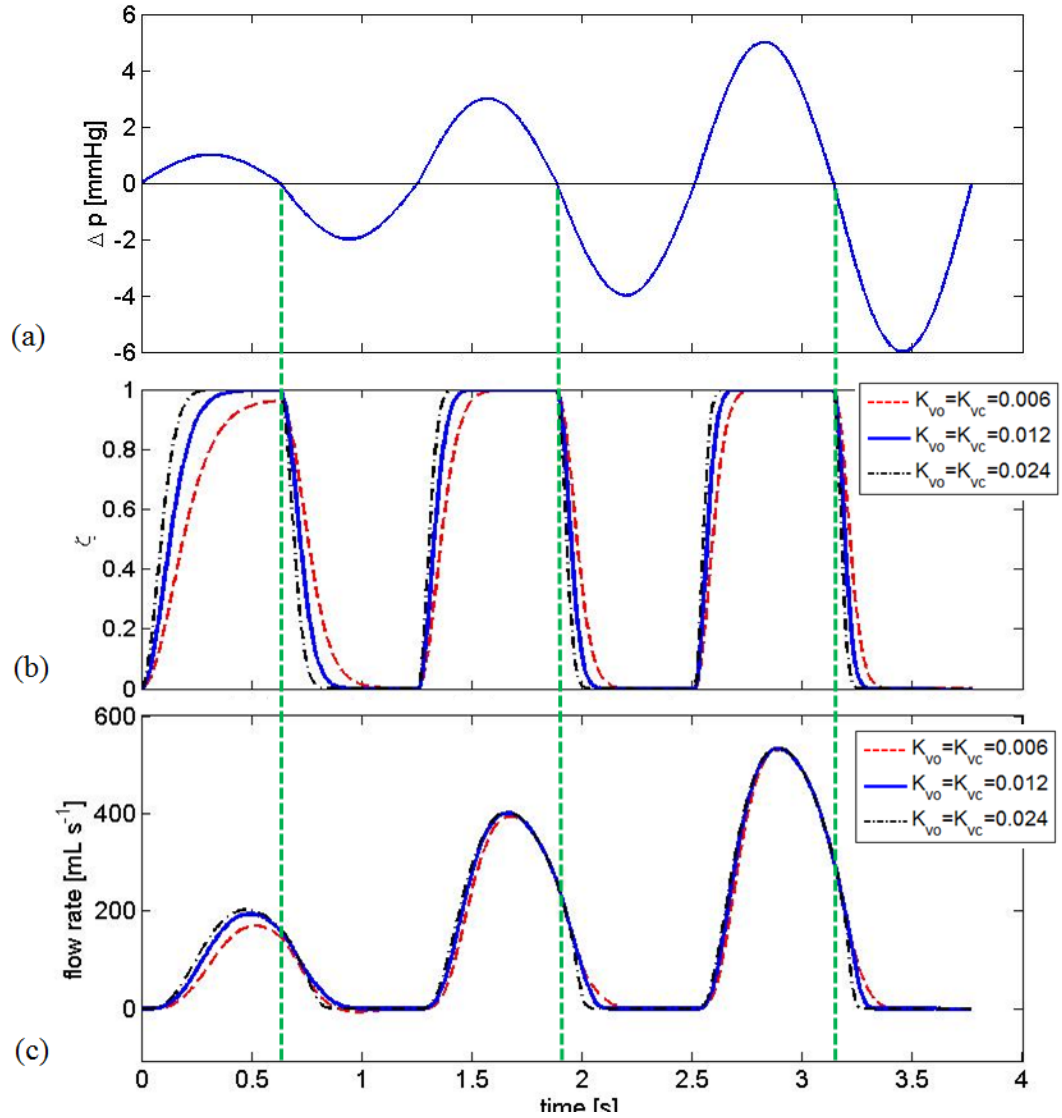

Figure 6.1: The valve motion (b) and flow rate (c) predicted by the AV model by using a sinusoidal pressure difference with increasing amplitude (a) given by (6.10). In this example, $K_{\text{vo}} = K_{\text{vc}} =$ 0.006 (dashed line in red), 0.012 (solid line in blue), 0.025 (dash-dot line in black).

6.2 Coupling the aortic valve model with the LV-arterial model

The 0D valve model is coupled into the LV-SA model described in Chapter 3 to mimic the opening and closing process of the aortic valve (or providing a dynamic pressure drop across the valve), so that we can get more physiological results during systole as well as studying the cardio-valvar-vascular interactions.

6.2.1 The 3D-0D-1D system

As described in Chapter 3, we have accomplished a coupled LV-arterial model including a 3D dynamic LV and a 1D systemic arterial model. To couple the valve model between the 3D and 1D segments, a proper coupling condition needs to be defined between each model. As shown in Fig. 6.2, for this 3D-0D-1D system, we assume that the flow rate does not change between the proximal and distal sites of the AV

$$Q_{\mathrm{AV}} = Q_{+} = Q_{-}. \tag{6.11}$$

The cross-valve pressure difference is defined as

$$\Delta p \equiv \bar{p}_{-} - \bar{p}_{+}, \tag{6.12}$$

where $\bar{p}_{-}$ is the cross-sectional averaged pressure at the outlet tract of the LV, and $\bar{p}_{+}$ is the cross-sectional averaged pressure at the inlet of the aorta. After calculating the pressure difference Δp from the AV model, the pressure $\bar{p}_{-} = \bar{p}_{+} + \Delta p$ is fed back as the pressure boundary condition for the outlet plane of the LV model.

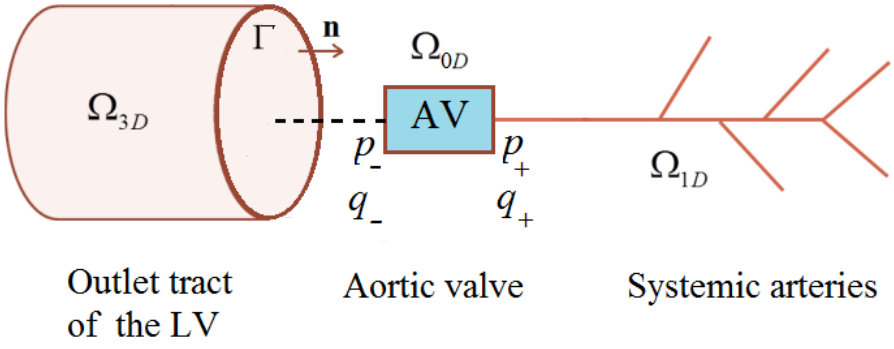

Figure 6.2: The 3D-0D-1D system. The AV model connects the outlet tract of the LV model and the inlet of the ascending aorta of the SA model, and provides a time-dependent cross-valve pressure drop Δp between the LV and the SA. Subscripts $+$ and $-$ denote variables in the SA model and the LV models. The cross-valve pressure difference is $\Delta p \equiv \bar{p}_{-} - \bar{p}_{+}$.

6.2.2 The discretization method

In order to use the flow rate to calculate the pressure difference from the AV model, we discretize (6.1) into

$$\Delta p^n = Bq^n|q^n| + L\left(\frac{q^n - q^{n-1}}{\Delta t}\right). \tag{6.13}$$

When $\Delta p^n \geqslant 0$, The aortic valve opens, and the rate of opening is discretized as

$$\frac{\zeta^n - \zeta^{n-1}}{\Delta t} = (1-\zeta^{n-1})K_{\text{vo}}\Delta p^n \quad \Rightarrow \quad \zeta^n = (1-\zeta^{n-1})K_{\text{vo}}\Delta p^n \Delta t + \zeta^{n-1}. \tag{6.14}$$

When $\Delta p^n < 0$, the aortic valve enters the closing state, and the rate of closing is discretized as

$$\frac{\zeta^n - \zeta^{n-1}}{\Delta t} = \zeta^{n-1}K_{\text{vc}}\Delta p^n \quad \Rightarrow \quad \zeta^n = \zeta^{n-1}K_{\text{vc}}\Delta p^n \Delta t + \zeta^{n-1}. \tag{6.15}$$

As a testcase, a sinusoidal flow rate with increasing amplitude is used as the inlet boundary condition (Fig. 6.3 (a)),

$$q(t) = (150+100n)(1+\sin(t)), \quad t \in [(4n-1)\pi/2, (4n-3)\pi/2)], \quad \text{for} \quad n = 0,1,2,3. \tag{6.16}$$

The corresponding valve motion ζ and the pressure difference Δp predicted by the AV model are shown in Fig. 6.3 (b) and (c). With higher flow rates, the valve opening and closing rates are faster, and the peak of the pressure difference increases.

Since the coupled LV-SA model is a dynamic system running with small time steps, the cross-sectional averaged flow rate in the LV proximal to the AV is noisy if we look at the flow rate difference at each time step. It cannot be used directly as inlet flow for the AV model, since a small change in dq in the second term of (6.13) has a dramatic effect on dq/dt when dt is very small. In order to smooth the flow rate, we use a weighted moving-average method, which has the same effects as a low-pass filter [31], to attenuate the high frequencies in the input signal and smooth the flow rate, i.e.

$$Q^n = sQ^n + (1-s)Q^{n-1}, \quad s \in [0,1], \tag{6.17}$$

where s is the smoothing factor. The first term is the contribution of the current input, and the second term refers to the inertia from the previous time step. As s gets closer to zero, the inertia increases, so that the higher frequencies are attenuated and the flow rate

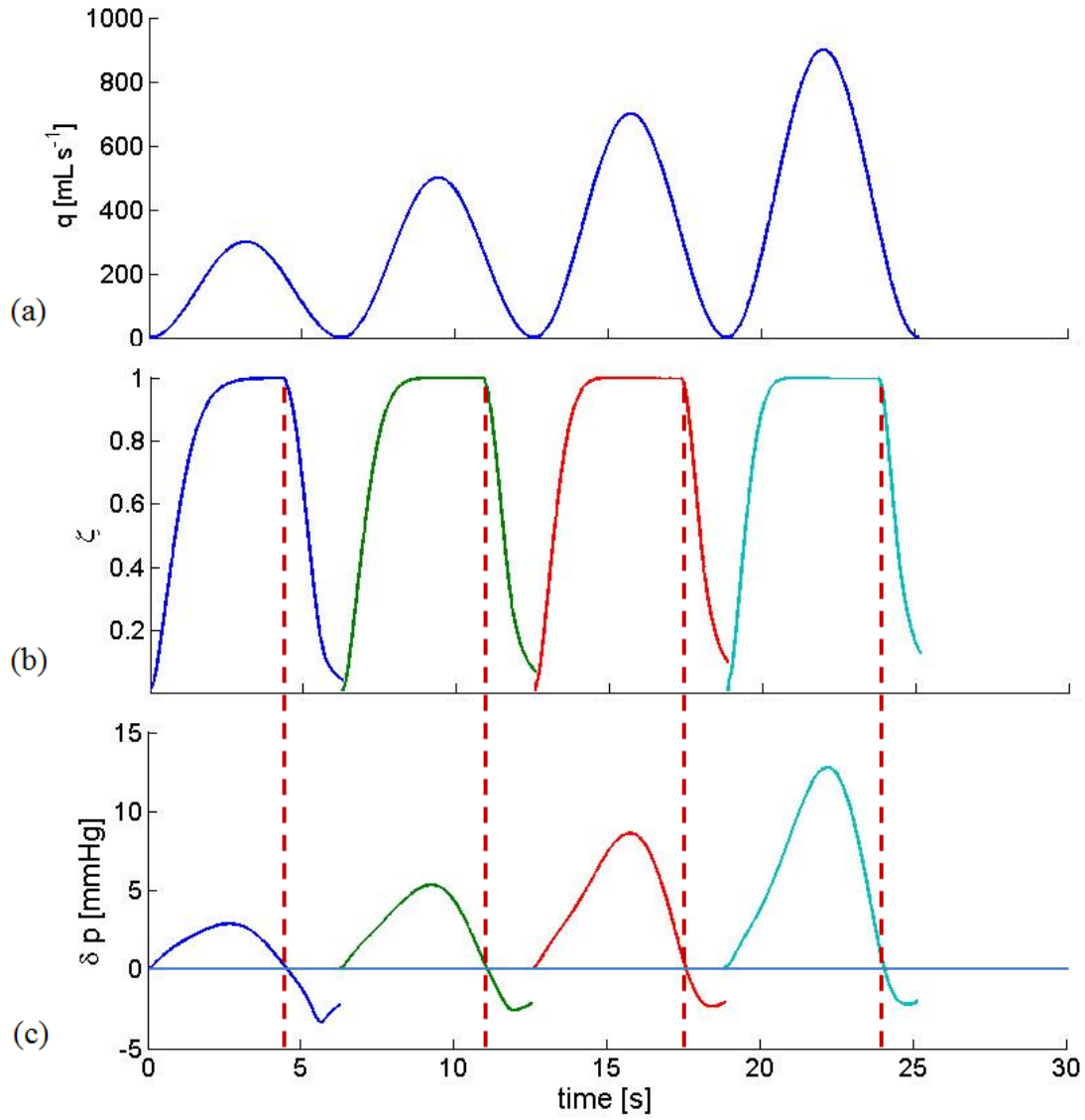

Figure 6.3: The valve motion (b) and flow rate (c) predicted by the AV model by using a sinusoidal flow rate with increasing amplitude (a). In this example, $K_{\mathrm{vo}} = K_{\mathrm{vc}} = 0.012$.

becomes smoother; whereas, if s tends to one, the higher frequencies are retained and the smoothing effect is small. For the cardiac output from the LV-SA model in the standard case, we choose $s = 0.04$, and the corresponding effects of the flow rate and dq are shown in Fig. 6.4 (a) and (b).

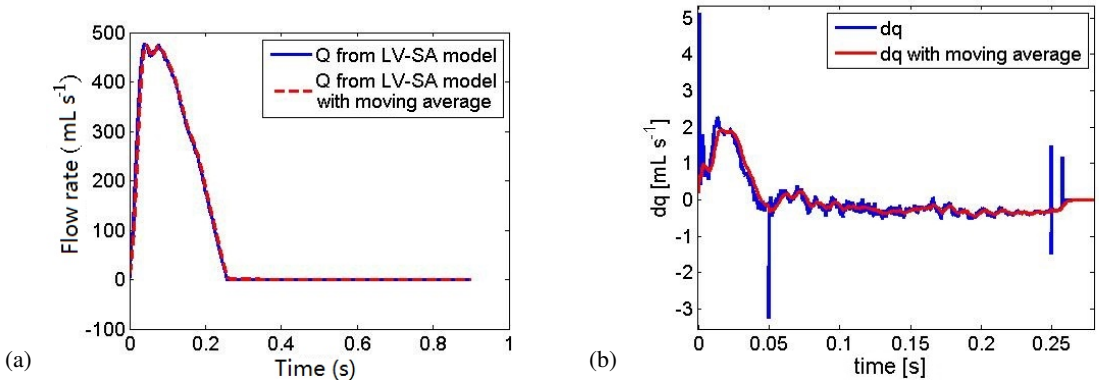

Figure 6.4: The comparisons between the original cardiac output from the standard case in the LV-SA model and the cardiac output with weighted moving average method (a), and the corresponding effects of dq (b). The smoothing factor $s = 0.04$.

6.2.3 Time integration conditions

In the LV-SA model, the LV model is running in computational time with a longer period than real physiological time and a varied length of time step to ensure the computational stability, while the SA model is running in physiologically realistic time with a fixed time step, so for the AV model in the coupled system, we use $\Delta t_{AV} = \Delta t_+ = 0.9/8192 \approx 1.099 \times 10^{-4}$ s, i.e. the same as that in the SA model. The AV model is only applied during ejection phase in the coupled model. The AV opens when

$$\bar{p}_- > \bar{p}_+, \tag{6.18}$$

$\bar{p}_-$ being the pressure in the LV proximal to the AV, and $\bar{p}_+$ is the pressure in the aorta distal to the AV. During ejection, the pressure difference Δp is predicted from the AV model and fed back to the LV using the interpolation method

$$p_-^n = \frac{(p_+^m + \Delta p^m - (p_+^{m-1} + \Delta p^{m-1}))(t_-^n - t_+^{m-1})}{t_+^m - t_+^{m-1}} + (p_+^{m-1} + \Delta p^{m-1}), \tag{6.19}$$

where subscripts $+$ and $-$ denote variables in the SA and the LV model respectively, and m denotes the current time step in the SA, n denotes the time step and the LV model. Systole ends when the valve state $\zeta = 0$ when the AV fully closed, or when back flow occurs ($q_- < 0$).

6.2.4 Parameter values for the aortic valve model

The value for the annulus area $A_{\text{ann}} = 4.9\,\text{cm}^2$, and the effective length $l_{\text{eff}} = 6\,\text{cm}$ are taken from measurements. For simulating the normal and stenosis valve condition in the coupled model, the values of the other parameters are given in Table 6.1.

Cases	M_{st}	M_{rg}	K_{vo}	K_{vc}
Normal	1	0	0.012	0.012
Mild stenosis	0.5	0	0.001	0.008

Table 6.1: Values of parameters in the AV model for normal and mild stenosis conditions.

The initial value for valve state index and flow rate, $\zeta^0 = 0.01$ and $p^0 = 10\,\text{dyne}\,\text{cm}^2 \approx 7.50 \times 10^{-3}$ mmHg, are specified to start the simulation.

6.3 Results

In this section, the resulting pressure and waveforms are presented for the coupled LV-AV-SA model. Two different conditions of the AV, i.e. a normal healthy condition and a diseased mild AV stenosis condition are simulated. The parameters for both AV conditions are listed in Table 6.1 and all the other parameters are the same as those in the LV-SA model for standard case (Table 4.1).

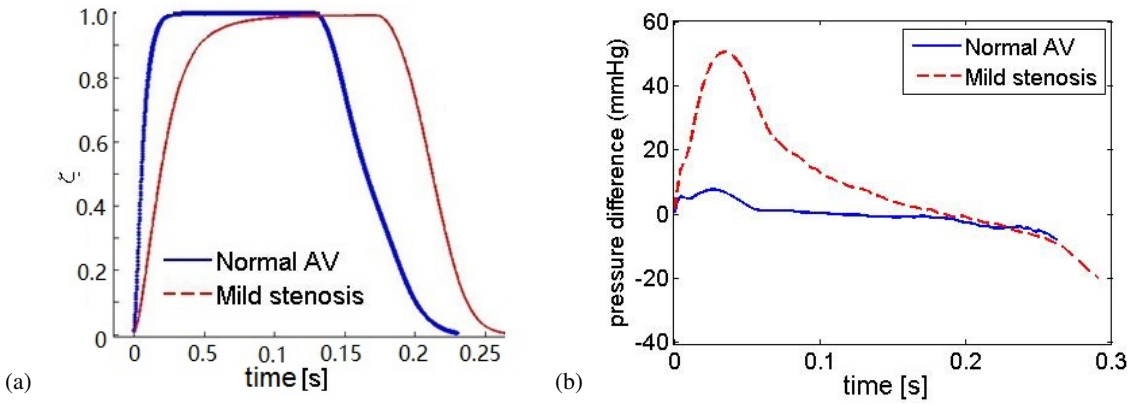

Figure 6.5: The valve state (a) and the pressure difference (b) predicted from the coupled LV-AV-SA model with normal AV condition (solid blue) and the mild stenosis condition (dashed red).

The simulated aortic valve motion and the pressure difference for normal AV and stenosis AV conditions are shown in Fig. 6.5. The pressure difference across the AV for the normal AV condition ranges from -8.15 mmHg to 7.62 mmHg. In contrast, it ranges from -20.15 mmHg to 50.62 mmHg for the mild AV stenosis. Table 6.2 summarizes the end-of-diastolic arterial pressure (P_{EDA}), peak aortic pressure (P_a^*), peak LV pressure (P_{LV}^*), the maximum and minimum pressure difference ($\Delta p_{\max}$ and $\Delta p_{\min}$) across the AV, peak aortic flow rate (Q_{a}^*), and the ejection period (T_{ej}) during systole. The P_{EDA} changes by $< 1\%$ for both normal AV and mild stenosis AV compared with the coupled model without the AV, while P_a^* increases by 1.9% and 36.3% for the normal AV and stenosed AV respectively. P_{LV}^* increases by less than 1% for the normal AV condition, but by 13.1% with mild stenosis of the AV. Q_{a}^* decreases by 3.5% to 4.9% with normal and stenosed AV, compared with the absence of the AV. The pressure and flow rate wave forms during systole in the LV are shown in Fig. 6.6. The length of ejection phase is 3.2 ms and 31.8 ms longer for the normal AV and stenosed AV, compared with the absence of the AV.

	P_{EDA} (mmHg)	P_{a}^* (mmHg)	P_{LV}^* (mmHg)	$\Delta p_{\max}$ (mmHg)	$\Delta p_{\min}$ (mmHg)	Q_{a}^* ($\mathrm{mL\,s^{-1}}$)	T_{ej} (ms)
standard case	81.31	110.3	159.23	0	0	494.53	259.3
normal AV	81.73	112.4	159.9	50.62	-20.15	477.1	262.5
mild stenosis AV	81.99	150.4	180.1	7.62	-8.15	469.9	291.1

Table 6.2: The effects of adding a normal and a stenosed AV on systolic LV function.

The pressure-volume loops for the LV-AV-SA model with normal AV and stenosis AV conditions are compared with the standard case in the LV-SA model (Fig. 6.7). At early systole, it shows a small increase of 5.1 mmHg of the LV pressure when a normal AV is added in the LV-SA system, while there is dramatic increase of 33.4 mmHg in the LV pressure with a mild AV stenosis (diamonds in Fig. 6.7).

Figure 6.8 compares the active tension between the LV-AV-SA model with normal or stenosed AV conditions and the LV-SA model without the AV. By adding a normal AV into the LV-SA model, the peak active tension increases by 8.7%, and the whole active tension profiles during systole have a similar trend. Comparing with the normal AV condition, for an AV with a mild stenosis, the peak active tension increases by 10.2%, and it shows an

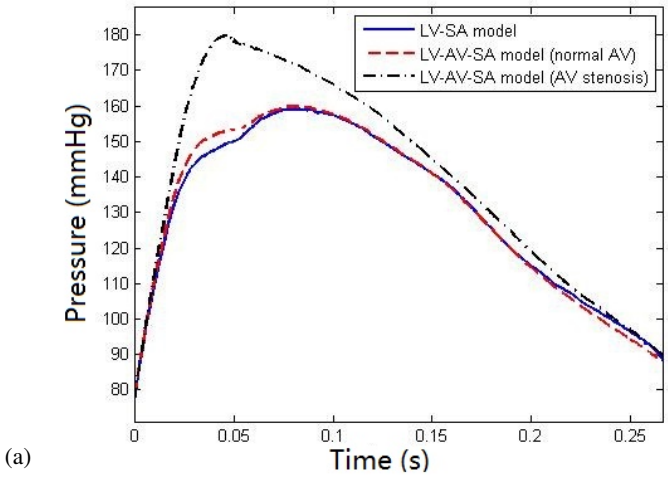

(a)

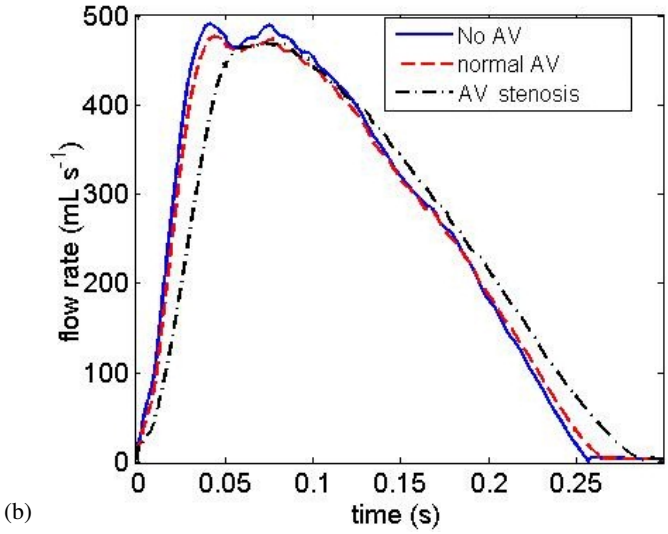

(b)

Figure 6.6: Effects of adding a normal AV (dashed red) and a stenosis AV (dash-dot black) in the coupled model compared with the standard case (solid blue) on the pressure in the LV proximal to the AV (a), the LV pressure (b) and the flow rate in the LV proximal to the AV (c).

earlier arrival of the peak value. Figure 6.9 shows the comparisons of the peak ejection velocity in the LV with normal and stenosed AVs. With mild stenosis of the AV, the peak velocity increases by 15.1%, compared with the normal AV.

The effects of the different AV conditions on the pressure and flow rate in three typical arteries, i.e. the ascending aorta, renal and femoral arteries, are compared in Fig. 6.10. The peak pressures in the three arteries are almost the same in the LV-SA model with and without the AV in the normal condition, but for the mild stenosis of the AV, it shows a lower peak value with a short delay in the arrival of the peak (Fig. 6.10 (a), (c) and (e)).

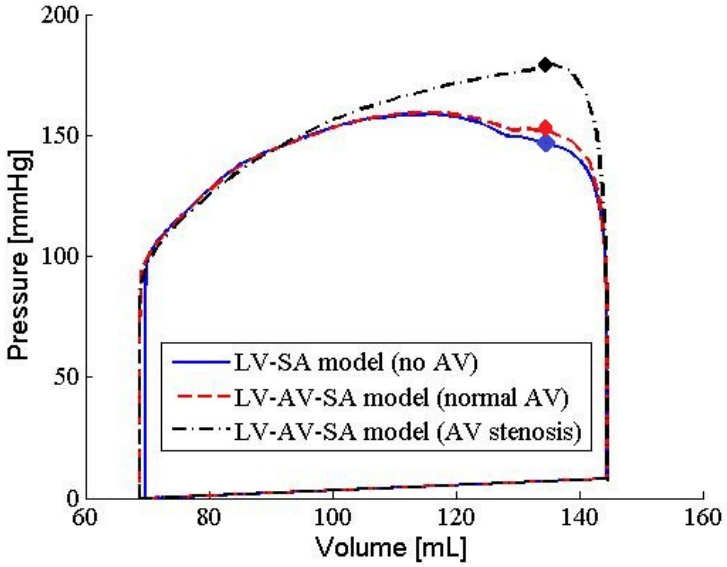

Figure 6.7: Comparisons of the pressure-volume loops of the LV-SA model (solid) and LV-AV-SA model with normal (dashed) and stenosis (dash-dot) valve conditions.

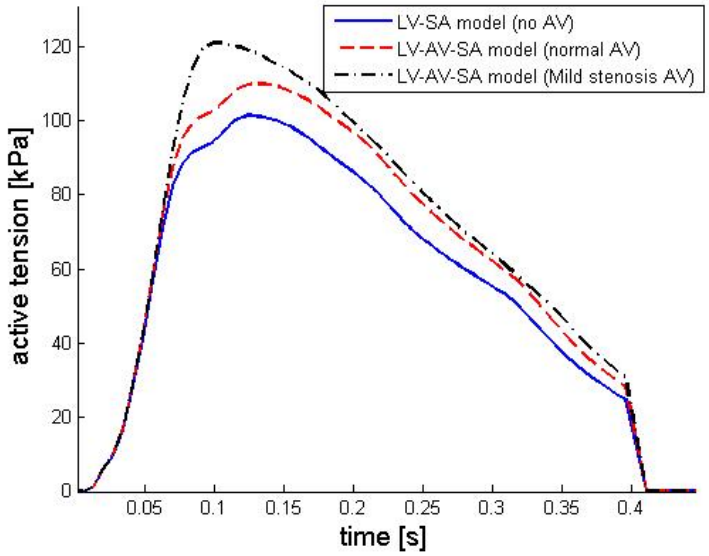

Figure 6.8: Comparisons of the active tension during systole between the LV-SA model (solid) and the LV-AV-SA model with normal (dashed) and stenosis (dash-dot) valve conditions.

Similarly, the peak flow rate are almost the same in the LV-SA model with/without AV in normal condition, but for the mild stenosis AV condition, the peak flow rate decreases with a short delay of the arrival of the peak values (Fig. 6.10 (b), (d) and (f)).

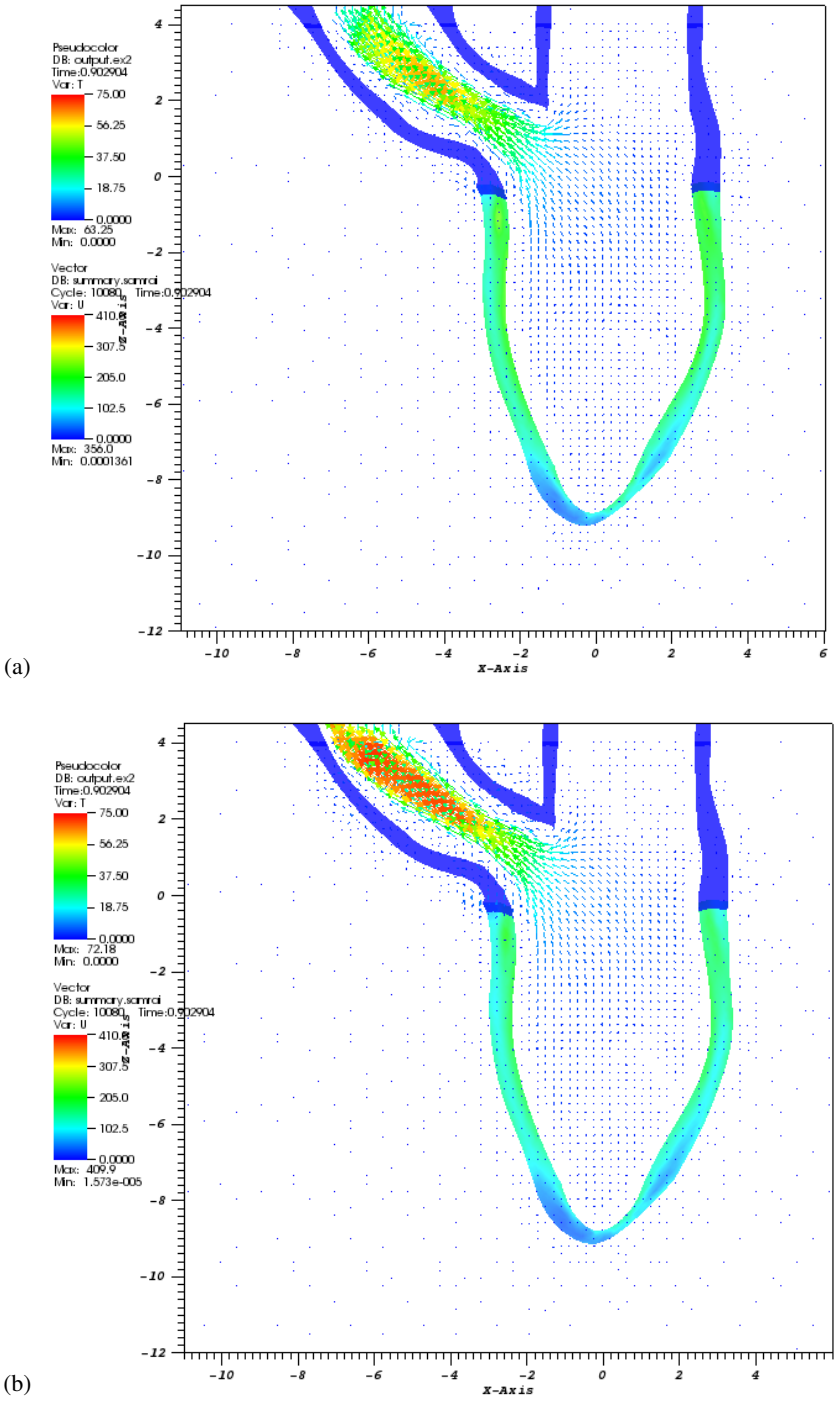

Figure 6.9: Comparisons of the ejection velocity at mid-systole for the LV-AV-SA model with normal (a) and stenosis (b) valve conditions. The maximum velocity in the coupled model with stenosis AV is 15% higher than that with the normal valve condition.

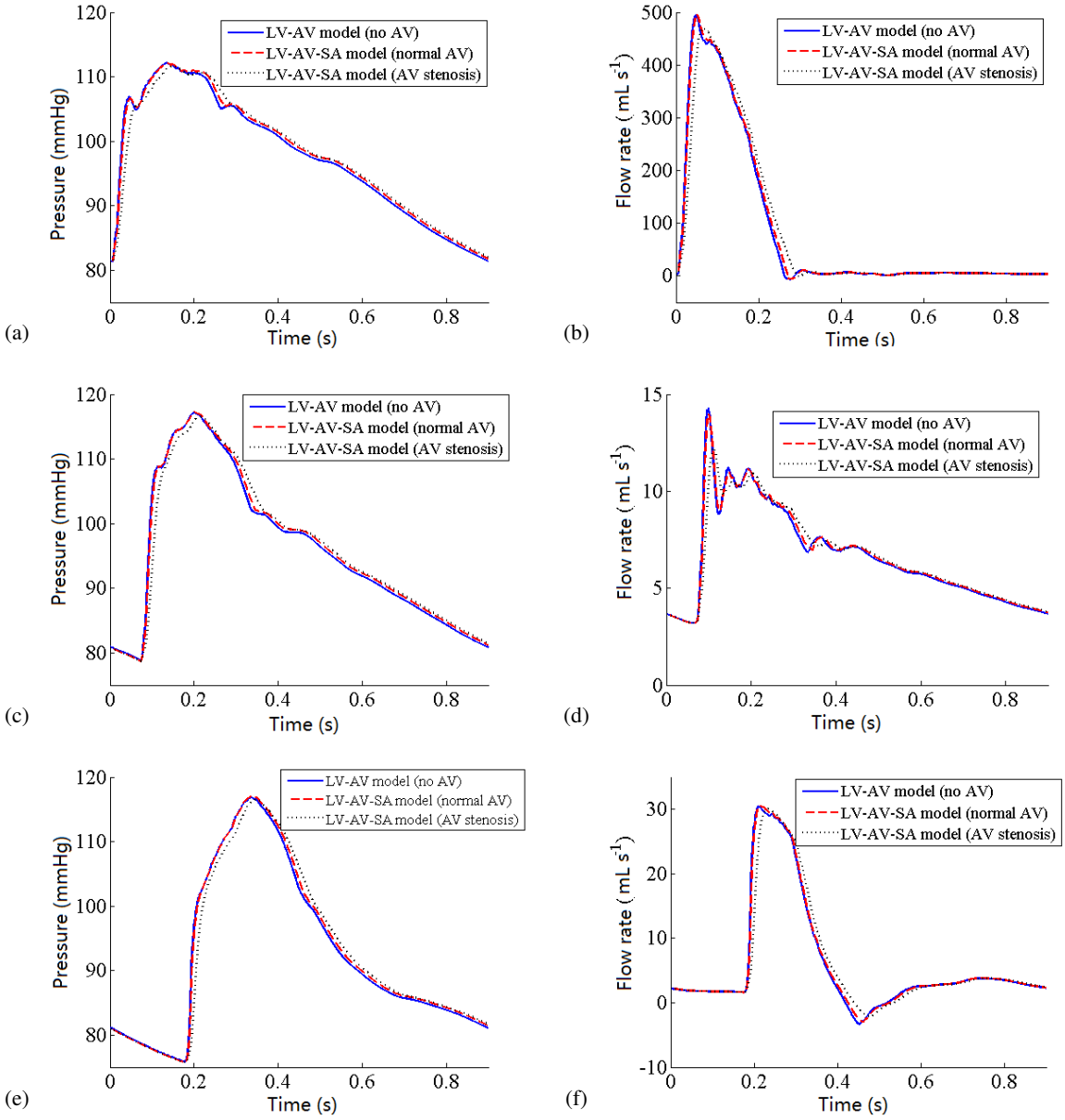

Figure 6.10: Comparisons of the pressure (left) and flow rate (right) in the ascending aorta ((a), (b)), the renal artery ((c), (d)) and the femoral artery ((e), (f)) between the LV-SA model (solid) and the LA-AV-SA model with normal AV (dashed) and stenosis AV (dot) conditions.

6.4 Discussion

In this chapter, a lumped-parameter AV model has been included to further develop the LV-SA model into the LV-AV-SA model to study the effects of stenosis of the AV. With a normal AV condition representing a healthy AV, the predicted peak cross-valve pressure difference is 7.62 mmHg, which is close to the measured peak pressure difference of 9.4 mmHg in dogs [24]. For mild AV stenosis, the predicted peak cross-valve pressure difference is 50.62 mmHg, which is within the range of the measured peak pressure gradient (10–100 mmHg) for mild stenosis [133].

Compared to the LV-SA model (no AV), when a normal AV is used in the coupled LV-AV-SA model, the active tension in the LV and the peak LV pressure at early systole increase, but the peak flow rate and the cardiac output barely change, with only a short delay in the arrival time of the peak values. This corresponds to the pressure difference and the control of the opening and closing valve motion provided by the AV model, which increases the LV pressure as well as slowing down the flow rate to make the peak arrive slightly late. When a mild stenosed AV is used in the coupled LV-AV-SA model, the LV function changes significantly, especially the peak LV pressure and the peak ejection velocity. This indicates that the valve condition is also important in studying cardiac-arterial interactions, especially for diseased valve conditions that the effects are huge and cannot be ignored. The effects of changing the aortic valve condition are more relates to changing the LV function, and these changes for homeostasis may promote heart remodelling over long time.

Chapter 7

Discussion of the cross-valve pressure drop in the LV

As discussed in Chapter 4 and Chapter 6, we have developed a LV-SA model and a LV-AV-SA model, which provide detailed pressure and flow wave propagations from the LV to the systemic arteries to study the interactions between the LV and systemic arteries. From the results, we can see a large pressure drop from the centre LV to the outlet plane in the LV proximal to the AV with or without the AV model. Considering the diameter of the valvular region is measured as 1.8 cm at early systole, and it expands to 2.5 cm in mid-systole, corresponding to a 93% increase in the cross-sectional area of the valvular region, but this expanding procedure has not been fully modelled in the LV model, we reconstruct the outlet tract with the diameter in mid-systole to analysis how the geometry of the valvular region affect the cross-valve pressure in the coupled model.

7.1 Reconstruction of the outlet tract in the LV model

The valvular region is reconstructed from the cardiac magnetic resonance (CMR) images at mid-systole as shown in Fig. 7.1. At that time, the diameter of the valvular region is 2.5 cm. We use the same geometry of the inlet tract and the LV region to combine into a new LV model. Since the valvular region is expanded, and the LV is operating under a lower peak pressure, the required active tension is less than previous LV-SA model. Cur-

rently, we let $T_{\text{scale}} = 3$ and use the same values for all the other parameters as described in Table 4.1 when couple it with the SA model.

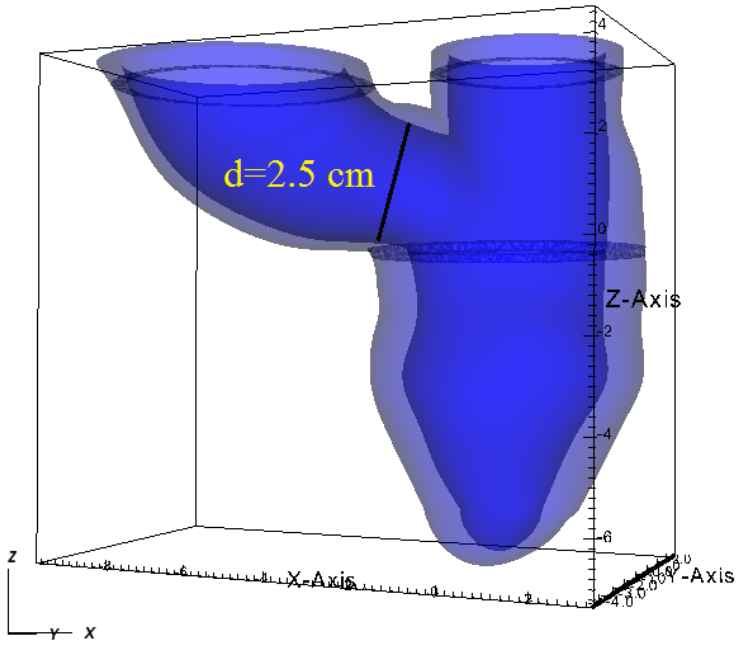

Figure 7.1: Reconstructed LV model from the cardiac magnetic resonance (CMR) images at mid-systole. The diameter of the valvular region is 2.5 cm.

7.2 Results

First, we compare the pressure between the center LV and the pressure in the LV proximal to the AV as shown in Fig. 7.4 (a). The peak LV pressure during systole is 110.2 mmHg, and the peak pressure in the LV proximal to the AV is 111.7 mmHg, which is close to each other. The corresponding pressure difference is shown in Fig. 7.4 (b), in which the pressure difference increases in early systole with peak value of 7.24 mmHg, and then decreases until the end of systole, reaching the minimum value of -9.02 mmHg.

The main characteristics of the LV functions during systole are shown in Fig. 7.3 and in Table 7.1. Compared with previous LV-SA model with narrower valvular region, the results show that the peak LV pressure decreased dramatically, and the pressure drop through the outlet tract reduced significantly, and the peak flow rate increases about 11% with a 33.2 ms shortening in the ejection duration. The stroke volumes are similar when

using early systole and mid-systole valvular diameter to construct the valvular region in this model. The peak velocity decreases from 409.4 cm s^{-1} to 135.7 cm s^{-1} with a wider valvular region in the LV (Fig. 7.2).

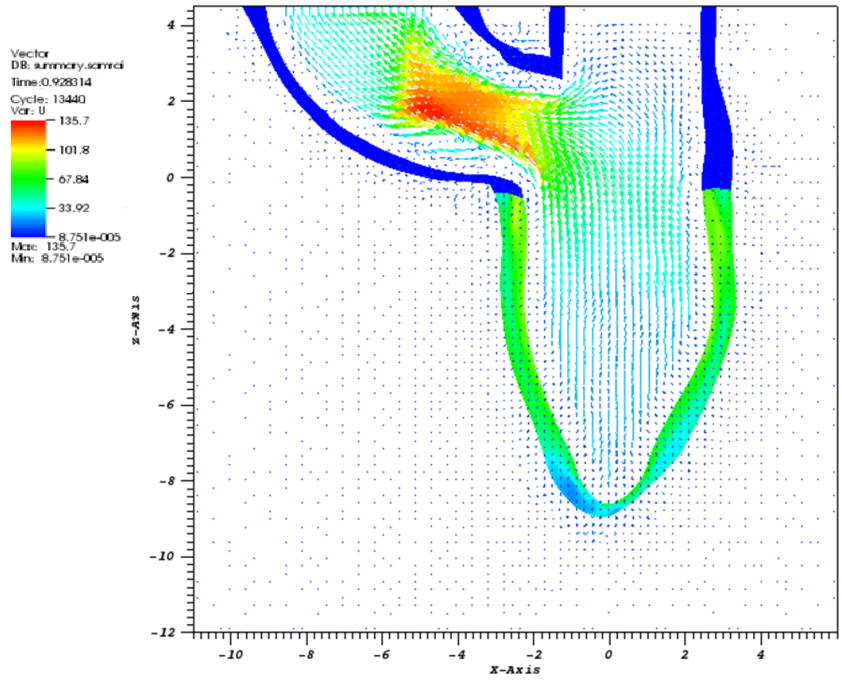

Figure 7.2: The velocity field in the LV with the reconstructed valvular region based on mid-systolic CMR image in middle systole at $t = 0.92$ s.

The pressure and flow rate along the aorta are shown in Fig. 7.5. Detailed peak values of the pressure and flow rate in each arteries are listed in Table 7.2. Compared with the previous standard case in the LV-SA model (Fig. 4.6 and Table 4.2), the pressure profiles in the reconstructed model with wider valvular region shows more pronounced peaks in mid-systole instead of early systole, and showing a time delay in the arriving time of peak values along the aorta.

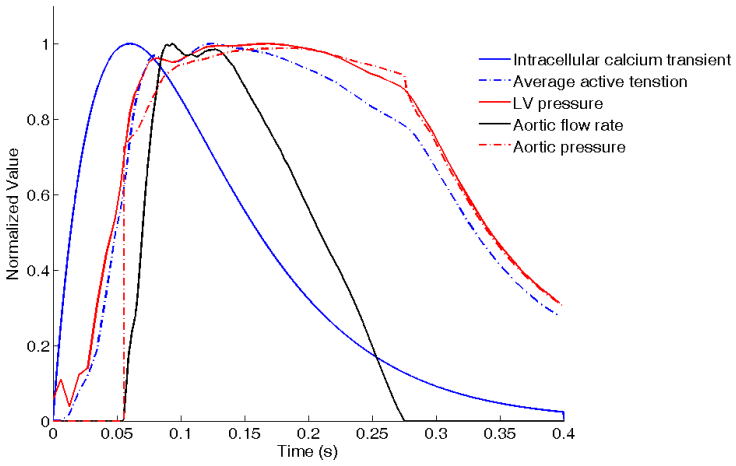

Figure 7.3: Normalized calcium transient (peak: $10^{-7}\,\mu$ mol), average active tension (peak: 68.99 kPa), LV pressure (peak: 113.1 mmHg), aortic flow rate (peak: 549.4 mL s^{-1}) and the aortic pressure (peak: 111.7 mL), 0 s is the beginning of isovolumetric contraction (end of diastole). Data are only from the systolic phase and normalized with peak values.

Diameter of the valvular region	P_{EDA} (mmHg)	P_{a}^{*} (mmHg)	P_{LV}^{*} (mmHg)	Q_{a}^{*} (mL s^{-1})	V_{s} (mL)	T_{ej} (ms)
d=1.8 cm (standard)	81.31	110.3	159.23	494.53	74.68	259.3
d=2.5 cm	81.32	111.7	110.2	549.4	73.3	226.1
(change)	(+0.02)	(+1.7)	(-49.03)	(+54.87)	(-1.38)	(-33.2)

Table 7.1: Summary of systolic LV function with different valvular diameters

	P^{*} (mmHg)	Q^{*} (mL s^{-1})	T_{P}^{*} (ms)	T_{Q}^{*} (ms)
Ascending aorta	113.5	548.3	135.5	55.0
Aortic arc	114.7	421.2	126.9	61.3
Thoracic aorta	117.2	322.4	181.8	82.1
Abdonimal aorta	119.6	227.8	198.5	116.0

Table 7.2: Summary of the pressure, flow rate and arriving time of peak values in the ascending aorta, aortic arc, thoracic aorta and abdonimal aorta during one cardiac cycle

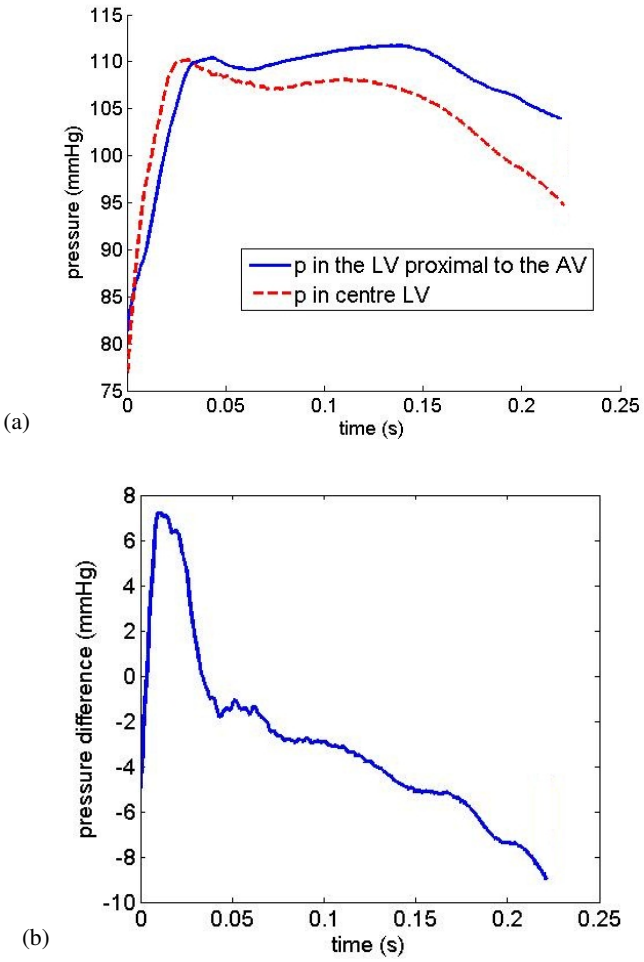

Figure 7.4: Comparisons of LV pressure and pressure in the LV proximal to the AV (a) and the corresponding cross-valve pressure difference (b) during systole.

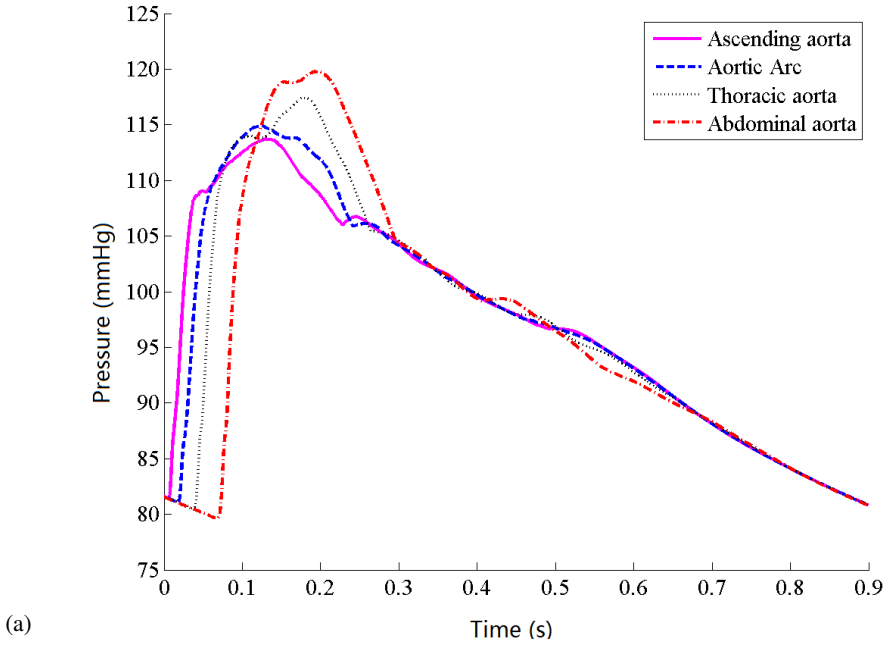

(a)

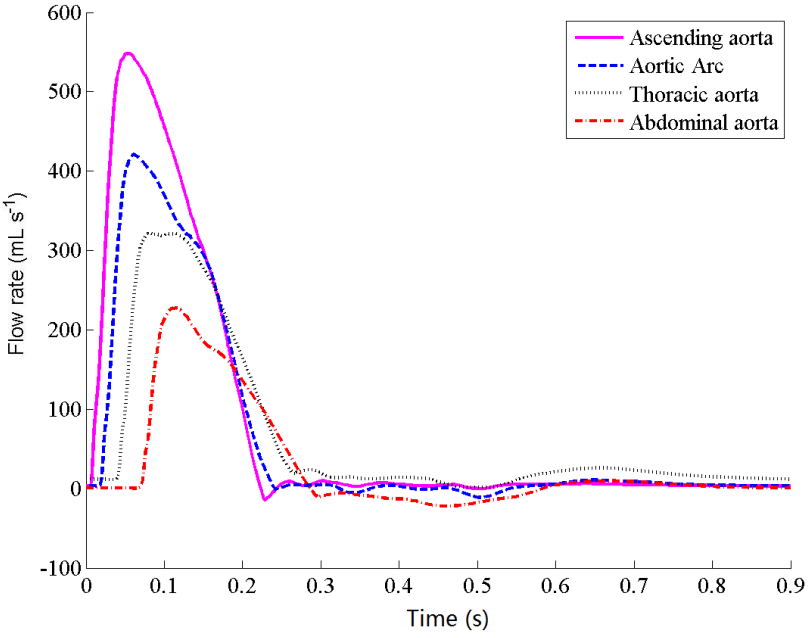

(b)

Figure 7.5: The pressure (a) and the flow rate (b) in the ascending aorta, aortic arc, thoracic aorta and abdonimal aorta in one period for the reconstructed LV.

7.3 Discussion

By expanding the valvular diameter based on the CMR images in mid-systole, the pressure difference between the centre LV and the pressure in the LV proximal to the AV becomes much smaller than that in the previous LV-SA model. The trend of the cross-valve pressure difference is closed to physiological measurement even with a simple boundary condition to mimic the fully open and closed actions of the AV [80], in which the LV pressure first exceeds the aortic pressure in early systole when the AV opens, and then it becomes lower than the aortic pressure when the AV starts to close. The pressure and flow profiles in the SA have the same trend as shown in previous simulations in Chapter 4, which indicates that the main effects of changing diameter of the valvular region is on the LV function. This also suggests that a local stenosis in this region may have significant effect on the heart function. This reconstructed LV-SA model based on CMR images in mid-systole shows different prediction than the previous model based on CMR images in early systole, and it suggests that the valvular extension needs to take into account in future work. A further step is to establish a subject-specific or patient-specific model when enough information is obtained from clinical measurements, so that we can simulate cardio-vascular interactions as well as comparing results with clinical measurements.

Currently, a paper including study of the coupled LV-SA model, in which the diameter of the valvular region is 2.5 cm, has been submitted to *Journal of Biomechanics* [18]. In this paper, the cardio-arterial interactions are studied under normal physiological and several pathological conditions of the LV and the arteries. The quantitative changes provided from the coupled model are useful for analyzing cardio-arterial interactions and future clinical applications.

Chapter 8

Conclusions

The purpose of this study is to develop a dynamic cardio-vascular (or LV-SA) model, which includes a detailed left ventricle and systemic arteries in order to predict pressure and flow interactions in the systemic circulation. This has been successfully achieved by employing a three-dimensional finite-strain structure-based LV, and a one-dimensional dynamic physiologically-based model for the systemic arteries, to complete a coupled LV-SA model.

The LV model is based on Gao et al. [35]s work, in which the fluid-structure interaction (FSI) is described by an Immersed Boundary (IB) approach, and solved by a Lagrangian Finite Element (FE) method. The systemic circulation model is employed from Olufsen et al. [90]'s work, which consists of two groups of arteries, the large arteries and the small arteries or vascular beds. The large-arteries model uses a Lax–Wendroff scheme to compute the cross-sectional area-averaged flow and pressure based on physiological parameters of the arterial tree, and the small arteries are modelled as asymmetric structured trees, to provide outflow boundary conditions at the end of each terminal vessel in the network of the large arteries. The coupling is achieved by matching the pressure and flow rate at the aortic root, i.e. the circulation model feeds back the pressure as a boundary condition to the LV model, and the flow rate from the LV is used as the inflow for the circulation model. There is no aortic valve in the LV, so we model the function of the AV as follows: the AV opens when the pressure in the LV just exceeds the pressure in the proximal aorta adjacent to the valve; the AV closes when the flow rate is negative at the boundary plane in the LV proximal to the AV. The governing equations of the system

are solved by a combined immersed boundary finite element (IB/FE) method, and the Lax–Wendroff scheme of Olufsen et al. [90]. This is an explicit method and sufficiently small time step Δt is used to ensure numerical stability. Below we give a summary of the achievements and observations generated in this thesis and state the limitations of this work and present the course of future works.

8.1 Summary of achievements

In this study, the pressure and flow waveforms in the LV and SA are studied in the LV-SA model. First, this model is tested by a standard case in Chapter 4, based on measurements of healthy LV and healthy systemic arteries from two healthy subjects. The results are compared with those calculated using Olufsen et al. [90]'s model with a periodic cardiac output from the coupled LV-SA model as inlet flow rate boundary condition instead of using a dynamic LV, and the other parameters are kept the same as those in the coupled model. Results in the standard case show that the flow rate in the LV proximal to the AV agrees well with the experiment data ($< 2\%$ difference in peak value). The peak LV pressure (159.1 mmHg) is also close to the experiment data (150 mmHg) ($< 3\%$ in difference).

Secondly, in Chapter 5, we consider four different pathological conditions, i.e. the arterial stiffening with aging, the functional rarefaction in the vascular beds, the fastened heart beat rate and varied end-of-diastolic pressure (EDP) in the LV, to study the effects of disease on the cardio-vascular system. The results show that different disease-related cases have different effects on the cardio-vascular system, but a common effects on the LV function is an increase of the active tension and LV pressure, except for decreasing the EDP in the LV, which has the opposite effects. The effects on the pressure and flow rate in the SA are different:

- Increasing the stiffness of the large arteries results in increased pulse pressure and decreased trough pressure in the SA, and shows an early arrival of the peak flow rate, while increasing the stiffness of small arteries has less effect on the pressure or the flow rate during systole.
- Increasing the degree of vascular rarefaction increases both the peak and the trough

pressures in the SA, and more pronounced back flow in the distal arteries, but the peak flow rate barely changes in the SA.

- Shortening the diastolic phase results in increased mean pressure in the SA, and increased cardiac output per minute.
- Increasing the EDP increases the end-of-diastolic volume, the stoke volume and the peak LV and SA pressures, while decreasing the EDP has the opposite effects on these characteristics.

Compared with the recalculated results from Olufsen et al. [90], the waveform of the pressure and the flow rate in our model have the same trend as those in the circulation model, but both the peak and the trough pressures in the coupled model are lower than those in the circulation model. Moreover, the increasing of the peak pressure caused by disease is less in the coupled model than in the circulation model. This means that the dynamic LV tends to decrease the pressure, reducing the effects of diseases on the systemic arterial system.

Then, in Chapter 6, a lumped-parameter AV model has been included to further develop the LV-SA model into the LV-AV-SA model to study the effects of stenosis of the AV. With a normal AV condition representing a healthy AV, the predicted peak cross-valve pressure difference is 7.62 mmHg, which is close to the measured peak pressure difference of 9.4 mmHg in dogs [24]. For mild AV stenosis, the predicted peak cross-valve pressure difference is 50.62 mmHg, which is within the range of the measured peak pressure gradient (10–100 mmHg) for mild stenosis [133]. Compared to the LV-SA model (no AV), when a normal AV is used in the coupled LV-AV-SA model, the LV function does not change much, but when a stenosed AV is applied in this model, the LV function changes significantly, especially a significant increase of the peak LV pressure and the peak ejection velocity. This indicates that the valve condition is also important in studying cardiac-arterial interactions, especially for diseased valve conditions that the effects are huge and cannot be ignored. The effects of changing the aortic valve condition are more related to changing the LV function, and these changes for homeostasis may promote heart remodelling over long time. Compared to the LV-SA model (no AV), when a normal AV is used in the coupled LV-AV-SA model, the active tension in the LV and the peak LV pressure at early systole increase, but the peak flow rate and the cardiac output

barely change, with only a short delay in the arrival time of the peak values. This corresponds to the pressure difference and the control of the opening and closing valve motion provided by the AV model, which increases the LV pressure as well as slowing down the flow rate to make the peak arrive slightly late. When a mild stenosed AV is used in the coupled LV-AV-SA model, the LV function changes significantly, especially the peak LV pressure and the peak ejection velocity. This indicates that the valve condition is also important in studying cardiac-arterial interactions, especially for diseased valve conditions that the effects are huge and cannot be ignored. The effects of changing the aortic valve condition are more relates to changing the LV function, and these changes for homeostasis may promote heart remodelling over long time.

Finally, in order to study how the diameter of the valvular region affects the cross-valve pressure difference, in Chapter 7, we reconstruct the valvular region based on the mid-systolic CMR images instead of using the early systolic CMR images as shown in the LV model in previous chapters. Since the cross-sectional area of the valvular region at mid-systole is about 93% wider than that in early systole, the cross-valve pressure drop decreases dramatically compared with the narrower valvular region in previous LV-SA model. This indicates that the a local stenosis in the valvular region may have significant effects on the heart function, and a better description of modelling the expanding procedure of the valvular region is needed to predict more physiological results.

With the systemic arterial model providing realistic downstream conditions for the LV, this is the first study to predict the pressure and flow rate profiles simultaneously in the LV and systemic arteries during systole, which is important progress in simulating the cardiovascular system. This coupled model makes it possible to study more detailed interactions between the LV and the systemic arteries under various physiological and pathological conditions during systole. It also provides quantitative changes that are useful for prospective clinical applications. With a simpled aortic valve model, the more complete coupled LV-AV-SA model can also be used to explore the effects of aortic valve stenosis on the circulatory system.

8.2 Future work

Although the current LV-SA and LV-AV-SA models are developed to simulate the pressure and flow dynamics under physiological and pathological conditions, and predict good agreement with physiological features, there are still plenty of room to make further improvements of this work.

First, a wave propagation analysis along the arteries will be useful to study the reflected wave at bifurcations, and it is undergoing at the moment. This study will give more insights of wave propagations and the pressure wave velocity (PWV) will be useful results that is comparable with clinical measurement.

In the current models, the geometry of the LV and SA are not from the same subject, which can be used to study healthy or pathological phenomenons, but can only provide limited results that are comparable with clinical measurements, thus one future work is to establish a subject-specific or patient-specific model, so that we can simulate the cardio-vascular interactions as well comparing the results with clinical measurements. However, it is still difficult to obtain the detailed geometry data for the same subject, thus the patient-specific material parameter estimation remains a challenge.

Since the mitral valve is not included in this model, the diastolic filling state is modeled by applying a pressure boundary condition on the endocardial surface in the LV, which can be further improved by adding a MV model to predict more physiological diastolic filling procedure.

As we have discussed in Chapter 7, the size of the valvular region has big effects on the cross-valve pressure drop in the cardio-vascular system, and a local stenosis in this region have a significant effect on the heart function. Although we have used a lumped-parameter model to predict a physiological opening and closing procedure of the AV between the LV and the SA, the valvular extension is still not considered, which needs further development when we have a better understanding of modelling this region.

In conclusion, this thesis is a step forward in understanding the cardio-vascular interactions in the systemic circulation. By using the LV-SA and the LV-AV-SA model presented in this thesis, we can study the pressure and flow propagation in the LV-SA system. Moreover, this model can also be used to study a wide range of pathological effects on both

the pressure and the flow rate in the LV and the SA. Despite for having room for further developments, the LV-SA and the LV-AV-SA models have a good prospect for clinical applications.

References

[1] J Alastruey Arimon. *Numerical modelling of pulse wave propagation in the cardiovascular system: development, validation and clinical applications*. PhD thesis, Imperial College London (University of London), 2006.

[2] TF Antonios. Microvascular rarefaction in hypertension-reversal or over-correction by treatment? *American Journal of Hypertension*, 19(5):484–485, 2006.

[3] DK Arnett, GW Evans, and WA Riley. Arterial stiffness: a new cardiovascular risk factor? *American Journal of Epidemiology*, 140(8):669–682, 1994.

[4] T Arts, T Delhaas, P Bovendeerd, X Verbeek, and FW Prinzen. Adaptation to mechanical load determines shape and properties of heart and circulation: the circadapt model. *American Journal of Physiology-Heart and Circulatory Physiology*, 288(4):H1943–H1954, 2005.

[5] HB Atabek and HS Lew. Wave propagation through a viscous incompressible fluid contained in an initially stressed elastic tube. *Biophysical Journal*, 6(4):481, 1966.

[6] AP Avolio, SG Chen, RP Wang, CL Zhang, MF Li, and MF O'Rourke. Effects of aging on changing arterial compliance and left ventricular load in a northern chinese urban community. *Circulation*, 68(1):50–58, 1983.

[7] AJ Bank and DR Kaiser. Arterial wall mechanics. In *Pan Vascular Medicine*, pages 151–161. Springer, 2002.

[8] BJ Bellhouse and TL. The fluid mechanics of the aortic valve. *Journal of Fluid Mechanics*, 35(04):721–735, 1969.

[9] D Bessems, M Rutten, and F Van De Vosse. A wave propagation model of blood

flow in large vessels using an approximate velocity profile function. *Journal of Fluid Mechanics*, 580:145–168, 2007.

[10] JG Betts. Anatomy & physiology. pages 787–846, 2013. ISSN 1938168135.

[11] J Beutel, HL Kundel, and RL Van Metter. Handbook of medical imaging, volume 1: Physics and psychophysics. 2000.

[12] R Beyar, MJ Hausknecht, HR Halperin, FC Yin, and ML Weisfeldt. Interaction between cardiac chambers and thoracic pressure in intact circulation. *American Journal of Physiology-Heart and Circulatory Physiology*, 253(5):H1240–H1252, 1987.

[13] PHM Bovendeerd, T Arts, JM Huyghe, DH Van Campen, and RS Reneman. Dependence of local left ventricular wall mechanics on myocardial fiber orientation: a model study. *Journal of Biomechanics*, 25(10):1129–1140, 1992.

[14] R Burattini, S Natalucci, and KB Campbell. Viscoelasticity modulates resonance in the terminal aortic circulation. *Medical Engineering & Physics*, 21(3):175–185, 1999.

[15] N Burns. *Cardiovascular physiology*. Retrieved from School of Medicine, Trinity College, Dublin., 2013.

[16] CJ Carmody, G Burriesci, IC Howard, and EA Patterson. An approach to the simulation of fluid–structure interaction in the aortic valve. *Journal of Biomechanics*, 39(1):158–169, 2006.

[17] JR Cebral, MA Castro, JE Burgess, RS Pergolizzi, MJ Sheridan, and CM Putman. Characterization of cerebral aneurysms for assessing risk of rupture by using patient-specific computational hemodynamics models. *American Journal of Neuroradiology*, 26(10):2550–2559, 2005.

[18] WW Chen, H Gao, XY Luo, and NA Hill. Study of cardiovascular functions using a coupled left ventricle and systemic circulation model. *Journal of Biomechanics (Submitted)*, 2015.

[19] KD Costa, PJ Hunter, JM Rogers, JM Guccione, LK Waldman, and AD McCulloch. A three-dimensional finite element method for large elastic deformations of

ventricular myocardium: Icylindrical and spherical polar coordinates. *Journal of Biomechanical Engineering*, 118(4):452–463, 1996.

[20] KD Costa, JW Holmes, and AD McCulloch. Modelling cardiac mechanical properties in three dimensions. *Philosophical Transactions of the Royal Society of London A: Mathematical, Physical and Engineering Sciences*, 359(1783):1233–1250, 2001.

[21] J De Hart, G Cacciola, PJG Schreurs, and GWM Peters. A three-dimensional analysis of a fibre-reinforced aortic valve prosthesis. *Journal of Biomechanics*, 31 (7):629–638, 1998.

[22] J De Hart, GWM Peters, PJG Schreurs, and FPT Baaijens. A three-dimensional computational analysis of fluid–structure interaction in the aortic valve. *Journal of Biomechanics*, 36(1):103–112, 2003.

[23] H Demiray. Stresses in ventricular wall. *Journal of Applied Mechanics*, 43(2): 194–197, 1976.

[24] TE Driscol and RW Eckstein. Systolic pressure gradients across the aortic valve and in the ascending aorta. *American Journal of Physiology*, 209(3):557–563, 1965.

[25] G Drzewiecki, JJ Wang, JKJ Li, J Kedem, and H Weiss. Modeling of mechanical dysfunction in regional stunned myocardium of the left ventricle. *Biomedical Engineering, IEEE Transactions on*, 43(12):1151–1163, 1996.

[26] CA Figueroa, IE Vignon-Clementel, KE Jansen, TJR Hughes, and CA Taylor. A coupled momentum method for modeling blood flow in three-dimensional deformable arteries. *Computer Methods in Applied Mechanics and Engineering*, 195 (41):5685–5706, 2006.

[27] SM Finkelstein and JN Cohn. First-and third-order models for determining arterial compliance. *Journal of Hypertension*, 10:S11–S14, 1992.

[28] L Formaggia, JF Gerbeau, F Nobile, and A Quarteroni. On the coupling of 3d and 1d navier–stokes equations for flow problems in compliant vessels. *Computer Methods in Applied Mechanics and Engineering*, 191(6):561–582, 2001.

[29] L Formaggia, D Lamponi, and A Quarteroni. One-dimensional models for blood flow in arteries. *Journal of Engineering Mathematics*, 47(3-4):251–276, 2003.

[30] YC Fung. Biodynamics: Circulation springer. *New York*, 1984.

[31] K Furutani, M Kato, and T Tsuru. Low-pass filter, September 16 1997. US Patent 5,668,511.

[32] H Gao, BE Griffith, D Carrick, C McComb, C Berry, and XY Luo. Initial experience with a dynamic imaging-derived immersed boundary model of human left ventricle. In *Functional Imaging and Modeling of the Heart*, pages 11–18. Springer, 2013.

[33] H Gao, X Ma, N Qi, C Berry, BE Griffith, and XY Luo. A finite strain nonlinear human mitral valve model with fluid-structure interaction. *International Journal for Numerical Methods in Biomedical Engineering*, 30(12):1597–1613, 2014.

[34] H Gao, H Wang, C Berry, XY Luo, and BE Griffith. Quasi-static image-based immersed boundary-finite element model of left ventricle under diastolic loading. *International Journal for Numerical Methods in Biomedical Engineering*, 30(11): 1199–1222, 2014.

[35] H Gao, C Berry, and XY Luo. Image-derived human left ventricular modelling with fluid-structure interaction. In H Van Assen, P Bovendeerd, and T Delhaas, editors, *Functional Imaging and Modeling of the Heart*, volume 9126 of *Lecture Notes in Computer Science*, pages 321–329. Springer International Publishing, 2015. ISBN 978-3-319-20308-9.

[36] H Gao, N Qi, X Ma, BE Griffith, C Berry, and XY Luo. Fluid-structure interaction model of human mitral valve within left ventricle. In *Functional Imaging and Modeling of the Heart*, pages 330–337. Springer, 2015.

[37] JF Gerbeau, M Vidrascu, and P Frey. Fluid–structure interaction in blood flows on geometries based on medical imaging. *Computers & Structures*, 83(2):155–165, 2005.

[38] MS Goligorsky. Microvascular rarefaction: the decline and fall of blood vessels. *Organogenesis*, 6(1):1–10, 2010.

[39] BE Griffith. Immersed boundary model of aortic heart valve dynamics with physiological driving and loading conditions. *International Journal for Numerical Methods in Biomedical Engineering*, 28(3):317–345, 2012.

[40] BE Griffith and XY Luo. Hybrid finite difference/finite element version of the immersed boundary method. *Submitted in revised form*, 2012.

[41] BE Griffith, RD Hornung, DM McQueen, and CS Peskin. An adaptive, formally second order accurate version of the immersed boundary method. *Journal of Computational Physics*, 223(1):10–49, 2007.

[42] BE Griffith, XY Luo, DM McQueen, and CS Peskin. Simulating the fluid dynamics of natural and prosthetic heart valves using the immersed boundary method. *International Journal of Applied Mechanics*, 1(01):137–177, 2009.

[43] JM Guccione, AD McCulloch, and LK Waldman. Passive material properties of intact ventricular myocardium determined from a cylindrical model. *Journal of Biomechanical Engineering*, 113(1):42–55, 1991.

[44] JM Guccione, LK Waldman, and AD McCulloch. Mechanics of active contraction in cardiac muscle: Part iicylindrical models of the systolic left ventricle. *Journal of Biomechanical Engineering*, 115(1):82–90, 1993.

[45] JE Hall. *Guyton and Hall textbook of medical physiology*. Elsevier Health Sciences, 2010.

[46] T Heldt, EB Shim, RD Kamm, and RG Mark. Computational modeling of cardiovascular response to orthostatic stress. *Journal of Applied Physiology*, 92(3): 1239–1254, 2002.

[47] GA Holzapfel and RW Ogden. Constitutive modelling of passive myocardium: a structurally based framework for material characterization. *Philosophical Transactions of the Royal Society of London A: Mathematical, Physical and Engineering Sciences*, 367(1902):3445–3475, 2009.

[48] GA Holzapfel, TC Gasser, and RW Ogden. A new constitutive framework for arterial wall mechanics and a comparative study of material models. *Journal of Elasticity and the Physical Science of Solids*, 61(1-3):1–48, 2000.

[49] N Hopkins and P McLoughlin. The structural basis of pulmonary hypertension in chronic lung disease: remodelling, rarefaction or angiogenesis? *Journal of Anatomy*, 201(4):335–348, 2002.

[50] TJR Hughes and J Lubliner. On the one-dimensional theory of blood flow in the larger vessels. *Mathematical Biosciences*, 18(1):161–170, 1973.

[51] JD Humphrey and FCP Yin. On constitutive relations and finite deformations of passive cardiac tissue: I. a pseudostrain-energy function. *Journal of Biomechanical Engineering*, 109(4):298–304, 1987.

[52] JD Humphrey, RK Strumpf, and FCP Yin. Determination of a constitutive relation for passive myocardium: I. a new functional form. *Journal of Biomechanical Engineering*, 112(3):333–339, 1990.

[53] PJ Hunter, MP Nash, and GB Sands. Computational electromechanics of the heart. *Computational Biology of the Heart*, 12:347–407, 1997.

[54] M Javorka, I Zila, T Balharek, and K Javorka. Heart rate recovery after exercise: relations to heart rate variability and complexity. *Brazilian Journal of Medical and Biological Research*, 35(8):991–1000, 2002.

[55] GS Kassab, CA Rider, NJ Tang, and YC Fung. Morphometry of pig coronary arterial trees. *American Journal of Physiology-Heart and Circulatory Physiology*, 265(1):H350–H365, 1993.

[56] HJ Kim, IE Vignon-Clementel, CA Figueroa, JF LaDisa, KE Jansen, JA Feinstein, and CA Taylor. On coupling a lumped parameter heart model and a three-dimensional finite element aorta model. *Annals of Biomedical Engineering*, 37(11): 2153–2169, 2009.

[57] R Klabunde. *Cardiovascular physiology concepts*. Lippincott Williams & Wilkins, 2011.

[58] P Kohl, D Noble, RL Winslow, and PJ Hunter. Computational modelling of biological systems: tools and visions. *Philosophical Transactions of the Royal Society of London A: Mathematical, Physical and Engineering Sciences*, 358(1766):579–610, 2000.

[59] T Korakianitis and Y Shi. Numerical simulation of cardiovascular dynamics with healthy and diseased heart valves. *Journal of Biomechanics*, 39(11):1964–1982, 2006.

[60] A Krishnamurthy, CT Villongco, J Chuang, LR Frank, V Nigam, E Belezzuoli, P Stark, DE Krummen, S Narayan, JH Omens, et al. Patient-specific models of cardiac biomechanics. *Journal of Computational Physics*, 244:4–21, 2013.

[61] DN Ku. Blood flow in arteries. *Annual Review of Fluid Mechanics*, 29(1):399–434, 1997.

[62] EM Landis and JR Pappenheimer. Exchange of substances through the capillary walls. *Handbook of Physiology*, 2(2):961–1034, 1963.

[63] LJ Laslett, P Alagona, BA Clark, JP Drozda, F Saldivar, SR Wilson, C Poe, and M Hart. The worldwide environment of cardiovascular disease: prevalence, diagnosis, therapy, and policy issues: a report from the american college of cardiology. *Journal of the American College of Cardiology*, 60(25_S):S1–S49, 2012.

[64] HY Lee and BH Oh. Aging and arterial stiffness. *Circulation Journal*, 74(11): 2257–2262, 2010.

[65] IJ LeGrice, BH Smaill, LZ Chai, SG Edgar, JB Gavin, and PJ Hunter. Laminar structure of the heart: ventricular myocyte arrangement and connective tissue architecture in the dog. *American Journal of Physiology-Heart and Circulatory Physiology*, 269(2):H571–H582, 1995.

[66] IJ LeGrice, PJ Hunter, and BH Smaill. Laminar structure of the heart: a mathematical model. *American Journal of Physiology-Heart and Circulatory Physiology*, 272(5):H2466–H2476, 1997.

[67] RG Leyh, C Schmidtke, HH Sievers, and MH Yacoub. Opening and closing characteristics of the aortic valve after different types of valve-preserving surgery. *Circulation*, 100(21):2153–2160, 1999.

[68] JKJ Li. *Comparative cardiovascular dynamics of mammals*. CRC press, 1995.

[69] H Liu, FY Liang, J Wong, T Fujiwara, W Ye, K Tsubota, and M Sugawara. Multi-

scale modeling of hemodynamics in the cardiovascular system. *Acta Mechanica Sinica*, 31(4):446–464, 2015.

[70] B Lohff. Das jahr 1899: Die erste mathematische beschreibung des druck-volumen-diagramms durch otto frank (1865-1944). *Sudhoffs Archiv*, pages 131–151, 1999.

[71] X Ma, H Gao, BE Griffith, C Berry, and XY Luo. Image-based fluid–structure interaction model of the human mitral valve. *Computers & Fluids*, 71:417–425, 2013.

[72] G Mahadevan, RC Davis, MP Frenneaux, FDR Hobbs, GYH Lip, JE Sanderson, and MK Davies. Left ventricular ejection fraction: are the revised cut-off points for defining systolic dysfunction sufficiently evidence based? *Heart*, 94(4):426–428, 2008.

[73] VB Makhijani, HQ Yang, PJ Dionne, and MJ Thubrikar. Three-dimensional coupled fluid-structure simulation of pericardial bioprosthetic aortic valve function. *ASAIO Journal*, 43(5):M392, 1997.

[74] KS Matthys, J Alastruey, J Peiró, AW Khir, P Segers, PR Verdonck, KH Parker, and SJ Sherwin. Pulse wave propagation in a model human arterial network: assessment of 1-d numerical simulations against in vitro measurements. *Journal of Biomechanics*, 40(15):3476–3486, 2007.

[75] WL Maughan, K Sunagawa, and K Sagawa. Ventricular systolic interdependence: volume elastance model in isolated canine hearts. *American Journal of Physiology-Heart and Circulatory Physiology*, 253(6):H1381–H1390, 1987.

[76] M McCormick, D Nordsletten, D Kay, and N Smith. Modelling left ventricular function under assist device support. *International Journal for Numerical Methods in Biomedical Engineering*, 27(7):1073–1095, 2011.

[77] DM McQueen and CS Peskin. A three-dimensional computer model of the human heart for studying cardiac fluid dynamics. *ACM SIGGRAPH Computer Graphics*, 34(1):56–60, 2000.

[78] LM Mielniczuk, GA Lamas, GC Flaker, G Mitchell, SC Smith, BJ Gersh, SD Solomon, LA Moyé, JL Rouleau, JD Rutherford, et al. Left ventricular end-

diastolic pressure and risk of subsequent heart failure in patients following an acute myocardial infarction. *Congestive Heart Failure*, 13(4):209–214, 2007.

[79] LO Müller and EF Toro. A global multiscale mathematical model for the human circulation with emphasis on the venous system. *International Journal for Numerical Methods in Biomedical Engineering*, 30(7):681–725, 2014.

[80] JP Mynard, MR Davidson, DJ Penny, and JJ Smolich. A simple, versatile valve model for use in lumped parameter and one-dimensional cardiovascular models. *International Journal for Numerical Methods in Biomedical Engineering*, 28(6-7): 626–641, 2012.

[81] MP Nash and PJ Hunter. Computational mechanics of the heart. *Journal of Elasticity and the Physical Science of Solids*, 61(1-3):113–141, 2000.

[82] RM Nerem. Vascular fluid mechanics, the arterial wall, and atherosclerosis. *Journal of Biomechanical Engineering*, 114(3):274–282, 1992.

[83] SA Niederer, PJ Hunter, and NP Smith. A quantitative analysis of cardiac myocyte relaxation: a simulation study. *Biophysical Journal*, 90(5):1697–1722, 2006.

[84] SA Niederer, G Plank, P Chinchapatnam, M Ginks, P Lamata, KS Rhode, CA Rinaldi, R Razavi, and NP Smith. Length-dependent tension in the failing heart and the efficacy of cardiac resynchronization therapy. *Cardiovascular Research*, 89(2): 336–343, 2011.

[85] JP Noon, BR Walker, DJ Webb, AC Shore, DW Holton, HV Edwards, and GC Watt. Impaired microvascular dilatation and capillary rarefaction in young adults with a predisposition to high blood pressure. *Journal of Clinical Investigation*, 99(8): 1873, 1997.

[86] D Nordsletten, M McCormick, PJ Kilner, P Hunter, D Kay, and NP Smith. Fluid–solid coupling for the investigation of diastolic and systolic human left ventricular function. *International Journal for Numerical Methods in Biomedical Engineering*, 27(7):1017–1039, 2011.

[87] JB Olansen, JW Clark, D Khoury, F Ghorbel, and A Bidani. A closed-loop model of

the canine cardiovascular system that includes ventricular interaction. *Computers and Biomedical Research*, 33(4):260–295, 2000.

[88] MS Olufsen. *Modeling the arterial system with reference to an anestesia simulator*. PhD thesis, Roskilde Universitetscenter, Institut for Studiet af Matematik og Fysik samt deres Funktioner i Undervisning, Forskning og Anvendelser, 1998.

[89] MS Olufsen. Structured tree outflow condition for blood flow in larger systemic arteries. *American Journal of Physiology-Heart and Circulatory Physiology*, 276 (1):H257–H268, 1999.

[90] MS Olufsen, CS Peskin, WY Kim, EM Pedersen, A Nadim, and J Larsen. Numerical simulation and experimental validation of blood flow in arteries with structured-tree outflow conditions. *Annals of Biomedical Engineering*, 28(11):1281–1299, 2000.

[91] MS Olufsen, NA Hill, GDA Vaughan, C Sainsbury, and M Johnson. Rarefaction and blood pressure in systemic and pulmonary arteries. *Journal of Fluid Mechanics*, 705:280–305, 2012.

[92] EM Pedersen, HW Sung, AC Burlson, and AP Yoganathan. Two-dimensional velocity measurements in a pulsatile flow model of the normal abdominal aorta simulating different hemodynamic conditions. *Journal of biomechanics*, 26(10): 1237–1247, 1993.

[93] TJ Pedley. The fluid mechanics of large blood vessels, cambridge university press, cambridge, 1980.

[94] TJ Pedley and XY Luo. Fluid mechanics of large blood vessels. 1995.

[95] G Pennati, M Bellotti, and R Fumero. Mathematical modelling of the human foetal cardiovascular system based on doppler ultrasound data. *Medical Engineering & Physics*, 19(4):327–335, 1997.

[96] K Perktold and G Rappitsch. Computer simulation of local blood flow and vessel mechanics in a compliant carotid artery bifurcation model. *Journal of Biomechanics*, 28(7):845–856, 1995.

[97] CS Peskin. Numerical analysis of blood flow in the heart. *Journal of Computational Physics*, 25(3):220–252, 1977.

[98] CS Peskin. The fluid dynamics of heart valves: experimental, theoretical, and computational methods. *Annual Review of Fluid Mechanics*, 14(1):235–259, 1982.

[99] CS Peskin. The immersed boundary method. *Acta Numerica*, 11:479–517, 2002.

[100] CS Peskin and DM McQueen. A three-dimensional computational method for blood flow in the heart i. immersed elastic fibers in a viscous incompressible fluid. *Journal of Computational Physics*, 81(2):372–405, 1989.

[101] M Potse, B Dubé, J Richer, A Vinet, and RM Gulrajani. A comparison of monodomain and bidomain reaction-diffusion models for action potential propagation in the human heart. *Biomedical Engineering, IEEE Transactions on*, 53(12):2425–2435, 2006.

[102] M Umar Qureshi and NA Hill. A computational study of pressure wave reflections in the pulmonary arteries. *Journal of Mathematical Biology*, pages 1–25, 2015.

[103] MU Qureshi, GDA Vaughan, C Sainsbury, M Johnson, CS Peskin, MS Olufsen, and NA Hill. Numerical simulation of blood flow and pressure drop in the pulmonary arterial and venous circulation. *Biomechanics and Modeling in Mechanobiology*, 13(5):1137–1154, 2014.

[104] WP Santamore and D Burkhoff. Hemodynamic consequences of ventricular interaction as assessed by model analysis. *American Journal of Physiology-Heart and Circulatory Physiology*, 260(1):H146–H157, 1991.

[105] H Schmid, MP Nash, AA Young, and PJ Hunter. Myocardial material parameter estimationa comparative study for simple shear. *Journal of Biomechanical Engineering*, 128(5):742–750, 2006.

[106] JB Schwartz, WJ Gibb, and T Tran. Aging effects on heart rate variation. *Journal of Gerontology*, 46(3):M99–M106, 1991.

[107] HD Sesso, MJ Stampfer, B Rosner, CH Hennekens, JM Gaziano, JE Manson, and RJ Glynn. Systolic and diastolic blood pressure, pulse pressure, and mean arterial

pressure as predictors of cardiovascular disease risk in men. *Hypertension*, 36(5): 801–807, 2000.

[108] JT Shepherd and PM Vanhoutte. The human cardiovascular system. facts and concepts. 1979.

[109] Y Shi, TJH Yeo, and Y Zhao. Numerical simulation of a systemic flow test rig. *ASAIO Journal*, 50(1):54–64, 2004.

[110] American Physiological Society. *The American Physiological Society Methods in Physiology Series*. Oxford University Press, 1994.

[111] BN Steele, MS Olufsen, and CA Taylor. Fractal network model for simulating abdominal and lower extremity blood flow during resting and exercise conditions. *Computer Methods in Biomechanics and Biomedical Engineering*, 10(1):39–51, 2007.

[112] DA Steinman, JS Milner, CJ Norley, SP Lownie, and DW Holdsworth. Image-based computational simulation of flow dynamics in a giant intracranial aneurysm. *American Journal of Neuroradiology*, 24(4):559–566, 2003.

[113] N Stergiopulos, DF Young, and TR Rogge. Computer simulation of arterial flow with applications to arterial and aortic stenoses. *Journal of Biomechanics*, 25(12): 1477–1488, 1992.

[114] N Stergiopulos, BE Westerhof, and N Westerhof. Total arterial inertance as the fourth element of the windkessel model. *American Journal of Physiology-Heart and Circulatory Physiology*, 276(1):H81–H88, 1999.

[115] Y Sun, BJ Sjoberg, P Ask, D Loyd, and B Wranne. Mathematical model that characterizes transmitral and pulmonary venous flow velocity patterns. *American Journal of Physiology-Heart and Circulatory Physiology*, 268(1):H476–H489, 1995.

[116] Y Sun, M Beshara, RJ Lucariello, and SA Chiaramida. A comprehensive model for right-left heart interaction under the influence of pericardium and baroreflex. *American Journal of Physiology-Heart and Circulatory Physiology*, 272(3):H1499–H1515, 1997.

[117] J Svensson, R Gårdhagen, E Heiberg, T Ebbers, D Loyd, T Länne, and M Karlsson.

Feasibility of patient specific aortic blood flow cfd simulation. In *Medical Image Computing and Computer-Assisted Intervention–MICCAI 2006*, pages 257–263. Springer, 2006.

[118] CA Taylor, TJR Hughes, and CK Zarins. Finite element modeling of three-dimensional pulsatile flow in the abdominal aorta: relevance to atherosclerosis. *Annals of Biomedical Engineering*, 26(6):975–987, 1998.

[119] SA Urquiza, PJ Blanco, MJ Vénere, and RA Feijóo. Multidimensional modelling for the carotid artery blood flow. *Computer Methods in Applied Mechanics and Engineering*, 195(33):4002–4017, 2006.

[120] TP Usyk, R Mazhari, and AD McCulloch. Effect of laminar orthotropic myofiber architecture on regional stress and strain in the canine left ventricle. *Journal of Elasticity and the Physical Science of Solids*, 61(1-3):143–164, 2000.

[121] HBM Uylings. Optimization of diameters and bifurcation angles in lung and vascular tree structures. *Bulletin of Mathematical Biology*, 39(5):509–520, 1977.

[122] M Vollkron, H Schima, L Huber, and G Wieselthaler. Interaction of the cardiovascular system with an implanted rotary assist device: Simulation study with a refined computer model¿. *Artificial Organs*, 26(4):349–359, 2002.

[123] HM Wang, H Gao, XY Luo, C Berry, BE Griffith, RW Ogden, and TJ Wang. Structure-based finite strain modelling of the human left ventricle in diastole. *International Journal for Numerical Methods in Biomedical Engineering*, 29(1):83–103, 2013.

[124] H Watanabe, T Hisada, S Sugiura, J Okada, and H Fukunari. Computer simulation of blood flow, left ventricular wall motion and their interrelationship by fluid-structure interaction finite element method. *JSME International Journal Series C*, 45(4):1003–1012, 2002.

[125] H Watanabe, S Sugiura, H Kafuku, and T Hisada. Multiphysics simulation of left ventricular filling dynamics using fluid-structure interaction finite element method. *Biophysical Journal*, 87(3):2074–2085, 2004.

[126] T Weber, J Auer, MF ORourke, E Kvas, E Lassnig, R Berent, and B Eber. Arterial

stiffness, wave reflections, and the risk of coronary artery disease. *Circulation*, 109 (2):184–189, 2004.

[127] JF Wenk, P Eslami, Z Zhang, C Xu, E Kuhl, JH Gorman, JD Robb, MB Ratcliffe, RC Gorman, and JM Guccione. A novel method for quantifying the in-vivo mechanical effect of material injected into a myocardial infarction. *The Annals of Thoracic Surgery*, 92(3):935–941, 2011.

[128] J Werner, D Böhringer, and M Hexamer. Simulation and prediction of cardiotherapeutical phenomena from a pulsatile model coupled to the guyton circulatory model. *Biomedical Engineering, IEEE Transactions on*, 49(5):430–439, 2002.

[129] N Westerhof, JW Lankhaar, and BE Westerhof. The arterial windkessel. *Medical & Biological Engineering & Computing*, 47(2):131–141, 2009.

[130] IB Wilkinson, H MacCallum, L Flint, JR Cockcroft, DE Newby, and DJ Webb. The influence of heart rate on augmentation index and central arterial pressure in humans. *The Journal of Physiology*, 525(1):263–270, 2000.

[131] RL Winslow, DF Scollan, A Holmes, CK Yung, J Zhang, and MS Jafri. Electrophysiological modeling of cardiac ventricular function: from cell to organ. *Annual Review of Biomedical Engineering*, 2:119, 2000.

[132] JR Womersley. Oscillatory flow in arteries: the constrained elastic tube as a model of arterial flow and pulse transmission. *Physics in Medicine and Biology*, 2(2):178, 1957.

[133] P Wood. Aortic stenosis. *The American Journal of Cardiology*, 1(5):553–571, 1958.